Title: Magnetic force imaging and handling of cancer cells on the nanoscale

Name: Jinyun Liu

This is a digitised version of a dissertation submitted to the University of Bedfordshire.

It is available to view only.

This item is subject to copyright.

MAGNETIC FORCE IMAGING AND HANDLING OF CANCER CELLS ON THE NANOSCALE

Jinyun LIU

Ph.D

2017

UNIVERSITY OF BEDFORDSHIRE

MAGNETIC FORCE IMAGING AND HANDLING OF CANCER CELLS ON THE NANOSCALE

by

Jinyun LIU

A thesis submitted to the University of Bedfordshire in partial fulfilment of the requirements for the degree of Doctor of Philosophy

November 2017

Declaration Of Authorship

I, Jinyun Liu declare that this thesis and the work presented in it are my own and has been generated by me as the result of my own original research.

[Magnetic Force Imaging and Handling of Cancer Cells on the Nanoscale]

I confirm that:

1. This work was done wholly or mainly while in candidature for a research degree at this University;
2. Where any part of this thesis has previously been submitted for a degree or any other qualification at this University or any other institution, this has been clearly stated;
3. Where I have cited the published work of others, this is always clearly attributed;
4. Where I have quoted from the work of others, the source is always given. With the exception of such quotations, this thesis is entirely my own work;
5. I have acknowledged all main sources of help;
6. Where the thesis is based on work done by myself jointly with others, I have made clear exactly what was done by others and what I have contributed myself;
7. Either none of this work has been published before submission, or parts of this work have been published as indicated on [PUBLISHED WORK AS PARTS OF THIS THESIS (See pages IV-V)].

Name of Candidate: Jinyun Liu Signature: Jinyun Liu

Date: 29 November 2017

MAGNETIC FORCE IMAGING AND HANDLING OF CANCER CELLS ON THE NANOSCALE

Jinyun Liu

ABSTRACT

Cancer treatment has become one of the top priorities in health. Great efforts have been devoted to the diagnosis and therapy of cancers. Culturing cells with drugs is a common method used to investigate cancer therapy in experiments. However, this method has limitations in cancer treatment because of the lack of capabilities of handling cells, targeting specific cells and measuring the nanoscale changes in cell structures. Magnetic nanoparticles (MNPs) and magnetic force microscopes (MFMs) have been used to study biological samples due to their advantages in tracing, manipulating and measuring, which has motivated to research the method for implanting MNPs into cancer cells, to target the cancer cells and to measure their changes during the treatment. Research reported in this thesis focuses on magnetic force imaging and handling of targeted cancer cells on the nanoscale for possible new cancer therapies.

A new differential MFM imaging method and a new compensation MFM imaging method were developed in this research to improve the MFM imaging quality. The

former reverses the magnetized direction of probe from upward to downward and the latter scans the samples with three scanning directions of 0°, 45° and 90°. With these methods, the obtained MFM images achieve a high resolution, SNR, image contrast and accuracy.

A pair of innovative MNPs picking up method and MNPs releasing method were developed in this research to achieve flexible MNPs picking up and releasing. The picking up method handles the magnetic tip following a helical structure as the capture path when approaching to the target MNPs. The MNPs releasing method uses a biaxiably-oriented polypropylene (BOPP) film together with a magnet allowing MNPs to separate from the MFM tip surface. With these methods, the target MNPs can be picked up by the MFM tip and released from the tip surface successfully.

This research discovered, for the first time in the world to the author knowledge, the differences in morphological features (height, length, width and roughness) and mechanical properties (adhesive force and Young's modulus) between multinuclear and mononuclear colon cancer cells after treating the cells with fullerenol. This discovery provides guidance to the selection of cells for target treatment. The results indicate that the mononuclear SW480 cells are more sensitive to fullerenol than the multinuclear SW480 cells and the multinuclear SW480 cells exhibit a stronger drug-resistance than the mononuclear SW480 cells.

A new MNPs implantation method was developed in this research, which enables the FITC-MNPs functioned tip to insert into cells so that MNPs are implanted into the target cells. Fluorescence microscope images show that the FITC-MNPs are released into the cells successfully. Cells being treated with MNPs (Cell-MNPs) manipulation

methods are explored by magnet and controllable electromagnets to manipulate the target cancer cells. The results show that the cell-MNPs have magnetic force manipulated capability and they can be manipulated to have the leftward, rightward, upward and downward flexibilities.

PUBLISHED WORK AS PARTS OF THIS THESIS

- ✧ Research described in **Section 2.5.1** (Synthesis of MNPs) **and Section 4.1** (Synthesis of Fe_3O_4) has been published in the paper: Qingling Meng, **Jinyun Liu**, Chao Zhang and Zuobin Wang*. (2015) Chemical synthesis and characterization of Fe_3O_4 magnetic nanoparticles. IEEE International Conference on Manipulation, Manufacturing and Measurement on the Nanoscale (IEEE 3M-NANO), 12-15.

- ✧ Research described in **Section 3.1** (Differential MFM Imaging Method) has been published in the paper: Ying Wang, Zuobin Wang*, **Jinyun Liu** and Liwei Hou. (2015) Differential magnetic force microscope imaging, Scanning, 37: 112-115.

- ✧ Research described in **Section 3.2** (Compensation by Scanning Directions) has been published in the paper: **Jinyun Liu**, Miao Yu, Yingmin Qu, Wenxiao Zhang, Yinxue Fan, Zhengxun Song, Renxi Qiu, Dayou Li* and Zuobin Wang*. (2017) Compensation of the magnetic force imaging by scanning directions, Micron.102:15-20.

- ✧ Research described in **Section 3.3** (Effect of liquid in MFM imaging) has been published in the paper: **Jinyun Liu**, Zuobin Wang*, Renxi Qiu and Dayou Li*. (2017) Effect of liquid on the magnetic force microscope imaging. IEEE International Conference on Manipulation, Manufacturing and Measurement on the Nanoscale (IEEE 3M-NANO), DOI: 10.1109/3M-NANO.2017.8286332.

- ✧ Research described in **Section 4.2** (Helical Curve Path for MNPs Lifting up) has been published in the paper: **Jinyun Liu**, Wenxiao Zhang, Yiquan Li, Hanxing Zhu, Renxi Qiu, Zhengxun Song, Zuobin Wang* and Dayou Li*. (2017)

Mechanical manipulation of magnetic nanoparticles by magnetic force microscopy, Journal of Magnetism and Magnetic Materials, 443:184-189.

- ✧ Research described in **Section 4.3** (External Magnetic Field Aided MNPs Releasing) has been published in the paper: Chao Zhang[#], **Jinyun Liu**[#], Qingling Meng, Wenxiao Zhang, Ying Wang, Dayou Li and Zuobin Wang*. (2017) Cleaning of contaminated MFM probes using a BOPP film and external magnetic field, Micron, 97:1-5.

- ✧ Research described in **Chapter 5** (Selection of cancer cells through investigating morphological features and mechanical properties) has been published in the paper: **Jinyun Liu**, Yingmin Qu, Guoliang Wang, Xinyue Wang, Wenxiao Zhang, Jingmei Li, Zuobin Wang*, Dayou Li* and Jinlan Jiang*. (2017) Study of morphological and mechanical features of multinuclear and mononuclear SW480 cells by atomic force microscopy. Microscopy Research and Technique. DOI: 10.1002/jemt.22950

ACKNOWLEDGEMENTS

I would like to express the deepest grateful to my families, my parents and husband, for their continuing support, encouragement and selfless love throughout my PhD.

I would like to extend sincere thanks to Professor Zuobin Wang for providing a large amount of guidelines and useful information. Without his help, I would not have achieved my study goals.

I would like to express extreme gratitude towards my supervisors, Professor Dayou Li and Doctor Renxi Qiu, for their guidance, support and encouragement, and their endeavour throughout this work. They are both outstanding advisors. I have learned a tremendous amount from them, not only in science, but also about ideas and skills that will be invaluable in my professional life.

True appreciation is given to the International Research Centre for Nano Handling and Manufacturing of China (CNM) for providing me an opportunity to carry out the experiments. Many thanks for the members of CNM, including Professor Zhengxun Song, Mrs Jiaolan Liu, Mrs Yingmin Qu, Mrs Miao Yu, Mr Li Li and all the members for helping me during my studies.

LIST OF CONTENTS

LIST OF PUBLICATIONS

Journal Papers

1. **Jinyun Liu**, Wenxiao Zhang, Yiquan Li, Hanxing Zhu, Renxi Qiu, Zhengxun Song, Zuobin Wang* and Dayou Li*. (2017) Mechanical manipulation of magnetic nanoparticles by magnetic force microscopy, Journal of Magnetism and Magnetic Materials, 443, 184-189.

2. **Jinyun Liu**, Yingmin Qu, Guoliang Wang, Xinyue Wang, Wenxiao Zhang, Jingmei Li, Zuobin Wang*, Dayou Li* and Jinlan Jiang*. (2018) Study of morphological and mechanical features of multinuclear and mononuclear SW480 cells by atomic force microscopy, Microscopy Research and Technique, 81(1), 3-12.

3. **Jinyun Liu**, Miao Yu, Yingmin Qu, Wenxiao Zhang, Yinxue Fan, Zhengxun Song, Renxi Qiu, Dayou Li* and Zuobin Wang*. (2017) Compensation of the magnetic force imaging by scanning directions, Micron, 102, 15-20.

4. Chao Zhang[#], **Jinyun Liu**[#], Qingling Meng, Wenxiao Zhang, Ying Wang, Dayou Li and Zuobin Wang*. (2017) Cleaning of contaminated MFM probes using a BOPP film and external magnetic field, Micron, 97, 1-5.

5. Ying Wang, Zuobin Wang*, **Jinyun Liu** and Liwei Hou. (2015) Differential magnetic force microscope imaging, Scanning, 37, 112-115.

6. Yingmin Qu, Zuobin Wang*, Feihu Zhao, **Jinyun Liu**, Wenxiao Zhang, Jingmei Li, Zhengxun Song and Hongmei Xu. (2018) AFM-detected apoptosis of

hepatocellular carcinoma cells induced by American Ginseng root water extract, Micron, 104, 1-7.

7. Lanjiao Liu, Wenxiao Zhang, Li Li, Xinyao Zhu, **Jinyun Liu**, Xinyue Wang, Zhengxun Song, Hongmei Xu and Zuobin Wang*. (2017) Biomechanical measurement and analysis of colchicine-induced effects on cells by nanoindentation using an atomic force microscope, Journal of Biomechanics, 67, 84-90.

International Conference Papers

1. **Jinyun Liu**, Zuobin Wang and Dayou Li*. (2018) A developed magnetic force microscope, Proc. EMBEC&NBC2017, IFMBE Proceedings, 64, 362-365, Singapore.

2. **Jinyun Liu**, Zuobin Wang*, Renxi Qiu and Dayou Li*. (2017) Effect of liquid on the magnetic force microscope imaging, Proc. IEEE 3M-NANO, 33-35.

3. Yingmin Qu, **Jiuyun Liu**, Guoliang Wang, Zhengxun Song and Zuobin Wang. (2017) Controlled manipulation of TRAIL into single human colon cancer cells using atomic force microscope, Proc. IEEE 3M-NANO, 345-348.

4. Ying Wang, Feifei Wang, Tingting Huang, Fenfen Guo, Ying Xie, **Jinyun Liu**, Zhengxun Song and Zuobin Wang. (2017) Manipulation of magnetic nanoparticles by optically induced dielectrophoresis, Proc. IEEE 3M-NANO, 325-328.

5. Feifei Wang, Ying Wang, Tingting Huang, Fenfen Guo, **Jinyun Liu**, Zhengxun Song, Zhankun Weng* and Zuobin Wang*. (2017) Stretching of DNA molecules on mica surfaces by magnetic field, Proc. IEEE 3M-NANO, 174-177.

6. **Jinyun Liu**, Zuobin Wang*, Yingmin Qu, Guoliang Wang, Dayou Li and Carsten Maple. (2013) Effect of fullerenol on the morphology features of SW480 cells, Proc. IEEE 3M-NANO, 27-30.

7. Qingling Meng, **Jinyun Liu**, Chao Zhang and Zuobin Wang*. (2015) Chemical synthesis and characterization of magnetic nanoparticles, Proc. IEEE 3M-NANO, 12-15.

8. Guoliang Wang, Zuobin Wang*, **Jinyun Liu**, Yingmin Qu and Yang Liu. (2013) Large area AFM imaging in liquids, Proc. ISOT, 28-30.

LIST OF TABLES

LIST OF FIGURES

LIST OF ABBREVIATIONS

AFM	atomic force microscope
ANOVA	one-way analysis of variance
BOPP	biaxiably-oriented polypropylene
Cell-MNPs	cells treated with MNPs
CNT	carbon nanotube
DC	direct current
DOX	doxorubicin
DMSO	dimethylsulfoxide
EBD	electron-beam deposition
FBS	fetal bovine serum
FIB	focused ion beam
FITC	fluorescein isothiocyanat
FITC-MNPs	FITC fluorescein functioned Fe_3O_4@SiO_2 MNPs
FluidFM	fluidic force microscope
GUI	graphical user interface
MNPs	magnetic nanoparticles
MRI	magnetic resonance imaging
MFM	magnetic force microscope
MCLs	magnetite cationic liposomes
MTT	methyl thiazolyl tetrazolium
NIRF	near-infrared fluorescence
PBS	phosphate buffer saline

PEG	polyethylene glycol
PSD	position sensitive detector
QI	quantitative imaging
SNR	signal to noise ratio
SPM	scanning probe microscope
STM	scanning tunnelling microscope
SPIONs	superparamagnetic iron oxide nanoparticles
SEM	scanning electron microscope
XRD	X-ray diffractometer

LIST OF NOMENCLATURE

$\Delta\varphi$	phase shift
φ_R	reference phase
φ_D	detected phase
$f_R(t)$	reference signal
$f_D(t)$	detected signal
Q	quality factor
k	spring constant
F_m/F_{mg}	magnetic force
F_m'	derivative of the magnetic force.
$\Delta\omega$	frequency shift
ω_R	reference frequency
ω_D	detected frequency
ω_0	resonant frequency
ΔA	amplitude shift
A_R	reference amplitude
A_D	detected amplitude
A_0	amplitude of free oscillations
μ_0	magnetic permeability of free space
$M(r')$	magnetization of the volume element in the tip
$H(r+r')$	stray field from the sample to the tip
m	effective dipole moment of the tip
F'	magnetic force in the Z direction of the tip

m_z	effective dipole moment in the Z direction
m_s	equivalent magnetic moment of the sample
H_s	stray magnetic field
H	constant of Hamaker
H_c	mean curvature
E_v	van der Waals interaction energy
C	equivalent coefficient
Z	interatomic distance
R_1, R_2	radius of sphere
ρ_1, ρ_2	molecular density of sphere
d	distance between the centres of two spheres
ΔP	pressure difference
Γ	interfacial energy
F_{van}	van der Waals force
F_c	capillary force
F_L	Laplace term of the capillary force
F_T	interfacial tension term of the capillary force
θ_1	contact angle at the object side
Φ	slope of the object
F_e	electrostatic force
ε_0	vacuum permittivity
V	potential difference
d	distance between two objects
φ_1	phase shift from the first scan
φ_2	phase shift from the second scan

φ_0	phase shift introduced by the magnetic forces
φ_{B1}	phase shift introduced by the background forces in the first scan
φ_{B2}	phase shift introduced by the background forces in the second scan
φ_{N1}	noise distribution in the first scan
φ_{N2}	noise distribution in the second scan
$\Delta\varphi_{0^\circ}$	phase shift obtained with the scanning direction of 0 °
$\Delta\varphi_{45^\circ}$	phase shift obtained with the scanning direction of 45 °
$\Delta\varphi_{90^\circ}$	phase shift obtained with the scanning direction of 90 °
$\Delta\varphi_c$	phase shift of compensation results
F_r	resistance force against the particle to move
$F_{t\text{-}p}$	force between the tip and particle
$F_{s\text{-}p}$	force between the surface and particle
F_{tv}	van der Waals' force between the tip and particle
F_{sv}	van der Waals' force between the surface and particle
F_{tc}	capillary force between the tip and particle
F_{sc}	capillary force between the surface and particle
$f_{s\text{-}p}$	adhesive force between the substrate surface and particle
F_g	gravity of the particle
F_{tot}	total interaction force
F_v	tangential force
F_p	push force
F_a	adhesive force between the magnetic particle and BOPP film
ΔL	deflection of the cantilever
E	Young's modulus
v	Poisson's ratio

δ	indentation depth

CHAPTER 1

INTRODUCTION

1.1 Rational and Motivation

Due to their unique physiochemical features such as high reactivity, high surface area and biocompatibility [1], magnetic nanoparticles (MNPs) have been widely investigated for cancer diagnosis and treatment [2], target cancer cells capture and detection [3, 4], drug delivery [5, 6], and magnetic resonance imaging (MRI) [7, 8].

Magnetic force microscope (MFM), developed based on the idea of atomic force microscope (AFM), has become a powerful tool for detecting and manipulating magnetic samples with nano resolutions [9]. Because of the properties of MNPs, MFMs have been used to study the features of biological samples after being treated with MNPs, including the DNA [10, 11], molecules [12, 13], bacteria and cells [14].

According to the researches published in [15-18], cancers such as lung cancer, liver cancer, stomach cancer, colorectal cancer and breast cancer are the leading causes of death worldwide. In 2015, 8.8 million people died, nearly 1 in 6 deaths, in cancer. Cancer treatment has become one of the top priorities in health. Great efforts have been devoted to the diagnosis and therapy of cancers.

Culturing cells with drugs is a common method used to investigate cancer therapy in experiments [19]. However, the application of this method to cancer treatment is

traditionally limited because of lack of capabilities of handling cells, targeting specific cells and measuring the nanoscale changes in cell structures to tailor treatments. With MNPs and MFM, it becomes possible to implant MNPs into cancer cells, to target treat cancer cells and to measure the changes of cancer cells during the treatment. Therefore, they are significant to cancer treatment.

1.2 Problem Definition

The manipulation of MNPs with MFM, in terms of implanting MNPs into target cancer cells, is challenging.

- High-quality MFM imaging. Before manipulating magnetic objects, their MFM images are needed. The quality of MFM imaging refers to resolution, image contrast, signal to noise ratio (SNR) and accuracy. MFM images with high resolution, high SNR, high image contrast and high accuracy could precisely show the features of magnetic materials. Many efforts have been made to improve the MFM image resolution, but how to increase the image contrast, SNR and accuracy is still to be explored.

- Flexible manipulation of MNPs. The flexible implant of MNPs into the target cancer cells using MFM involves picking up MNPs with the magnetic probe of MFM and then separating them from the tip surface and releasing into cells. Whereas how to pick the MNPs up and separating them from the tip surface is still to be investigated.

- Selection of target cancer cells. To tailor the treatment, some cancer cells with MNPs implanted should be selected and targeted. The morphological and mechanical features of cancer cells reflect cells' viability and drug-resistance. But for multinuclear and mononuclear cells, how these features changed after the drug treated is still unclear. Thus, these features of multinuclear and mononuclear cells need to be measured and analysed to provide evidences to select the target cancer cells.

- Implanting MNPs into the target cancer cells. To specifically treat the target cancer cells, the MNPs should be manipulated into the target cancer cells. But how to manipulate the MNPs into the target cancer cells successfully is still to be investigated.

1.3 Aim and Objectives

The aim of this research is to develop techniques of implanting MNPs into target cancer cells and techniques of manipulating cell-MNPs using MFM, enabling culturing cancer cells with drugs for investigating specific treatments of cancer.

The objectives of this research are:

- To develop imaging methods to improve MFM imaging quality.

- To develop MNPs manipulation techniques to pick up MNPs by MFM probe and separate the MNPs from the tip surface.

- To investigate the morphological features and mechanical properties of cells after they are treated with anticancer drugs for the selection of target cells.

- To implant the MNPs into the target cancer cells.
- To study the toxicity of MNPs on the cancer cells.
- To flexibly manipulate the target cells (treated with MNPs) with magnetic forces.

1.4 Thesis Structure

The rest of the thesis is divided into 7 chapters.

Chapter 1 gives the rational and the motivation of the research presented in this thesis. It also states the aim and the objectives of the research, as well as the structures of this thesis.

Chapter 2 introduces the fundamental theories of the research and represents the results of a literature review. This chapter firstly describes the principle of MFM and force detection. It, then, reviews the applications of MNPs in biology, including drug delivery, MRI and tissue engineering. Finally, this chapter presents the analysis results on the methods of MFM imaging quality improvement, MNPs synthesis and manipulation, cell feature investigation and drug delivery to cells using MNPs.

Chapter 3 gives the details of the methods for improving the MFM imaging quality. First, this chapter represents a differential MFM imaging method through switching the magnetization direction of MFM tip from upward to downward to increase the image contrast and SNR of MFM image. Second, it discusses a compensation MFM imaging method that uses three different scanning directions of $0°$, $45°$ and $90°$ to increase the accuracy of the MFM imaging. Third, the chapter analyses the effect of

the liquid on the MFM imaging to obtain MFM images in liquid environments.

Chapter 4 presents the method of synthesis and manipulation of MNPs. The first is the chemical co-precipitation method to synthesis of MNPs. The second is the method of picking up MNPs by allowing MFM tip to follow a helical curve as the capture path. Finally, this chapter reports the method for separation of the MNPs from tip surface, which is proposed using a BOPP film together with an external magnetic field. All the methods are developed in this research.

Chapter 5 investigates the changes of the morphological features and the mechanical properties of cancer cells to provide recommendations for selecting the target cells. In this chapter, the morphological features including height, roughness, length and width, and mechanical properties including adhesive force and Young's modulus are investigated after the treatment with anti-cancer drug fullernol to understand their drug-resistance capability difference.

Chapter 6 demonstrates MNPs implanting and cell-MNPs manipulation methods developed in this research. The MNP implanting method allows implanting MNPs into target cells using the magnetic probe. The method of cell-MNPs manipulation employs controllable electromagnetic magnets and enables flexible and controllable movement of cell-MNPs. Furthermore, for investigating MNPs' toxicity, cell viabilities of SMCC-7721 and HL-7702 cells are studied. To evaluate the magnetic force manipulated capability of cell-MNPs, the cells untreated and treated with MNPs are manipulated with magnet are studied.

Chapter 7 concludes the works and comments on future researches.

CHAPTER 2

BACKGROUND KNOWLEDGE AND LITERATURE REVIEW

2.1 Magnetic Force Microscope

Scanning probe microscope (SPM) was invented in the 1980's [20, 21]. The first generation is scanning tunnelling microscope (STM), being used to measure the conducting electric current characters of materials [22] at atomic scale. Atomic force microscope (AFM) is the latest generation of SPM. It was invented by G. Binnig in 1986 [23]. AFM has been used to produce images of topographic, conducting, magnetic and ultrasonic features of samples with nano scale resolutions. AFM used in imaging and manipulation of the magnetic samples is also called magnetic force microscope (MFM).

MFM has been proved as a very powerful tool to investigate magnetic domain patterns, domain walls and magnetic vortices [24]. Fig. 2.1 is the schematic diagram of a typical MFM system. The system consists of piezoelectric (PZT) scanner, micro stage, nano stage controller, micro stage controller, AD and DA convertors, computer based data processing analysis unit, phase lock loop, tip driver, piezoelectric bimorph, probe, laser and position sensitive detector (PSD) [25]. The PZT scanner can move with a nano resolution whilst the micro stage scanner can move with a micro resolution. They are controlled by the nano stage controller and the micro stage

controller, respectively. Both controllers are programmable so that the scanners can scan samples in different ways to best obtain their topographical and magnetic images. The probe is fixed on the piezoelectric bimorph that is controlled by the tip driver so that the cantilever of the probe can be oscillated. The movements of the probe are captured by the laser and PSD in the form of optical signal. The phase locked loop used to obtain the shift signals for MFM imaging. The AD convertor receives the signal from PSD and convers these analogue signal to digital signal and passes on it to the computer based processing and analysing unit. The DA convertor converts the digital control signal to analogue signal and feeds the signal to micro/nano controllers.

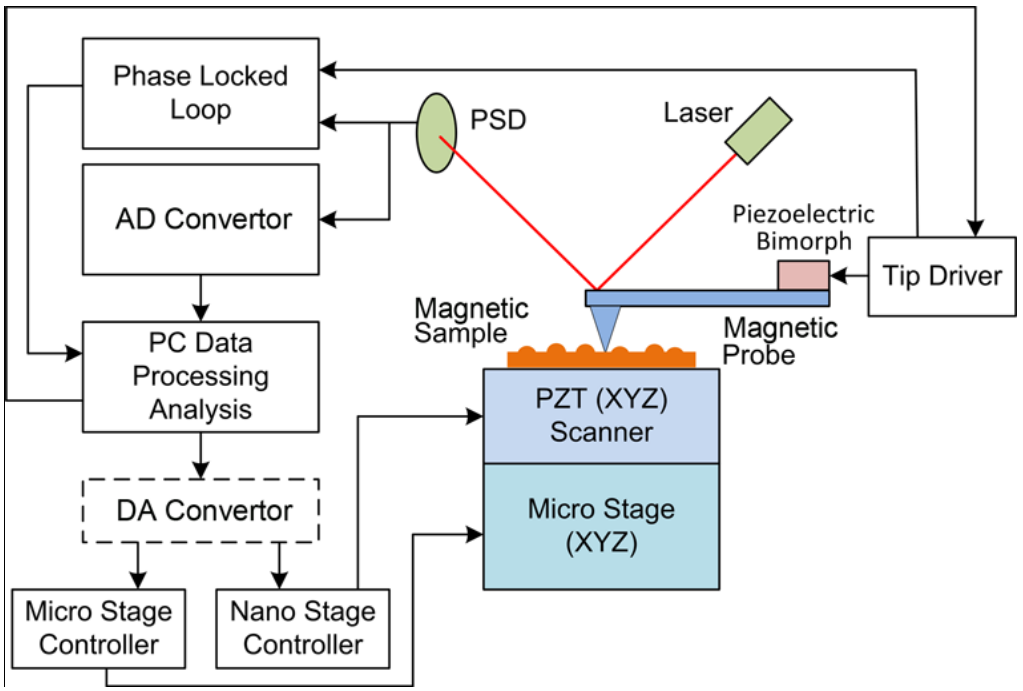

Fig. 2.1 Schematic diagram of MFM.

The probe, laser and PSD form an optical path for detecting the change of the topographical features of samples and the interaction forces between the samples and the probe. The wave length of the used laser is ~670 nm to avoid the damage to the biological samples. The attractive or repulsive forces between the sample and the tip

causes the probe cantilever deflect towards or away from the sample surface, as Fig. 2.2 shown. The angle of the reflected laser beam changes due to the cantilever deflections, and there are different positions of the spot on the PSD. The PSD consisted with four quadrants and the position of laser spot can be computed in two directions [25]. The deflection in the vertical direction can be calculated through comparing the signals from the "Top" half and "Bottom" half of the activity area of PSD, and it has $V_{T-B}=(V_A+V_B)-(V_C+V_D)$. The lateral twisting of the cantilever can be calculated through comparing the "Left" half and "Right" half of the activity area of PSD, and it has $V_{L-R}=(V_A+V_c)-(V_B+V_D)$. The sum output voltage is $V_{SUM}=V_A+V_B+V_C+V_D$.

MFM imaging is to obtain the long-range magnetic force information of samples. Tapping mode is the main scanning mode for MFM to collect the information. Two successive scans are operated in the lift-tapping mode [26], as shown in Fig. 2.2. The lift-tapping mode is developed from the tapping mode by lifting the tapping probe several nanometers to measure the long-range force [24, 27].

The first scan aims to have the topography of samples. It is performed by tapping at a resonant frequency and by detecting the deflection of the probe cantilever. The second scan aims to obtain the magnetic force map. This is performed by lifting probe several nanometers above the sample (ΔZ) and by tracing the topography profile obtained in the first scan [28, 29]. The long-range magnetic force information is realized by measuring the force gradient between the sample and the magnetic probe, and the magnetic domain distributions will be shown in the MFM image. The change of the force gradient will lead a linear change of phase shift, or resonance frequency shift or amplitude of an oscillation cantilever [30]. Accordingly, the force gradient change is

obtained through calculating the shift between the detected signal ($f_D(t)$) extracted from PSD and the reference signal ($f_R(t)$) used for driving the probe cantilever working in a tapping mode [24]. The details will be described in the next section.

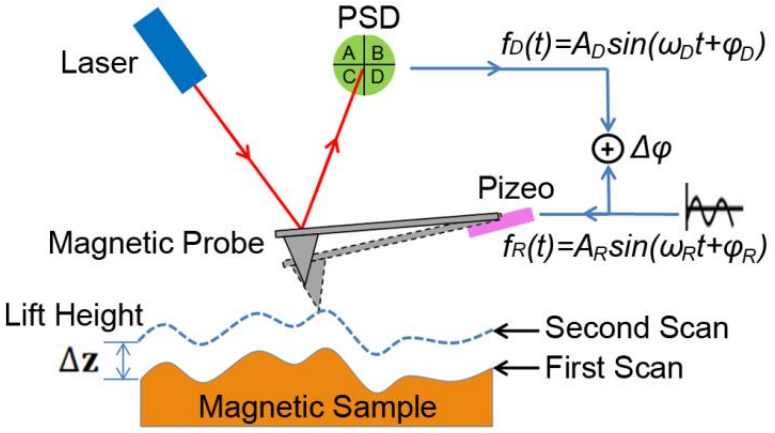

Fig. 2.2 Schematic diagram of an MFM imaging system.

MFM carries out the first scan along a line and then immediately the second scan on the same line, and repeats this line by line. Fig. 2.3 illustrates the process. Starting from the start point, MFM undertakes the first scan along the first line (X-axis) from the left to the right, and then lifts the tip up dozens of nanometers and performs the second scan from the right to the left along the same line. The MFM then moves the tip to the second line along Y axis and repeats the same along the second line. It repeats the same to all lines until the sample is scanned.

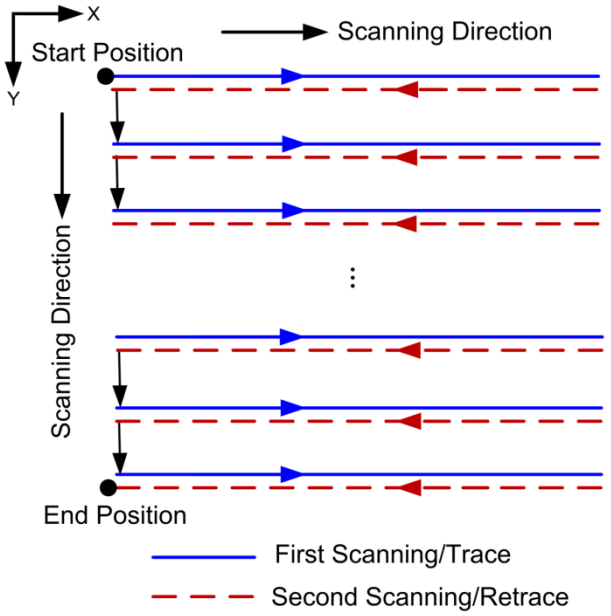

Fig. 2.3 Illustration of the MFM scanning process.

Fig 2.4 provides flow chart of the scanning process. In the "Parameters Setting" block, parameters, including scanning pixels, scanning range, scanning speed, proportional gain, integral gain, working amplitude, working frequency, setpoint and lift height are set. After setting these parameters, the "Tip Approaching" process is started by driving the tip closing to the sample surface step by step and the process will be stopped until the tip contacted the surface.

After the tip approached, the "Start Scanning" button on the graphical user interface (GUI) is clicked to activate the scanning thread (dotted line frame). Then the tip will tapping at the set frequency and amplitude to scan the sample. "iFast" is a variable to record the number of the scanned points in the X-axis. For the first point to be scanning of the first line, there is "iFast=0". "iFastScope" is the total points (X-axis pixels) will be scanned in the X-axis. The scanner will be moved to scan the next point if "iFast< iFastScope" is true and the value of the "iFast" will plus one by execution instruction of "iFast++". It repeats until all of the points in this line is

scanned and have “iFast=iFastScope”. The first scan of the first line is finished. Then the tip lifts up to the set height (“Lift iHeight”) and performs the second scan. The value of the “iFast” reduced one after scanned the point and the instruction of “iFast--” is implemented. Until all of the points have been rescanned and the “iFast>0” is fail. The first line has been finished scanned by these two successive scanning. Then “Save Data Send to GUI” block is working to save the collected data and scanning thread send image and curve updated message to update the scanning image and oscillograph curve of GUI.

“iSlow” is a variable to record the number of the scanned points in the Y-axis and its initial value is “iSlow=1”. “iSlowScope” is the total lines (Y-axis pixels) that will be scanned in the Y-axis. The scanner will be moved to scan the next line if “iSlow<iSlowScope” is true. The tip declined to the sample surface (“Decline iHeight”), and the value of the “iSlow” will plus one by execution instruction of “iSlow++”. The X-axis scanning will be repeated. Until “iSlow<iSlowScope” is fail, the scanning has been finished.

If there is a need to stop the scanning process, click the “Stop” button on the GUI and the scanning thread will be stopped. Then the “Clear Cache” is working to prepare the space for the next time scanning. The scanning process is finished.

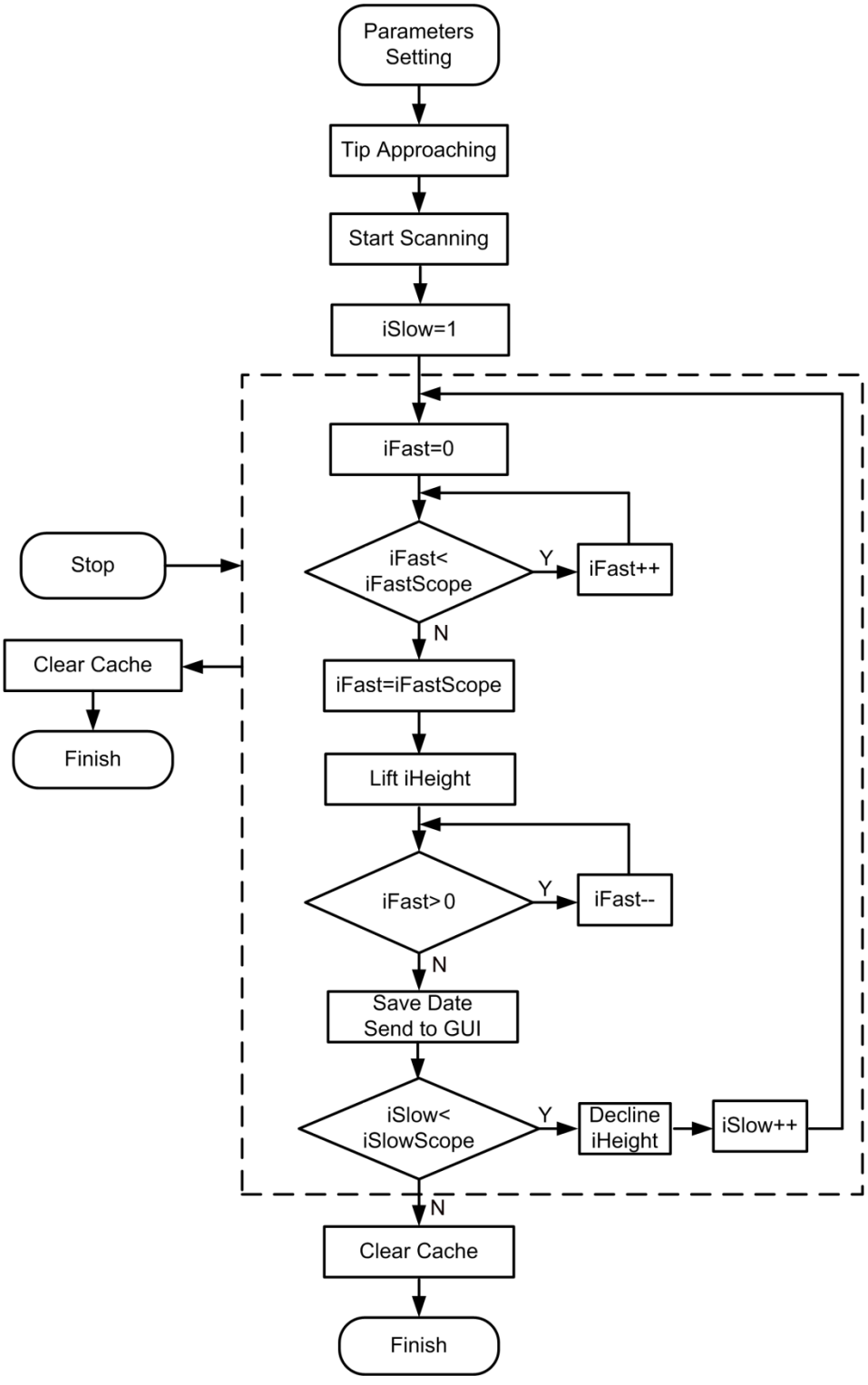

Fig. 2.4 Diagram of the MFM system scanning.

2.2 Magnetic Force Detection

For MFM imaging and manipulation, magnetic force and van der Waals force are the two main forces acting on the magnetic tip [31]. The magnetic force between the probe and sample is a long-range force and varies according to the distance between the tip and sample. The van der Waals force is a short-range force and always exists in the measurement process. As this force is also always ubiquitous between atoms or molecules, sample surface topography can be obtained by the detection of the van der Waals force.

During micro/nano manipulation and assembly with MFM, there will be the so called distance or surface forces generated between sample and probe, causing the deformation of the probe cantilever, producing adhesive force between the two objects when they contact to each other [32, 33]. Capillary force and electrostatic force are two surface forces. The capillary force dominates the entire micro/nano world range from a few nanometres to several millimetres. The electrostatic force exists even if the sample is non-charged because of the triboelectrification.

2.2.1 Magnetic Force

The magnetic force of sample that can be detected by MFM is magnet static. It is possible for MFM to measure the forces between the magnetic probe and the sample [34]. Because of the high sensitivity and stability, the detection of the force gradient through phase shift, or resonance frequency shift or amplitudes shift, of an oscillation cantilever is most commonly used for MFM imaging [30].

Phase shift $\Delta\varphi$ imaging method records the phase signal of every point of the scanned area. The phase shift $\Delta\varphi$ is proportional to the derivative of the magnetic force between the tip and sample in the *Z*-direction. It can be given in Eq. (2.1) [35, 36]

$$\Delta\varphi = \varphi_R - \varphi_D = \frac{Q}{k} F_m' \tag{2.1}$$

where, φ_R is the reference phase of the reference signal $f_R(t)$ which is used for driving the pizeo in a tapping mode. φ_D is the detected phase of the detected signal $f_D(t)$ which is obtained from the PSD. Q is the quality factor and k is the spring constant of the cantilever. F_m' is derivative of the magnetic force.

The force gradient between the tip and sample will cause a frequency change of the tapping cantilever. If the cantilever detects an attractive force gradient, the frequency shift $\Delta\omega$ can be calculated as Eq. (2.2) [37]

$$\Delta\omega = \omega_R - \omega_D = \omega_0 F_m' / 2k \tag{2.2}$$

where, ω_R is the reference frequency of the reference signal $f_R(t)$ which is used for driving the pizeo in a tapping mode. ω_D is the detected frequency of the detected signal $f_D(t)$ which is obtained from the PSD. ω_0 is the resonant frequency of the probe cantilever.

The resonant frequency shift can be expressed by the oscillation amplitude if the oscillation frequency choose at the steepest portion of the resonance frequency curve and higher than the ω_0 simultaneously. The amplitude shift ΔA can be calculated using Eq. (2.3) as suggested in [34, 38].

$$\Delta A = A_R - A_D = (2A_0 Q / 3\sqrt{3}k) F_m' \tag{2.3}$$

where, A_R is the reference amplitude of the reference signal $f_R(t)$ which is used for driving the pizeo in a tapping mode. A_D is the detected amplitude of the detected signal $f_D(t)$ which is obtained from the PSD. A_0 is the amplitude of free oscillations of the cantilever.

The forces detected by MFM are purely magnetic static forces and they depend on the interactions of the magnetic dipole moments of the magnetic tip and sample [39]. The magnetic force acting on a volume element dV' on the tip is described in the following [37]

$$dF_m = \mu_0 \nabla(M(r') \cdot H(r + r'))dV' \tag{2.4}$$

where, μ_0 is the magnetic permeability of free space, $M(r')$ is the magnetization of the volume element in the tip, and $H(r+r')$ is the stray field from the sample to the tip. The model is shown in Fig. 2.5 [39]. r and r' refer to the tip apex coordinate and the internal coordinate, respectively. The tip can be a simple point probe that has a magnetic element. The magnetic force is given by [40]

$$F_m = \mu_0 \nabla(m \cdot H) \tag{2.5}$$

where, m is the effective dipole moment of the tip.

F' is the magnetic force in the Z direction of the tip and it is detected by the cantilever of the probe. F' can be calculated by Eq. (2.6) as given in [41].

$$F' = \frac{dF_m}{dz} = \mu_0 m_z \frac{\partial^2 H_z}{\partial z^2} \tag{2.6}$$

where, it is assumed that the tip is magnetized in the vertical direction and m_z is the

effective dipole moment in the Z direction.

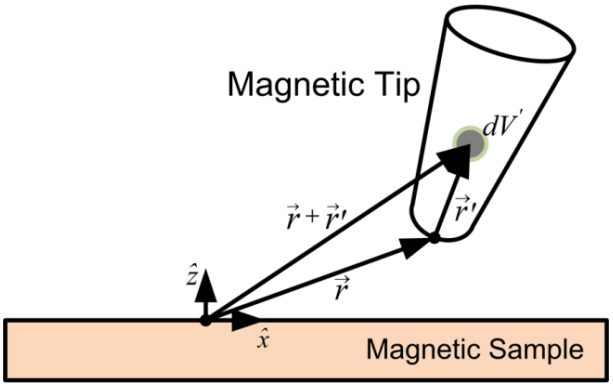

Fig. 2.5 Geometry of magnetic tip used for calculating the interactive force [42].

The stray magnetic field of the magnetic particle is expressed in Eq. (2.7) [41]

$$\mathrm{H}_s(r)_{r>a} = \frac{1}{4\pi}\left[-\frac{\mathrm{m}_s}{r^3} + \frac{3(\mathrm{m}_s \cdot \mathrm{r})}{r^5}\right] \tag{2.7}$$

where, r is the radius vector of which the start point is in coincidence with the sphere center, a is the sphere radius, and m_s is the equivalent magnetic moment of the sample. The instantaneous m_s depends on the material magnetization intensity and the sphere volume, which can be expressed as Eq. (2.8) [40].

$$m_s = 4\pi a^3 M\hat{n} / 3 \tag{2.8}$$

where, n is the unit magnetization vector specified the orientation.

2.2.2 The van der Waals Force

The van der Waals force is a short-range force with the property of superposition and can be obtained by adding together or integrating all of the van der Waals forces. The model is shown in Fig. 2.6. The energy of interaction between atoms is given by [43], such as

$$E_v = -C / Z^6 \tag{2.9}$$

where, C is the equivalent coefficient determined by the incentive, orientation and dispersion effects, and Z is the interatomic distance.

The van der Waals interaction energy can be described as

$$E_v = -\frac{H}{6}\left[\frac{2R_1R_2}{d^2-(R_1+R_2)^2} + \frac{2R_1R_2}{d^2-(R_1-R_2)^2} + ln\frac{d^2-(R_1+R_2)^2}{d^2-(R_1-R_2)^2}\right] \tag{2.10}$$

where, R_1 and R_2 are the radius of spheres, d ($d=R_1+R_2+Z$) is the distance between the centres of two spheres, H is the constant of Hamaker ($H=\pi^2\rho_1\rho_2C$), and ρ_1 and ρ_2 are the molecular densities of spheres.

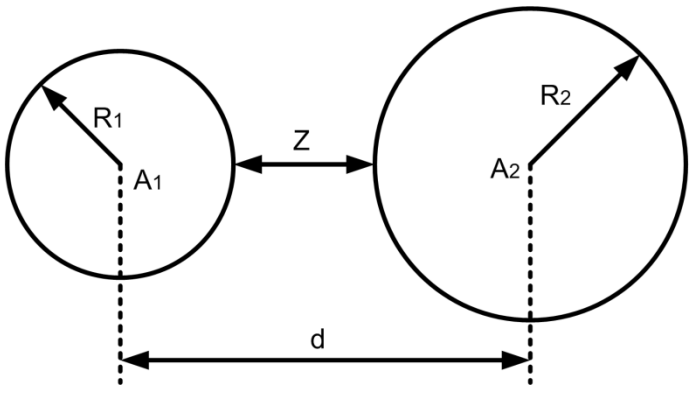

Fig. 2.6 Model of van der Waals force between two spheres [43].

If $Z << R_1$ and R_2, the van der Waals force can be simplified as

$$F_{van} = -\frac{\partial E_v}{\partial Z} = -\frac{HR_1R_2}{6Z^2(R_1 + R_2)} \tag{2.11}$$

If R_2 is infinite and $Z << R_1$, the van der Waals force can be written as

$$F_{van} = -\frac{HR_1}{6Z^2} \tag{2.12}$$

2.2.3 Capillary Force

Capillary force has two components. They are the negative pressure along the axis of the liquid bridge and the surface tension of the solid sphere in the vertical direction. A liquid bridge system is constituted when there is liquid between the sphere and the object [32]. Fig. 2.7 shows the surface tension model of a sphere and a plane.

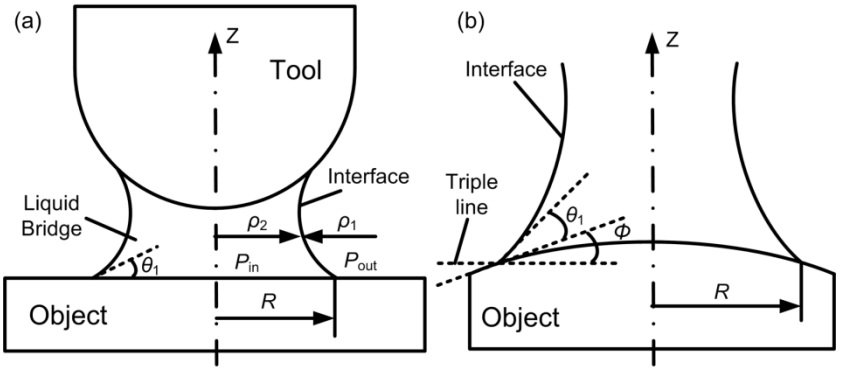

Fig. 2.7 Model of the tension force between the surface of sphere and plane [32]. (a) Effects of the liquid bridge linking the two objects. (b) Details of the tension force.

Capillary force refers to the pressure difference (ΔP) across the curved liquid bridge interface and it can be expressed as Eq. (2.13) [32].

$$\Delta P = P_{in} - P_{out} = 2\gamma H_c \tag{2.13}$$

where, γ is the interfacial energy between the object and the liquid surface. H is the mean curvature of the crescent liquid bridge interface, which is defined as Eq. (2.14) [44].

$$H_c = \frac{1}{2}\left(\frac{1}{\rho_2} - \frac{1}{\rho_1}\right) \tag{2.14}$$

where, ρ_1 and ρ_2 are the main curvature radius of the interface.

According to the analysis of the capillary force of the solid sphere, the Laplace term of the capillary force F_L that acts on the wetted area $A_L=2\pi R^2$ of the solid sphere, can be expressed as Eq. (2.15) [32].

$$F_L = \Delta P A_L = 2\gamma H_c \pi R^2 \tag{2.15}$$

where, R is the radius of the liquid bridge at the object side.

The interfacial tension term of the capillary force F_T acting on the perimeter of the wetted region can be expressed as Eq. (2.16) [32].

$$F_T = 2\pi R\gamma \sin(\theta_1 + \phi) \tag{2.16}$$

where, θ_1 is contact angle at the object side and Φ is the slope of the object at the location of the triple line.

The total capillary forces of liquid effect on the solid spheres and the plane can be expressed as Eq. (2.17).

$$F_c = F_L + F_T = 2\pi R\gamma(H_c R + \sin(\theta_1 + \phi)) \quad (2.17)$$

2.2.4 Electrostatic Force

Coulomb forces are also called electrostatic forces in the micro/nano world. No matter the objects are conductor or not, surface charges will be generated by triboelectrification and the electrostatic forces are discontinuous [45]. When the radius of a sphere is far greater than the distance between these two objects ($R>>d$), the electrostatic force between the charged sphere and plate can be expressed as Eq. (2.18) [33, 46].

$$F_e \approx \frac{3\pi\varepsilon_0 R V^2}{4d} \quad (2.18)$$

where, ε_0 is vacuum permittivity, R is the sphere radius, V is the potential difference and d is the distance between these two objects.

2.3 Applications MNPs in Biology

Due to the unique physiochemical features of MNPs, they have been widely investigated for drug delivery [47], MRI [7, 48], tissue repair, immunoassay, anticancer magnetic hyperthermia and cell separation [49].

2.3.1 Drug Delivery

The vehicle for drug delivery requires that the carriers have the ability to release the

drug carried at the aimed position and cure the lesion location without any side effect on the healthy tissues [50]. Because of their unique physicochemical properties and ability [51], MNPs can be used for drug delivering and concentrating to the target lesion location by the effect of external magnetic field [52].

Since found the magnetic polymer can be used as carriers in the 1970s, a large number of magnetic nano/micro-particles have been used for delivering drugs to the aimed location in vivo due to their magnetic field responsiveness [53]. Because of the excellent biocompatibility, acceptable stability and simple surface functionalization [54], magnetic liposomes have been developed to be drug carriers and stimuli-sensitive nano devices manipulated by the external magnetic field [55]. For example, the drug release properties of doxorubicin (DOX) loaded MNPs encapsulations were depends on the changes of temperature and pH [56].

Chao et al. [57] investigated the application of polyethylene glycol (PEG) modified Gold-MNPs (PGMNPs) as the vehicle to deliver the DOX in vitro, and evaluates the curative efficiency of DOX-conjugated PGMNPs in vivo through an external magnetic field. Verma et al. [58] deliveried the quercetin-loaded MNPs to the target lung cancer cells through nebulization method and evaluated the feasibility and biocompatibility. The results indicated that growth of the lung cancer cells could be efficient inhibited by the quercetin-loaded MNPs. Streptokinase and activator of tissue plasminogen were taken by the nanocarriers of SiO_2-MNPs for investigation of the targeted thrombolytic therapy by Tadayon et al. [59], as shown in Fig. 2.8. The results found that the hemorrhagic side effects were prevented because of the high protein-loading efficiency and activity retention of SiO_2-MNPs. Tarasi et al. [60] used the MNPs to deliver the docetaxel to HEK293 normal cells, HeLa cells and

MDA-MB-231 cells and evaluated their viability. The results show that MNPs were non-cytotoxicity and the proliferation of HeLa and MDA-MB-231 cells were significantly decreased by this method.

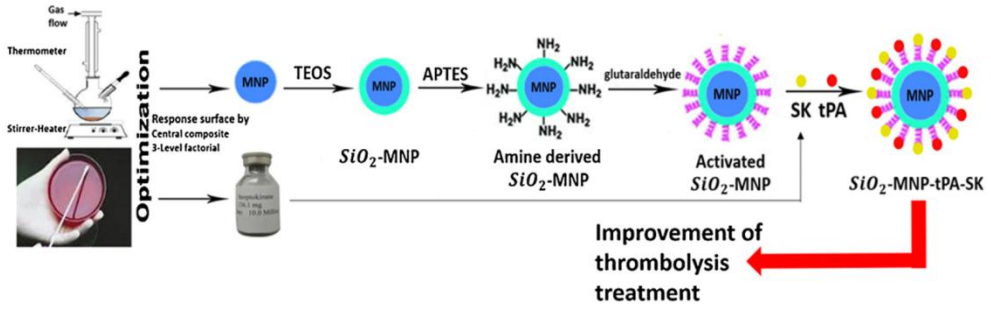

Fig. 2.8 Strategy of the experimentation [59].

Nowadays, how to effectively deliver the drug to the target action sites and increase drug diffusion pass biological barriers were still problems for the conventional methods and need to be further developed. Delivery of drugs through nanoparticles could overcome these problems.

Further research is needed to concentrate on the optimal dosage to the treatment of cancer. With the targeting ability of MNP enhanced continuously, MNPs hold great expects in the applications of drug delivery to treatment of cancer.

2.3.2 Magnetic Resonance Imaging

Due to the biodegradability, low toxicity and low impact on cell functionality of MNPs, they have been used for labelling and tracking cells by MRI [61]. MRI supplying high-resolution anatomical images with noninvasive. It has been widely used to diagnose malignant and healthy tissues [62].

Compared with other MRI agents, such as chelates of paramagnetic ions [63], superparamagnetic iron oxide nanoparticles (SPIONs) are excellent because of their stronger contrast. It can be found from T_2-weighted images of hypointense [64, 65] that SPIONs could be rapidly insulated by the splenic and hepatic macrophages.

Bierry et al. [66] enhanced MRI through SPIONs to investigate the macrophage infiltration in knee synovial inflammation area of the rabbit. After injection of SPIONs to eight rabbits, $T_1/T_2/T_2$*-weighted images were obtained and found that the SPIONs were mainly gathered together in the infarcted area where the macrophages were heavily localized. Baraki et al. [67] labelled granulocytes by SPION and observed acute inflammation of soft tissue in rats by MRI. The work provided new opinions to specificity and sensitivity investigated the infectious processes in early stage. Chen et al. [68] used PEG-Cy5.5 functioned MnO MNPs (MnO-PEG-Cy5.5) to take MRI and near-infrared fluorescence (NIRF) images and found that brain tumor was visually detected and contrast was significantly enhanced by MnO-PEG-Cy5.5 MNPs, as shown in Fig. 2.9.

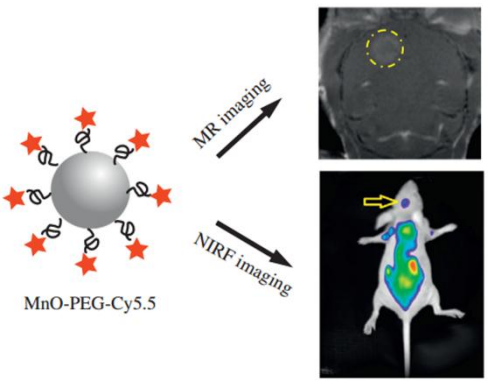

Fig. 2.9 Images of MR and NIRF after the treatment of the MnO-PEG-Cy5.5 [68].

2.3.3 Tissue Engineering

Tissue engineering is an interdisciplinary area. It integrates the cell biology, medicine and engineering purposing of specific cell regeneration to functional tissues and organizations [69, 70]. Tissue engineering uses the biocompatible microstructure in 2D or 3D construction to confirm these cells can well attachment, growth, differentiation and proliferation [71, 72]. Tissue engineering technique depends on magnetic force has been explored by MNPs and magnetite cationic liposomes (MCLs) for the purpose of providing magnetic characters to the specific cells [73].

Cell 3D constructions for tissue engineering often with complex structures and shapes, and those can be configured through magnetic force. Ito et al. [74] seeded cells incubated together with MCLs onto ultralow-attachment plates for 24 hours under the effect of a magnet to form a sheet. Then a magnet with cylindrical shape was rolled onto the sheet, due to the magnetic attraction a tubular structure formed. In another study, Oshima et al. [75] percutaneously injected the ferumoxide nanoparticles labelled rabbit bone marrow-derived mesenchymal stromal cells and then gathered these cells into the ceramic to fill the bone defect through magnetic fields. The results have shown that this technique enhances bone formation significantly.

It can be concluded that the tissue engineering technique that depends on magnetic force was a potential method for bone defects/fractures treatment and vascular tissue construction [76, 77]. The magnetic field intensity was the crucial point and it has significant effect on the cell depth when seeding them into the constructions [78, 79].

2.4 MFM Imaging Quality Improvement

MFM has been developed for researching the precise characters of magnetic properties by a magnetic probe [38, 80, 81]. Because of the nanoscale resolution of MFM [82-84], it has been used as a powerful tool to observe the magnetic microstructure distributions of various magnetic materials [85-89] and manipulate the magnetic objects [90-92]. Therefore, how to obtain good quality MFM images has attracted attention. The quality of MFM imaging refers to the accuracy and resolution of the images. There are mainly three factors that are related to the accuracy and resolution, namely, tip shape, tip magnetisation direction and distance between the tip and sample. Accordingly, research in improving the quality has been carried out from these three aspects.

2.4.1 Tip Shape

The topography of samples has a significant impact to MFM imaging because MFM tip traces the topography with several nanometres above the samples in scanning. The geometry and size of MFM tip are also important parameters as it decides the resolution and the accuracy of the obtained topography images [93]. The ideal tip is a point that is sharp enough to record the true sample surface. However, in practice it is difficult to obtain the ideal tip due to the limited by the technics, methods and parameters in the fabricate processing. Accordingly, the distortion images of the topography were inevitably acquired due to the tip shape of the profile, as shown in Fig. 2.10.

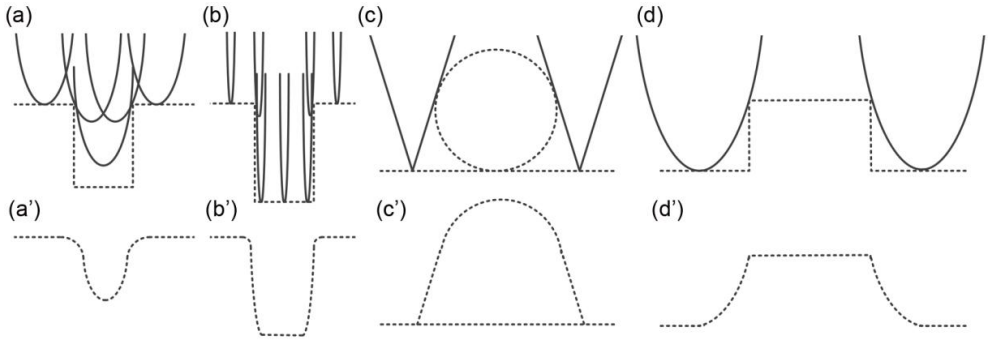

Fig. 2.10 Effect of geometry and size of tip on topography imaging [94]. (a) is the illustration of measurement by a larger circular arc tip with the cone shape and (a') is the topography obtained by the tip. (b) is the illustration of measurement by a smaller circular arc tip with the cone shape and (b') is the topography obtained by the tip. (c) is the illustration of measurement by a larger angle tip with the pyramid shape and (c') is the topography obtained by the tip. (d) is the illustration of measurement by a larger angle tip with the cone shape and (d') is the topography obtained by the tip.

To improve the accuracy of MFM imaging, techniques for specially fabricated MFM tips with a sharper shape have been developed, including used focused ion beam (FIB), electron-beam deposition (EBD) and carbon nanotube (CNT) [95].

Memmert et al. [96] modified the MFM tips using the EBD technique to acquire the highest resolution by reduce tip perturbation influence on soft magnetic structures. Koblischka et al. [97] employed FIB to prepare MFM tip with high-aspect ratio to acquire high resolution MFM images. The results show that the spatial resolution was improved and the perturbations effect was decreased with the prepared MFM tip. The resolution of the magnetic structures was improved to 20 nm. Huang et al. [98] used FIB to fabricate high performance tips and measured the magnetic structures of hard disk, as shown in Fig. 2.11. The regular magnetic domains were clearly recognized in

both MFM images. The phase shift signals obtained by the modified MFM probe are more accuracy than signals obtained by conventional MFM tip. The results indicated that the sharpen MFM tip could significantly improve the resolution of the MFM images.

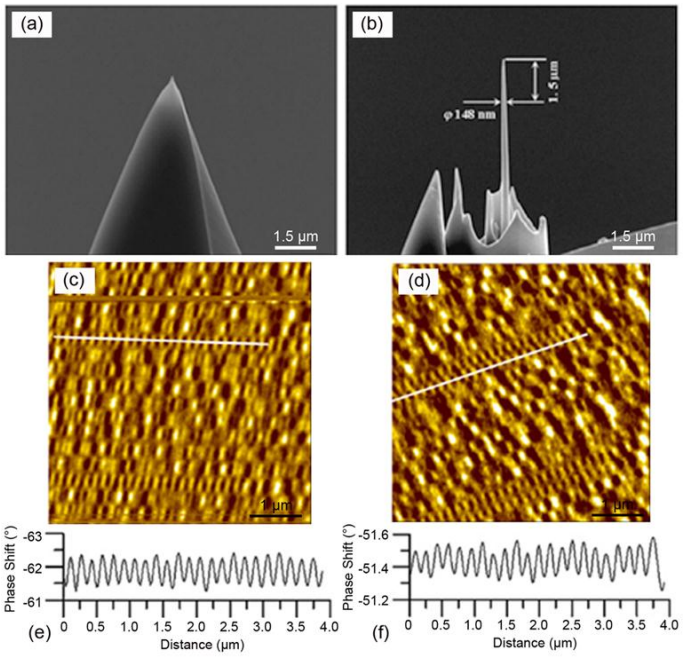

Fig. 2.11 Si-based probe and MFM images of hard disk [98]. (a) is the tip before FIB fabricated and (b) is the tip after FIB milling and CoCr film coating. (c) is an MFM image obtained by a conventional MFM tip. (d) MFM image obtained by the modified MFM tip. (e) and (f) are signal line profiles extracted from (c) and (d).

Choi et al. [99] developed $Co_{90}Fe_{10}$-coated CNT as the probes. To obtain the best MFM images, the ferromagnetic $Co_{90}Fe_{10}$ films with thickness of 20~50 nm were used to coat the CNT and obtained MFM images. The results found that 40 nm $Co_{90}Fe_{10}$-coated tip could obtain highest resolution MFM images. Wolny et al. [100] adhered an iron filled CNT (FeCNT) with a length of ~8 μm and diameter of ~20 nm onto the conventional MFM tip for changing the shape of the tip to obtain high

resolution MFM images. They found that the FeCNT can be used as a magnetic monopole and it is an excellent tool for MFM imaging and manipulation of low magnetic fields samples.

It can be found that the tip shape has been sharpened and the accuracy of the sample has been improved with the above methods. However, the tip shape modified techniques cannot be popularized to every laboratory because the equipment cost is high. In addition, the simplex tip shape modified methods are limit to image the magnetic sample with the complex magnetic domains and lead to a distortion of the magnetic domain structures which is parallel to the scanning direction.

2.4.2 Tip Magnetization

In addition to tip shapes, the probe magnetized direction can also be considered in improving MFM image quality. This is because MFM imaging depends on the interactive forces between the magnetic tip and sample [101]. The related works on different magnetized angles of magnetic tip effects on MFM imaging were investigated.

Alekseev et al. [30] magnetized the tip under some angle with respect to the Z-axis by an external magnet and measured the samples, the results as shown in Fig. 2.12. The experimental and theoretical results were shown that the signals of attractive and repulsive forces were strongly affected by the angle of the tip magnetization, and the samples with strong magnetic fields also influenced the magnetized directions of the tip in the scanning. Rice et al. [102] applied magnetic field at various angles to magnetize the tip and hard disk used as sample to observe the effect of tip

magnetization on magnetic features. The results shown that vertical magnetized tip could obtain higher resolution MFM images. Saito et al [103] calculated the tip magnetized directions with different angles and found that with tip magnetization directions changed, the attractive and repulsive forces regions were changed simultaneously.

It is known that the stability of the tip magnetization is not guaranteed if the samples are with strong magnetic fields [30]. Thus, the tip magnetization techniques are limited to image the samples with stronger magnetic fields, and the simplex magnetization changed techniques cannot improve the SNR of the MFM images and improve the accuracy of the samples with complex magnetic domain directions. Chapter 3 presents an innovative method to solve this problem.

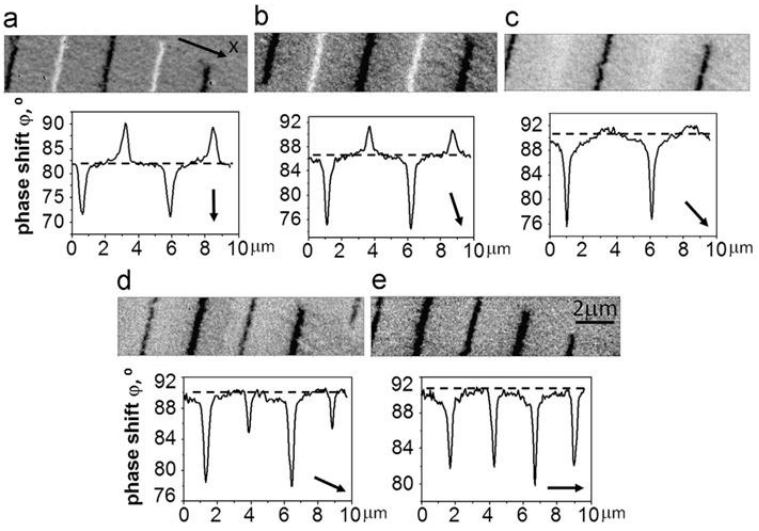

Fig. 2.12 MFM images and their corresponding cross-sections obtained by the pre-magnetized tip with different magnetized angles [30]. (a) Tip was magnetized with 0 °. (b) Tip was magnetized with 20 °. (c) Tip was magnetized with 45 °. (d) Tip was magnetized with 70 °. (e) Tip was magnetized with 90 °. Arrows indicated the magnetized angles and the lift height was 20 nm.

2.4.3 Lift Height

The magnetic force is a long-range force between the magnetic probe and sample [25]. Thus, the distance between the probe and sample determines the quality of MFM images. Many researches have been made to study the effect of lift height on MFM imaging.

Nyamjav et al. [104] analysed the MFM images quality of the DNA coated by Fe_3O_4 MNPs with various lift heights of magnetic probes ranging from 5 nm to 50 nm and found that lift height above 20 nm cause a very small and weak magnetic properties of MNPs, but the MNPs could be clearly observe with the lift height below 10 nm. To obtain the best MFM images quality, Nenadović et al. [105] studied the magnetic fields images with tip under various lift height. And the results showed that the optimized lift height was between 60-80 nm and the MFM images with a lower distortion and higher kurtosis. Huang et al. [98] investigated the MFM images definition and signals sensitivity by magnetic tip at different lift heights. It can be seen that the best quality of MFM image signal were obtained with a lift height of 40 nm. The signals' definition of MFM images were decreased with the increase of lift height, as shown in Fig. 2.13.

It can be seen that a single scan of the sample is used in different lift height MFM imaging processes without the selection of specific scanning directions. Accordingly, this will lead to a distortion of the magnetic domain structures which is parallel to the scanning direction. Chapter 3 presents an innovative method to solve this problem.

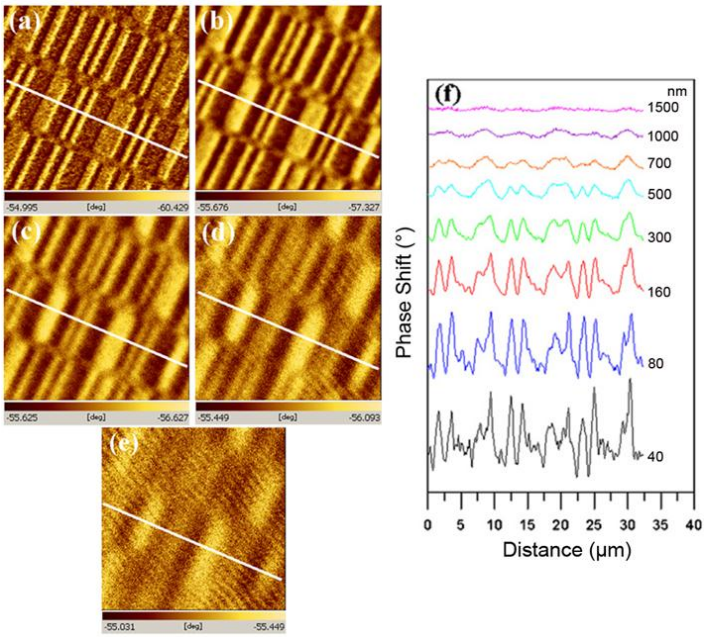

Fig. 2.13 MFM images of hard disk acquired by various lift heights [98]. (a) Obtained with 40 nm. (b) Obtained with 400 nm. (c) Obtained with 700 nm. (d) Obtained with 1000 nm and (e) Obtained with 1500 nm. (f) Cross-section profiles.

2.5 MNPs Synthesis and Manipulation

2.5.1 Synthesis of MNPs

Techniques for synthesis of MNPs have been developed in last decades because of their unique characters and a number of clinical trials have been conducted to study potential applications of MNPs in biomedicine. Various methods including electron beam lithography, thermal decomposition, hydrothermal method and chemical co-precipitation have been developed to obtain MNPs [106, 107]. MNPs magnetic characters are influenced by the particles shape and size, and how to precisely control the particles' shape and size is still a challenge. Table 2.1 compared the methods for

the synthesis of MNPs.

Electron beam lithography method involves emitting an electron beam with a certain frequency on a substrate that is covered with a layer of iron particles and the iron particles are then converted into MNPs because of oxidation reaction caused by the electron beam [106]. This method has difficulties in controlling the particle size due to the beam intensity and resist sensitivity and in collecting the particles because the MNPs are grown on the substrate surface [108].

Table 2.1 Comparison of methods for the synthesis of MNPs [106, 109].

Technique / Criteria	Electron Beam Lithography	Thermal Decomposition	Hydrothermal Method	Chemical Co-precipitation
Size Distribution	relatively small	small	very small	relatively small
Controllable Shape	not good	good	very good	not good
Reaction Period	milliseconds-seconds	hours-days	hours-days	minutes-hours
Condition	electron beam emitted	high temp (100-320 ℃)	high temp (>200 ℃); high pressure (>2000 psi)	20-90 ℃

Thermal decomposition method obtained the MNPs by decomposed the organometallic compounds to iron atom under high temperature and then the iron atom transfer to iron oxides by the oxidation reaction. The ratios of organometallic compounds, surfactant and solvent decide the size and shape of the synthesized MNPs.

The size and shape of the particles are easy to control, but it is easy to transfer to γ-Fe_2O_3 MNPs in the process of synthesis the Fe_3O_4 MNPs and the obtained particles are only dissolved in nonpolar solutions generally [106, 107, 109].

The hydrothermal method is through growing the metal nucleation to form the MNPs under high temperatures and pressures. The reactions take place with aqueous media in reactors or autoclaves at a temperature higher than 200 ℃ and pressure higher than 2000 psi [110]. With this method, the particle size and shape are easy controlled by adjust the parameters in reaction, such as the temperature, pressure and reaction time. However, it is difficult to meet such experimental conditions in an ordinary laboratory because the equipment cost is high.

Chemical co-precipitation method is through added a base (e.g. NaOH) in the mixed salts solution of the Fe^{2+} and Fe^{3+} to obtain the iron oxide nanoparticles (Fe_3O_4) in aqueous environments. This method is considered the simplest [111]. It is efficient in synthesizing Fe_3O_4 under the condition of a proper temperature, PH and ionic strength [112]. In the synthesis process, the type of the salt and the ratio of Fe^{2+}/Fe^{3+} used were determined the size and shape of particles [109]. However, in ambient environment, magnetite nanoparticles are unstable and easy to oxidation and formed the maghemite (γ-Fe_2O_3). Thus, processing conditions need to be controlled to complete the reactions and obtain the Fe_3O_4 MNPs.

2.5.2 Manipulation of Nanoparticles

Currently, the common manipulation operations of single nanoscale objects using AFM/MFM include pushing, rolling, cutting, drilling, dissecting and reversing

[113-115]. Pushing and sliding of nanoscale particles are mainly performed along linear paths from one location to another location on surfaces [115-117].

Korayem et al. used AFM tip to push, roll and slide gold nanoparticles with spherical shapes [116] and manipulated the nanoparticles with cylindrical geometries [113] on silicon substrate to study of the critical parameters in the nanomanipulation. Sitti et al. [117] moved the nanoparticles in 2D based AFM and simulated the pushing operation. Guo et al. [118] pushed the polystyrene nanoparticle by AFM tip to make it moving on the silicon substrate to study the frictions in the movement, as shown in Fig. 2.14.

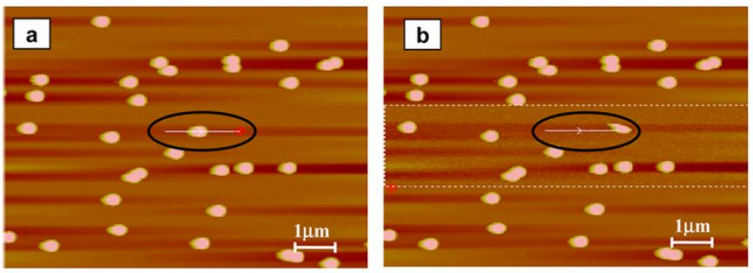

Fig. 2.14 Pushing a polystyrene nanoparticle on silicon by AFM probe [118]. (a) Before pushing and (b) after pushing.

Based on the AFM, the MFM is developed for the study of magnetic domain structures on the submicron/nanometer scale [119]. Besides the observation of magnetic structures, MFM is commonly used for the manipulation and measurement of magnetic samples [35]. In addition, it has been used for the manipulation of MNPs.

Chang et al. [120] reversed the magnetization of magnetic nanoparticles with the inhomogeneous magnetic field produced by the magnetic tip. Baronov and Andersson [41] tracked a magnetic nanoparticle by MFM tip in three dimensions and a tracking control law was developed for the magnetic tip retained adjacent to the target magnetic particle. Pinilla-Cienfuegos et al. [91] manipulated individual molecules

based on magnetic nanoparticles with an average size of 25 nm by MFM. In their work, external magnetic fields were increased from -600 Oe to +600 Oe to transfer the magnetization of the MNPs and the magnetization reversal processes were recorded, as shown in Fig. 2.15. The results showed that the MNPs have been fully reversed at +600 Oe and this work increased the application of the MNPs in information storage.

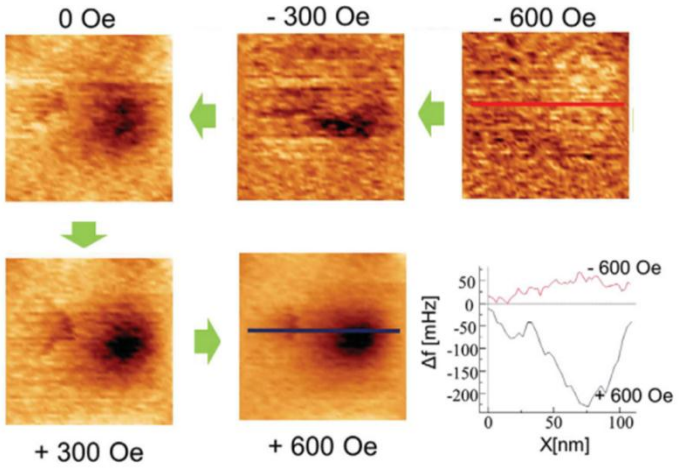

Fig. 2.15 Manipulation of the KNiCr MNPs by changing the coercive fields [91].

For the particles with disordered and complicated distributions, it is hard to design a simple straight line path for the tip to push a selected particle to the target location. In practice, the linear path should be precisely determined for each operation, and it is difficult to be successfully performed. Due to the limitation of the tip radius, reliability and reposition precision of the AFM/MFM system, flexible manipulation of particles with a size below 100 nm is still a challenge [117]. In addition, interaction forces between the substrate surface and the particle are difficult to overcome in the vertical direction, leading to the difficulties in separating MNPs from the surface and in lifting them up with simple tip approaching and retracting. New methods of MNPs manipulation are needed.

2.6 Cells Features Investigation

Cancer treatment has been an important issue and endeavours have been made to the diagnosis and therapy of cancers [121, 122]. Because of the nanoscale resolution of AFM in the imaging, manipulation and measurement of biological objects and biological structures [123-128], it has been used to investigate morphological and mechanical features of living cells [129-132]. Thus, AFM can be a proper tool for the manipulation and measurement of cancer cells and providing a guideline in the target cancer cells selection. Studies about the changes of morphological and mechanical features of cancer cells after the treatment with anti-cancer drugs were conducted.

Gaspar et al. [133] studied the effect of human neutrophil peptide-1 on PC-3 cells and MOLT-4 cells by AFM, and the results showed that the height decrease was caused by the HNP-1 treatment. The roughness of the cell membrane was related to the cell motility, and it can be used to characterize the state of cells [134, 135]. Kim et al. [136] found by AFM that the roughness of HeLa cells was increased significantly after the treatment with paclitaxel. Pelillo et al. [137] investigated the adhesion and morphology features of HCT-116 cancer cells to study their metastatic behaviours affected by ruthenium drug NAMI-A. Hayashi et al. [138] and Ansardamavandi et al. [139] evaluated the stiffness changes of cancer cells to understand the pathophysiology. Efremov et al. [140] characterized the cell area, focal adhesion and Young's modulus distributions of tumor cells and normal cells with AFM to study their transformational changes. Hence, morphology and mechanics are significant features for the investigation of cancer cells [141, 142].

A tumour cell, often contains more nuclei [143-145]. The fusion of plasmodia [146-148], closed mitosis [149, 150] and cell division [151, 152] can lead to the coexistence of different nuclei and formation of multinuclear cells [153]. Studies have shown that multinuclear cells commonly exist in tumors and they are a key character for the diagnosis of cancer [154-156]. However, little work has been reported in the investigation of the difference of drug-resistance between multinuclear cancer cells and mononuclear cancer cells after the treatment with anticancer drugs for the purpose of effectively treatment of the cancer.

2.7 Drugs Delivery to Cells Using MNPs

Due to their biocompatibility and superparamagnetic characters, MNPs have attracted attentions and are used to deliver the drug to target treatment of the tumor cells or tissue [157]. Many efforts have been devoted to treatment of cancer cells or tissues using MNPs.

Varshosaz et al. [158] used the Dox-MNPs conjugate to the LHRH receptors of breast cancer cells MCF-7 (normal cells are low expressed LHRH receptor) to target treatment of the cancer cells by co-culture them and an external magnetic field used for releasing the drug. The results showed that the Dox-MNPs conjugated to the LHRH receptors effectively and cells viability was significantly reduced. Du et al. [159] functioned the MNPs with D-tyrosine phosphates (MNP_pY) and 40 μg/mL MNP_pY contained in the culture medium to treat the cancer cells HeLa-GFP and normal cells HS-5 to target conjugated the placental alkaline phosphatase (ALPP)

ectoenzyme of cells. Because of the over expressed of ALPP in cancer cells and none expressed in normal cells, the MNP_pY target conjugated to the cancer cells. Borroni et al. [160] intravenously injected 400 μL of lentiviral vectors loaded MNPs solutions into the tumor location of mice liver to target treatment of the tumor tissue and a magnetic field was used to affect the target location for killing the tumor cells. The results showed that the MNPs can target the cancer cells and also the normal cells.

It can be seen that the both methods of co-culturing MNPs with cells or injecting MNPs solutions into the target tissue can ensure cells carrying MNPs. However, investigation into individual cells is necessary. It enables to trace drug effects on the cells and to see inside of how the drug working in cancer cells that have different characters. Therefore, it is significant to exploiting of new therapy [161-163]. In addition, more controlled manners of getting MNPs into cells are needed so that the exact amount of drug carried by the cells can be known.

Matsuoka et al. [164] developed a robot for microinjection of the single-cell. In their robot system, the pipette was obtained by heated and pulled a glass capillary and X/Y/Z stages were handled to move the filled solution pipette to locate the target cell and inject the pipette into the cells. This microinjection method can implant the filled solution into the cells successfully. Guillaume-Gentil et al. [165] used the fluidic force microscope (FluidFM) combined a pyramidal probe to pressure the DNA fluid into the single HeLa cell through the triangular opening in side of the probe by insert the probe into the cells, as shown in Fig. 2.16. This technique can implant the fluid into cells with a high efficiency and cell viability.

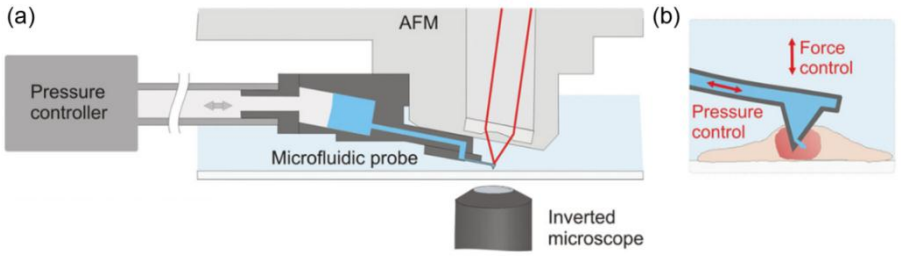

Fig. 2.16 (a) Illustration of the cell injection using FluidFM [165]. (b) Fluid implanted into the cells through a triangle opening in-side of the probe.

With above methods, MNPs can be used as the fluid or solution filled the pipette or probe to be implanted into the target cells. However, microinjection technique was limited because it was difficult to handle shape fabricated of glass micropipette and monitor the injected deeps of the probe, and the probe with a triangle opening cannot be used any more if there was a blocking inside it and the probe was with a high price. Thus, simple and effectively target cancer cells treatment techniques are still needed future investigate to study the effect of the drug on cancer cells in a more controllable way.

2.8 Summary

In this chapter, fundamental theories of MFM were briefly described firstly, including the principles of MFM and scanning method. Optical path is the significant parts to detect the deflection of the probe cantilever and it is consist with probe, laser and PSD. In MFM imaging, a lift-tapping mode was used and this was performed by two successive scans. The first scan obtained the topography images and the second scan obtained the magnetic force map by tracing the topography profiles. The magnetic

forces, van der Waals forces, capillary forces and electrostatic forces in MFM working were introduced. The magnetic and van der Waals forces are always exists in the measurement process. The capillary force dominates the entire micro/nano world and the electrostatic forces involves because of the triboelectrification.

Then, the applications of MNPs in biology were reviewed, including the drug delivery, MRI and tissue engineering. Because of their superparamagnetic properties, they can be arrived the target position by controlled external magnetic fields to label or treatment of the cancer cells. But culturing cells with drugs is a common method used to investigate cancer therapy in experiments. Traditionally, the application of this method to cancer treatment is limited because of lack of capabilities of handling cells, targeting specific cells and measuring the nanoscale changes in cell structures to tailor treatments.

Next, to obtain good quality MFM images, factors affecting the MFM images resolution and accuracy were reviewed, including the tip shapes, tip magnetizations and the tip-sample distances. However, these factors improved cannot obtain high quality MFM imaging with different magnetic structures, in terms of high resolution, high image contrast, high SNR and high accuracy.

Afterwards, to implant the MNPs into the target cancer cells for the specific treatment, the synthesis and manipulation MNPs methods were observed. The advantages and disadvantages of MNPs synthesis methods were compared. Pushing or sliding of the target object is commonly used in manipulation of nanoparticles. The flexibility of the manipulations in many applications is limited and it is hard to pick up the particles by MFM probe with those methods.

To select the target cells, the morphological features and mechanical properties of cancer cells after the treatment with anti-cancer drugs were reviewed. However, little work was carried out to investigate the difference of drug-resistance between multinuclear and mononuclear cancer cells and this is significant to selection of cancer cells for the MNPs treatment.

Finally, methods of MNPs treated cells were reviewed to target the treatment of cancer cells or tissues. However, the commonly methods used in the research are co-culture/mixture the MNPs with cells or injected to the tissue of target location and these methods cannot satisfy the demand of specific treatment of the target single cells in a simple and effective way.

CHAPTER 3

MFM IMAGING QUALITY IMPROVEMENT

With the development of nano magnetic materials, devices and systems, such as magnetic nanoparticles, magnetic random access memories and perpendicular recording media, MFM has been widely used for measuring and manipulating magnetic samples [166-168]. The demand for high quality MFM imaging, in terms of high resolution, high image contrast, high SNR and high accuracy, is increasing. This chapter presents an innovative method for differential MFM imaging which increases image contrast and SNR of samples with single magnetic domain structure by switching the magnetic probe magnetization directions, and a compensation method to improve the accuracy of the MFM images of samples with complex magnetic domain structure by different scanning directions. This chapter also investigates the effects of liquid on the MFM imaging for the purpose of measuring and manipulating the magnetic samples in liquid environments.

3.1 Differential MFM Imaging Method

In this section, a method for differential MFM imaging is presented to obtain differential magnetic force images with an improved contrast and SNR. The method is based on a two-pass scanning procedure. In the first scan, the magnetic sample is scanned with the upward magnetized MFM tip to obtain the first MFM image. In the

second scan, the sample is scanned with the downward magnetized MFM tip to obtain the second MFM image. Subtraction is performed between two images to obtain the differential magnetic force image. The magnetic forces are separated from other background forces, and the quality of magnetic images is improved.

3.1.1 Principles

MFM mainly detects the magnetic interactions between the sample and the tip in the *Z* direction for the magnetic force imaging of the sample surface. Since a force gradient exists between the probe and the sample, a probe phase shift will be introduced. The phase shift can be calculated as Eq. (2.1) [35].

The distribution of the magnetic forces on the sample surface can be obtained through recording the phase shift of every scanning point when the probe scans along with the sample surface. In the scanning process, the background forces (such as the van der Waals force, the electrostatic force, and the force set during the AC tuning of cantilever) and the noises can introduce variations to the magnetic force images. Let φ_1 be the phase shift from the first scan (tip magnetized upward) and φ_2 be the phase shift from the second scan (tip magnetized downward). The phase shifts can be expressed as

$$\varphi_1 = \varphi_0 + \varphi_{B1} + \varphi_{N1} \tag{3.1}$$

$$\varphi_2 = -\varphi_0 + \varphi_{B2} + \varphi_{N2} \tag{3.2}$$

where, φ_0 is the phase shift introduced by the magnetic forces, φ_{B1} is the phase shift introduced by the background forces in the first scan. φ_{B2} is the phase shift introduced

by the background forces in the second scan. φ_{N1} is the noise distribution in the first scan and φ_{N2} is the noise distribution in the second scan.

The phase shift difference between the two scans can be calculated by

$$\Delta\varphi = \varphi_1 - \varphi_2 = 2\varphi_0 + \varphi_{B1} - \varphi_{B2} + \varphi_{N1} - \varphi_{N2} \tag{3.3}$$

When $\varphi_{B1}=\varphi_{B2}$, Eq. (3.3) can be simplified as

$$\Delta\varphi = 2\varphi_0 + \varphi_{N1} - \varphi_{N2} \tag{3.4}$$

Providing that φ_{N1} and φ_{N2} are zero mean Gaussian noise distributions and they are uncorrelated, $E(\varphi_{N1})=E(\varphi_{N2})=0$, $E(\varphi^2_{N1})=E(\varphi^2_{N2})=\sigma^2_N$, and $E(\varphi^2_{N1}\,\varphi^2_{N2})=0$.

Thus, the expectation of the noise term is

$$E(\varphi_{N1} - \varphi_{N2})^2 = 2\sigma_N^2 \tag{3.5}$$

It can be seen from Eqs. (3.4) and (3.5) that the differential magnetic force signal amplitude is doubled and the background forces are eliminated so that the SNR and the image contrast are significantly improved by differential MFM imaging.

Fig. 3.1 shows the principle of differential MFM imaging with the reversed tip magnetization. When the probe is magnetized upward, the phase shifts caused by the magnetic forces and background forces between the tip and the sample surface are shown in Fig. 3.1(a). When the probe magnetization direction is downward as shown in Fig. 3.1(b), the magnetic interactions between the tip and the sample are reversed and the background forces remain unchanged. Fig. 3.1(c) shows the differential magnetic force signal obtained by performing subtraction over the two signals in Fig.

3.1(a) and (b), and its amplitude is doubled compared with those in Fig. 3.1(a) and (b). Thus, there is a clear contrast enhancement in the differential magnetic image, as the background forces have been removed and the output signal amplitude is increased. The differential magnetic force image can be analysed similarly to the magnetic force images with the reduced or removed background forces.

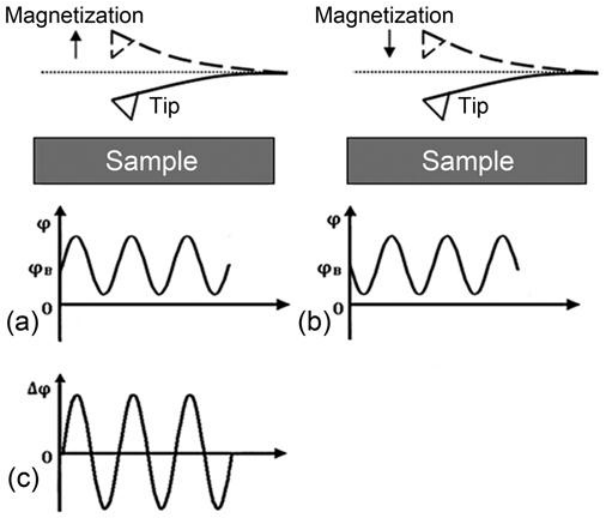

Fig. 3.1 Principle of differential MFM imaging. (a) MFM probe magnetized upward. (b) MFM probe magnetized downward. (c) Differential magnetic force signal.

3.1.2 Experiments and Discussions

A BENYUAN (CSPM-5500, China) MFM system, as shown in Fig. 3.2(a), was used to measure the magnetic structures. The cycloidal shape magnetic structure with a diameter of 2 μm was made by electron beam lithography (EBL) on a silicon wafer substrate with the nickel film thickness of 100 nm. The resonant frequency and spring constant were 75 kHz and 3 N/m of the employed magnetic probe (Multi75M-G, BudgetSensors), respectively. Fig. 3.2(b) shows the magnetic probe.

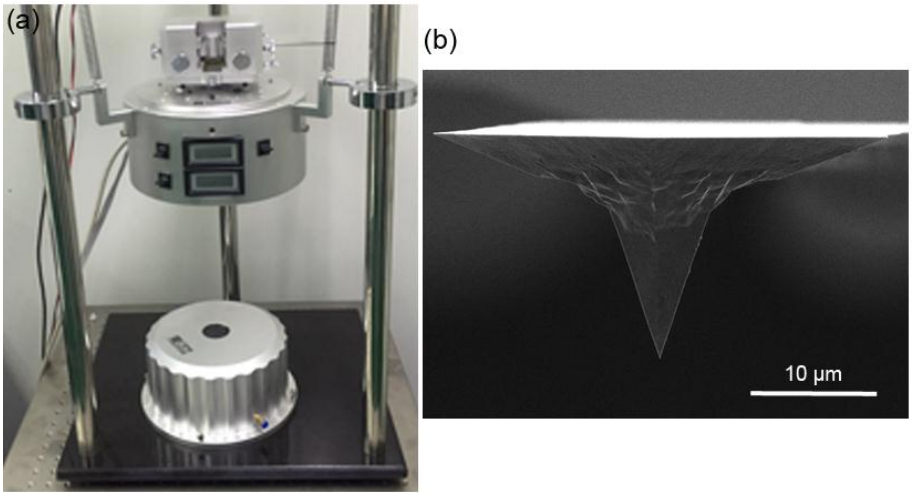

Fig. 3.2 (a) is BENYUAN MFM system and (b) is the magnetic probe.

Fig. 3.3 shows the topographic images and magnetic force images of the cycloidal shape magnetic structure. Fig. 3.3(a) and (b) are the topographic images corresponding to the magnetic images in Fig. 3.3(c) and (d) obtained with the reversed tip magnetization. Fig. 3.3(e) is the differential magnetic force image. Three selected cross-sectional curves from Fig. 3.3(c-e) are shown in Fig. 3.4. In the experiment, there were two separate magnetic images captured and the differential magnetic image was then obtained by analyzing the similarity of the images from the two scans, and the MATLAB software was used to process the images. Two standard magnets were used to magnetize the tip outside the microscope, and the tip magnetization direction was changed by reversing the magnets after the first scan.

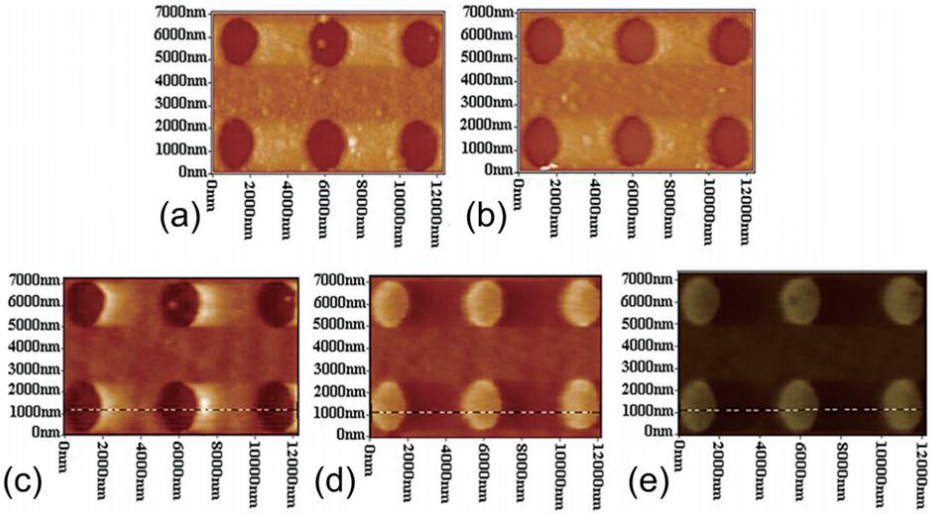

Fig. 3.3 Topographic and magnetic images of the cycloidal magnetic structures made by EBL. (a) and (b) are the topographic images corresponding to the magnetic force images (c) and (d) with reversed tip magnetization. (e) is the differential magnetic force image.

In Fig. 3.4, the curve a is extract from Fig. 3.3(c), curve b is extract from Fig. 3.3(d) and curve c is extract from Fig. 3.3(e). It can be seen that curves a and b are two mirror symmetric distributions due to the change of the magnetization direction of the tip leading to the phase inversion of the output signal, and the curve c is the difference of the curves a and b. It can be seen that the differential magnetic force signal amplitude is the sum of those from the curves a and b, and the background forces are significantly reduced. The average contrast values of Fig. 3.3(c-e) are 0.69, 0.51 and 0.86, respectively. The contrast values in the experiment are estimated by

$$Contrast = (\overline{Max} - \overline{Min})/(\overline{Max} + \overline{Min}) \tag{3.6}$$

where, $\overline{Max}$ is the average of ten maximum amplitude values, and $\overline{Min}$ is the average of ten minimum amplitude values in the images.

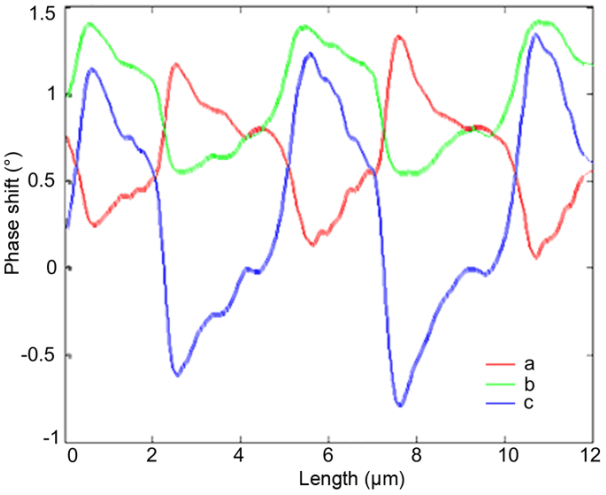

Fig. 3.4 Cross-sectional curves a, b and c from Fig. 3.3 (c), (d) and (e).

It can be seen that the SNR and the image contrast are significantly improved by differential MFM imaging. This method is useful for the improvement of the magnetic force image contrast and SNR, and for the acquisition of high quality of magnetic force images.

3.2 Compensation by Scanning Directions

A single scan of the sample is a common scanning method used for MFM imaging without the selection of specific scanning directions. For a magnetic sample with complex magnetic domain directions, the magnetic structures cannot be correctly imaged with a single scanning direction due to the errors induced by the magnetized probe. Thus, MFM images are often distorted in MFM applications. Errors can also be introduced due to the instability of the tip magnetization when the samples with strong magnetic fields.

In this section, a method is proposed to reduce the errors and structure distortions of MFM images. Three different scanning directions with the angles of 0 °, 45 ° and 90 ° are used to measure the distributions of magnetic domain structures and then averaged their magnetic force signals to obtain the compensated results. The results show that the proposed method is able to correct the distortions significantly in MFM imaging.

3.2.1 Principles

For the magnetic sample with complex magnetic domain directions, the domain structures parallel to the scanning direction are often distorted. To compensate the distortions caused by the scanning direction, scanning directions of 0 °, 45 ° and 90 °, as shown in Fig. 3.5(b), are successively operated. M_s shows the magnetic direction of the magnetic structure.

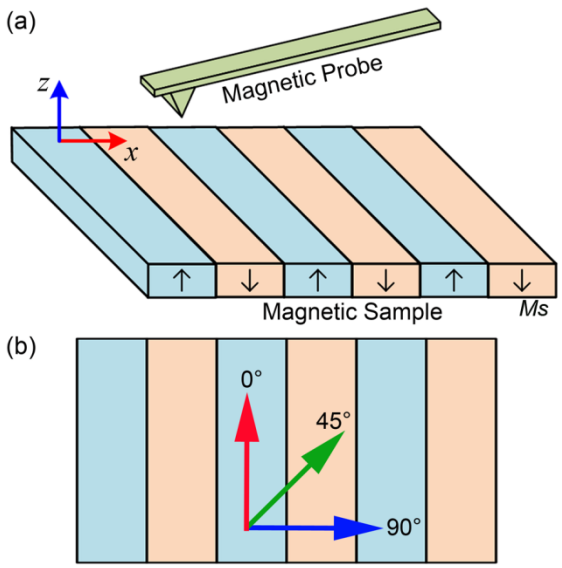

Fig. 3.5 Illustration of MFM imaging with three scanning directions on the magnetic sample. (a) The structure of the magnetic sample. (b) The scanning angles between the scanning directions and magnetic domain structures of 0 °, 45 ° and 90 °.

These three MFM images are calibrated firstly and then averaged to compensate the distorted structures. The magnetic sample also serves as the reference for the three scanning directions. The scanning direction parallel to the magnetic domain structure in the imaging is selected as the scanning direction of 0°. If the scanning direction is vertical to the magnetic structure, the scanning direction is defined as 90°. If the intersection angle between the scanning direction and the magnetic structure is 45°, the scanning direction is 45°.

Fig. 3.6 shows the procedure of calibration. Firstly, the MFM images are successively obtained with the three different scanning directions, and it is found that the magnetic domain structures parallel to the scanning direction are often distorted, as shown in Fig. 3.6(a). Secondly, the acquired MFM images are rotated to make the magnetic domain structures in the same direction, as shown in Fig. 3.6(b). A target magnetic feature area is then selected and matched with the three MFM images, as presented in Fig. 3.6(c). Next, the matched features of the three images are overlapped and the phase shift values of the matched pixels are averaged, as shown in Fig. 3.6(d). Finally, the compensated MFM image is obtained from Fig. 3.6(d), as shown in Fig. 3.6(e).

The compensation method of MFM imaging is expressed as

$$\Delta\varphi_{\mathrm{c}} = \frac{1}{3}\left(\Delta\varphi_{0^\circ} + \Delta\varphi_{45^\circ} + \Delta\varphi_{90^\circ}\right) \tag{3.7}$$

where, $\Delta\varphi_{0^\circ}$ is phase shift obtained with the scanning direction of 0°. $\Delta\varphi_{45^\circ}$ is phase shift obtained with the scanning direction of 45° and $\Delta\varphi_{90^\circ}$ is phase shift obtained with the scanning direction of 90°.

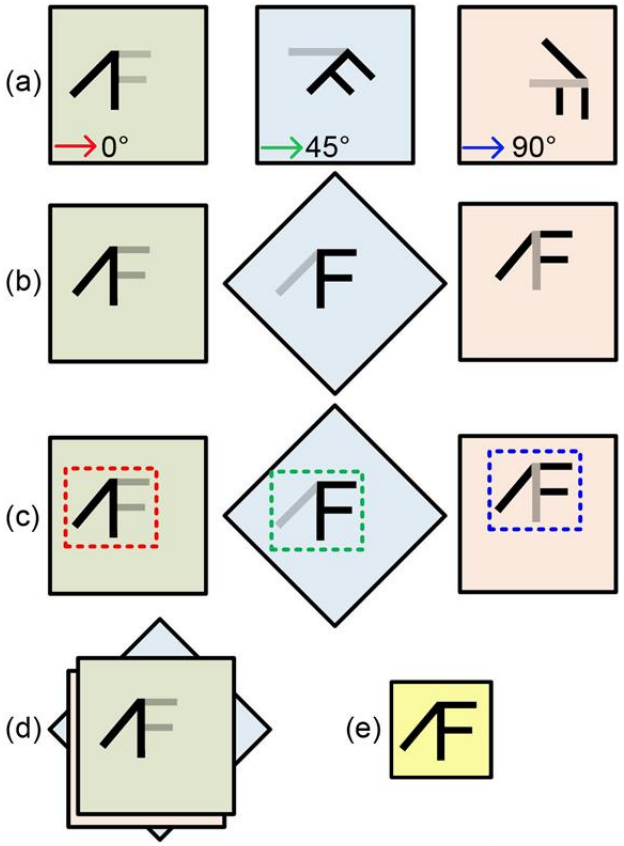

Fig. 3.6 Illustration of the calibration procedures. (a) MFM images obtained from three different scanning directions in which the arrows show the scanning directions. (b) The images rotated to ensure the magnetic domain structures in the same direction. (c) A target feature area selected and matched. (d) The matched features of the three images averaged. (e) The compensation result acquired.

3.2.2 Experiments

MFM used in the work was JPK (NanoWizard®3, Germany), as shown in Fig. 3.7, and its repeatability in x/y is 1 nm. The system was operated in a clean-room in which the temperature and humidity were precisely controlled. The lift-tapping mode was used to image the magnetic structures. The probe used in the experiments was

MagneticMulti75-G (BudgetSensors). The resonant frequency of the magnetic probe was 75 kHz and the force constant was 3 N/m. Before the experiment, the probe was magnetized vertically by an external magnetic field (500 mT) for more than 12 hours.

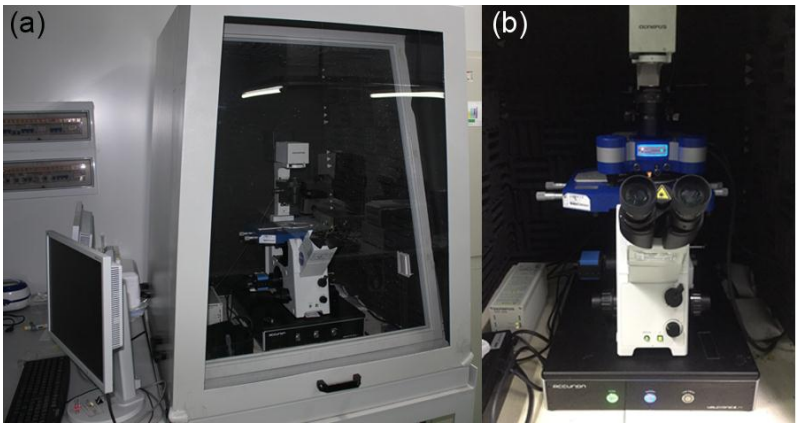

Fig. 3.7 JPK MFM system.

A hard disk with a size of 10 mm × 10 mm, a standard MFM sample purchased from BRUKER with two-direction magnetic structures, and a magnetic sample with the magnetic structures aligned in four directions were used as samples to investigate the effect of scanning directions on MFM imaging. The MATLAB software was used to process the images.

3.2.3 Results and Discussions

The phase shift signals were used in imaging the hard disk with scanning directions of 0 °, 45 ° and 90 °, as shown in Fig. 3.8. In the experiment, the lift height was 30 nm. It can be seen that the features of MFM images with the scanning direction of 0 ° is undistinguished in Fig. 3.8(a). However, periodic magnetic domain structures are clearly recognized with the scanning directions of 45 ° and 90 °, as shown in Fig. 3.8(b, c).

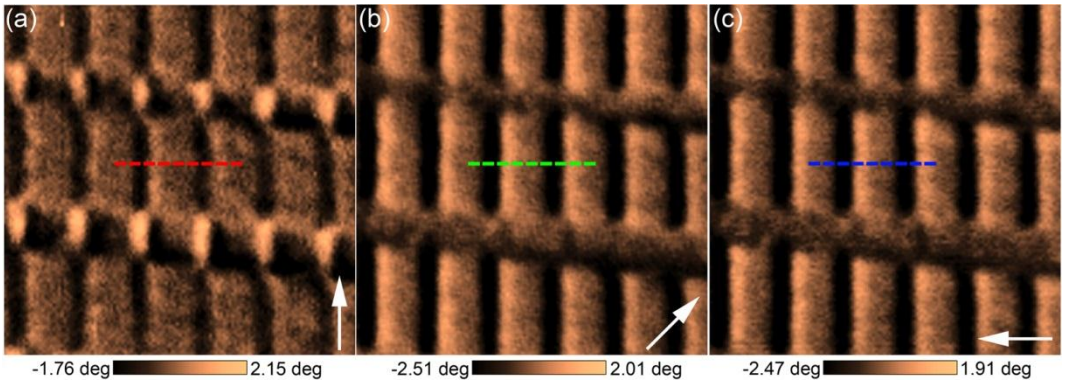

Fig. 3.8 MFM images of the hard disk. (a) Phase shift image obtained with the scanning direction of 0 °. (b) Phase shift image obtained with the scanning direction of 45 °. (c) Phase shift image obtained with the scanning direction of 90 °. The image size is 4.0 μm × 4.0 μm and the resolution is 128×128 pixels. The arrows show the scanning directions.

The profiles extracted from Fig. 3.8 are shown in Fig. 3.9. It can be seen from line I that the value of the smallest phase shift obtained by the scanning direction of 0 ° is -0.73 °, and the values acquired by the scanning directions of 45 ° and 90 ° are -1.86 ° and -2.03 °, respectively. It is known from line II that the highest phase shift value of the profile with the scanning direction parallel to the magnetic structures is 0.70 °. For the 45 ° and 90 ° scanning directions, the highest values are 1.59 ° and 1.47 °, respectively. The peak to peak phase shifts obtained with the scanning direction of 0 ° are the smallest compared with those acquired with the scanning directions of 45 ° and 90 °. It is concluded that there are distortions for the magnetic domains structures paralleled to the scanning direction.

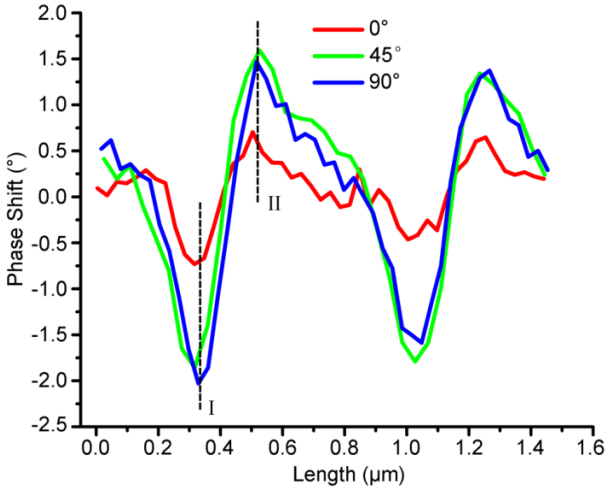

Fig. 3.9 Phase shift signals of hard disk.

Fig. 3.10 shows the MFM images of the standard magnetic sample with three scanning directions of 0 °, 45 °and 90 °. The lift height was 80 nm for MFM imaging in the experiment. The topography image is shown in Fig. 3.10(a). It can be seen from Fig. 3.10(b) that the features of the periodic magnetic domains parallel to the scanning direction are hardly distinguished. The periodic magnetic structures are clearly recognized for the scanning direction unparalleled to the domain, as shown in Fig. 3.10(c) and (d). Fig. 3.10(e) shows the compensated result with the proposed method and it can be seen that the distortions caused by the 0 °scanning are corrected.

The profiles extracted form Fig. 3.10(b-e) are shown in Fig. 3.11(a). The phase shift signals obtained with the scanning direction of 0 °(red line) are ranged from -1.42 °to 0.31 °. The periodic structure is clearly recognized from the phase shift signals obtained with the scanning direction of 45 ° (green line) and the signals are varied between -1.92 °and 2.32 °. For the signals acquired by the scanning direction of 90 ° (blue line), the magnetic domain structures are clear and they are ranged from -1.92 ° to 2.18 °. For the curve extracted from the compensated image (black line), the phase

shift signals varied from -1.74 °to 1.55 °. For the compensated result, the peak to peak value is larger than those of the signals obtained with the scanning direction of 0 °.

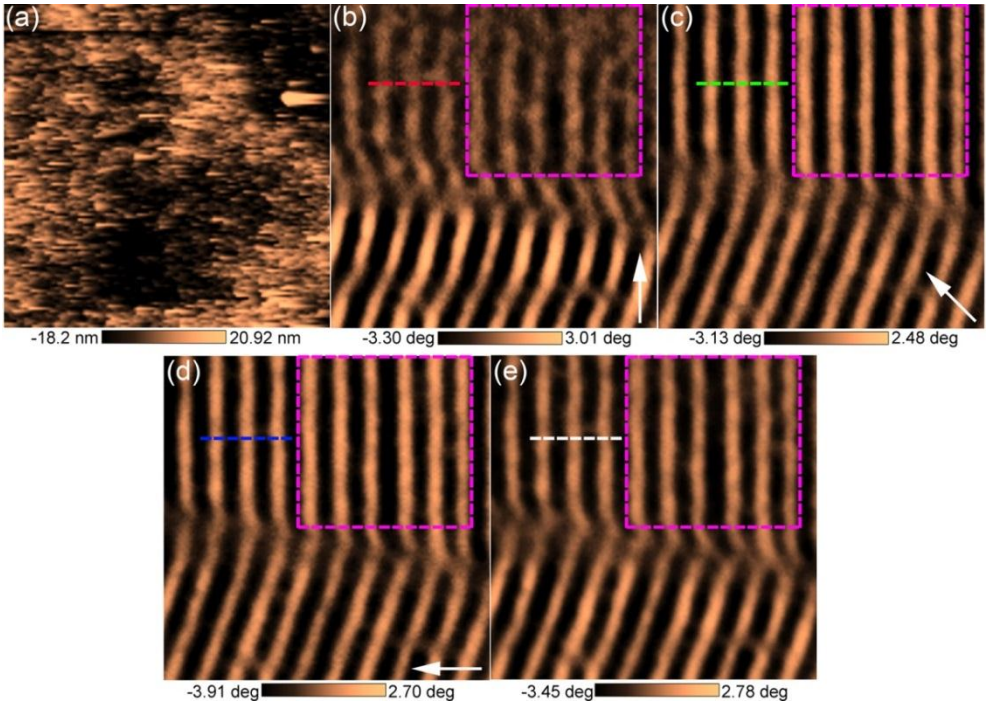

Fig. 3.10 MFM images of the standard magnetic sample obtained with three different scanning directions. (a) Topography image. (b) Phase shift image obtained with the scanning direction of 0 °. (c) Phase shift image obtained with the scanning direction of 45 °. (d) Phase shift image obtained with the scanning direction of 90 °. (e) The compensation result obtained. The image size is 7.5 μm ×7.5 μm and the resolution is 128×128 pixels. The arrows show the scanning directions.

The image contrast distributions of the squared areas in Fig. 3.10(b-e) are shown in Fig. 3.11(b). It can be seen that the contrast in Fig. 3.10(b) is 31.88%. For the areas of Fig. 3.10(c) and (d), the values are 74.45% and 71.73%, respectively. The features of the images with a low contrast are unable to be clearly seen. For the square area in Fig. 3.10(b), the magnetic domain structures are blurred. After the compensation with the

proposed method, the image contrast of the square area in Fig. 3.10(e) is 49.31%.

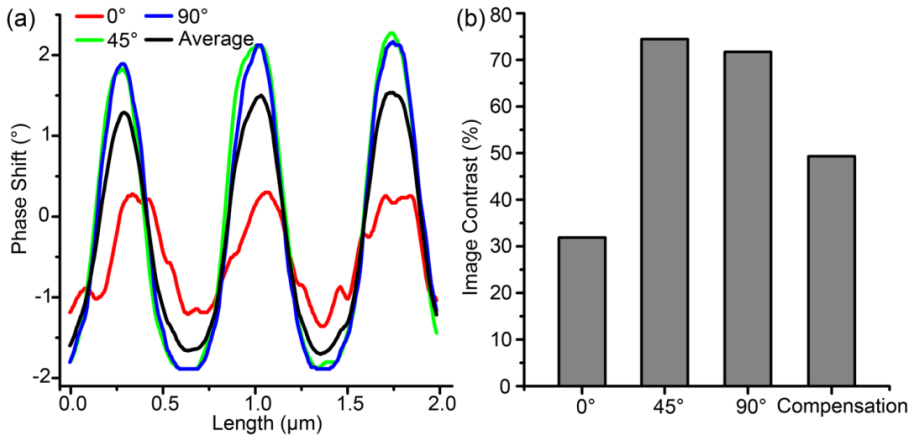

Fig. 3.11 Profiles of the phase shift signals and image contrast. (a) Phase shift signals extracted from the dashed lines in Fig. 3.10(b-e). (b) Image contrasts of the square areas in Fig. 3.10(b-e).

The signals obtained with the scanning directions of 45 ° and 90 ° were used to compensate the signals acquired with the scanning direction of 0 °. Accordingly, the compensation method corrected the distortions and improved the image contrasts of the images obtained with the scanning direction of 0 °.

Fig. 3.12 shows the MFM images of the magnetic sample with the magnetic structures aligned in four directions. The magnetic structures were obtained with the scanning directions of 0 °, 45 ° and 90 °, and the lift height was 45 nm. The compensation result of Fig. 3.12(a-c) is shown in Fig. 3.12(d). The cross-sectional curves of the phase shifts extracted from Fig. 3.12 are shown in Fig. 3.13.

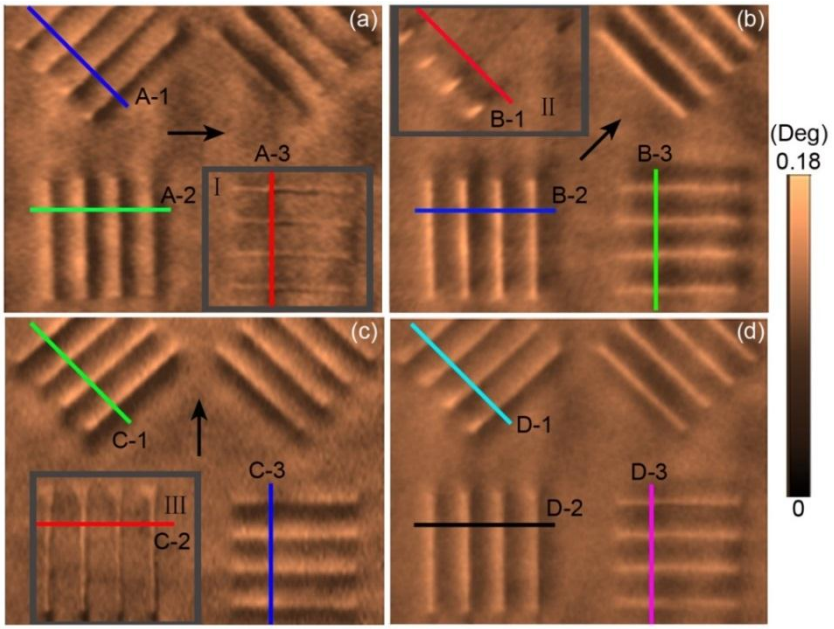

Fig. 3.12 Phase shift images of the magnetic sample with different scanning directions. (a) Obtained with the scanning direction of 0 °. (b) Obtained with the scanning direction of 45 °. (c) Obtained with the scanning direction of 90 °. (d) Compensation result obtained. The image size is 6.4 μm × 5.0 μm and the resolution is 256×200 pixels. The arrows show the scanning directions.

The phase shifts of A-1, B-1, C-1 and D-1 in Fig. 3.12 are shown in Fig. 3.13(a). The phase shift obtained with the scanning direction of 0 ° is ranged from 0.089 ° to 0.115 ° and the compensated phase shift is varied from 0.086 ° to 0.123 °. The phase shifts of A-2, B-2, C-2 and D-2 in Fig. 3.12 are shown in Fig. 3.13(b). The phase shift obtained with the scanning direction of 0 ° is ranged from 0.091 ° to 0.145 ° and the compensated phase shift is varied from 0.088 ° to 0.143 °. The phase shifts of A-3, B-3, C-3 and D-3 in Fig. 3.12 are shown in Fig. 3.13(c). The phase shift obtained with the scanning direction of 0 ° is ranged from 0.08 ° to 0.116 ° and the compensated phase shift is varied from 0.079 ° to 0.127 °. The peak to peak value of the compensated phase shift is larger than that obtained with the scanning direction of 0 °.

It can be seen from Fig. 3.12 that the bottom-right structures in area I, the top-left structures in area II and the bottom-left structures in area III have the largest distortions compared with the structures in other directions. The structures of each direction are clearly imaged after the compensation processed, as shown in Fig. 3.12(d).

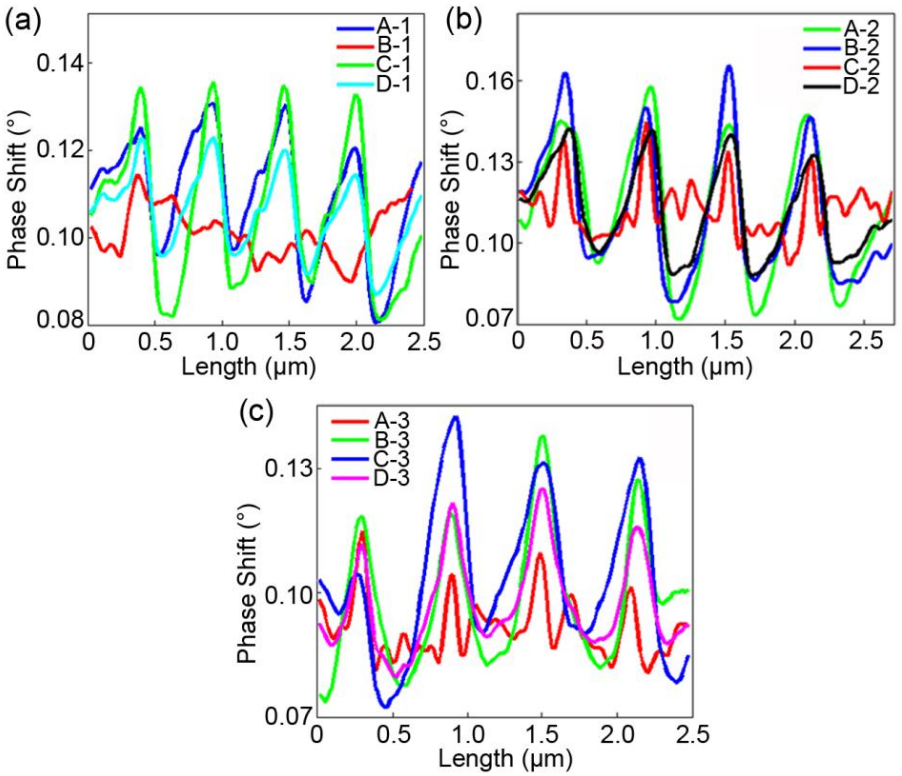

Fig. 3.13 Cross-sectional curves of phase shifts extracted from Fig. 3.12. (a) Extracted from the top-left structures. (b) Extracted from the bottom-left structures. (c) Extracted from the bottom-right structures.

Consequently, it has proved that the scanning direction parallel to the magnetic structure leads to a distortion of the structure, and its phase shift range is declined. It can be concluded that with the MFM imaging compensation method, the distortion structures can be corrected and the effect of scanning directions on the MFM imaging

is significantly reduced.

Nenadović et al. [105] changed the lift heights to obtain the best quality of MFM images. Lisunova et al [169] used a carbon nanotube to sharpen the probe tip for imaging the high resolution magnetic domian. With those methods, the quality of the MFM images was improved. However, the distortions caused by the scanning directions were unsolved. For the sample with complex magnetic domain directions, the magnetic domain structures parallel to the scanning direction were inevitably distorted. It is concluded that with the proposed MFM imaging compensation method, the distortion can be corrected and the effect of scanning directions on the MFM imaging can be significantly reduced.

3.3 Effect of Liquid in MFM Imaging

When the probe vibrating in liquid, the oscillation of the cantilever is significantly affected by the interaction forces, known as hydration forces, between the water molecular and the probe surface, which has a strong influence on the determination of the parameters of a tapping magnetic probe. To investigate the performance of magnetic probe with different the resonant frequency, Q-factor and spring constant in air and liquid environments, MFM images of a hard disk acquired in ambient and liquid conditions are compared. The results are important for the use of MFM in biological applications.

3.3.1 Principles

It is possible for MFM to measure forces with different detecting techniques [34] and there are interaction forces between the tip magnetic dipole moment and the sample. Because of its high sensitivity and stability, the common method used for detecting the force gradient is to calculate the phase shift of an oscillation cantilever [30].

The forces detected by MFM are purely magnetic static forces and they depend on the interactions of the magnetic tip and the sample [39]. For the phase shift $\Delta\varphi$ MFM imaging method, the phase signal of every point of the scanned area is recorded. The phase shift is proportional to the derivative of the magnetic force between the tip and the sample in the Z direction, and it can be expressed as Eq. (2.1) [35, 36].

In liquid environments, the forces interacted on the probe are quite complex. However, compared to the ambient environment, the van der Waals forces are reduced significantly, and the capillary forces are eliminated and electrostatic forces are minimized [170-172]. For the working magnetic probe, the magnetic force F_M, drive force F_D, hydrate force F_H and noise force F_N are coexisted, as shown Fig. 3.14.

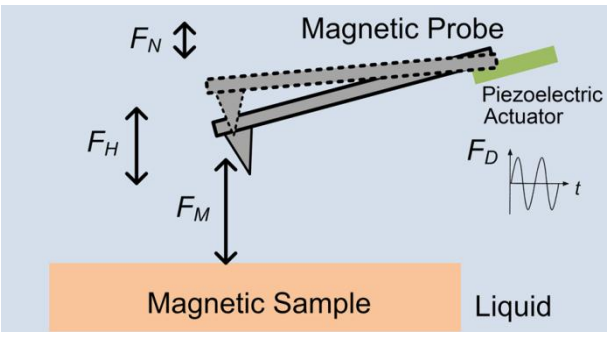

Fig. 3.14 Forces of magnetic probe on magnetic sample in liquid.

The probe is fixed at one end on the probe holder, and the piezoelectric actuator is fixed on the probe holder and adjacent to the probe. A voltage signal is applied to the actuator to drive the cantilever oscillation. A uniform beam is used to measure the deflection of the probe cantilever. When the probe vibrating in the liquid, the oscillation of the cantilever is significantly damped due to the interaction forces between the water molecules and the probe surface, which is known as the hydration force [173]. In an AFM system, the laser is detected by PSD. The displacement sensor noise and thermal displacement are the two major noises consisting of the frequency noise [174]. Thus, the magnetic forces between the sample and the probe are significantly affected in the liquid.

3.3.2 Experiments and Discussions

Mica with the size of 15 mm×15 mm×1 mm was used as the nonmagnetic sample and a hard disk cut into 10 mm×10 mm were used as the magnetic sample. All the measurements were implemented by JPK (NanoWizard®3, Germany) MFM system. The magnetic probe (Magnetic Multi 75-G, Budgetsensors) was used for the imaging and measurement of the samples in air and liquid environments. The typical resonance frequency of the probe was 75 kHz, the spring constant was 3 N/m, the cantilever length was 225 μm and the tip height was 17 μm. The liquid used in the experiments was ultrapure water and the ambient environment was a standard clean room.

The adhesive force and parameters of the magnetic probe including the resonance frequency, quality factor (Q-factor) and spring constant were obtained on the substrates of mica and hard disk in ambient and water environments, and they were detected with a height of 30 μm from the hard disk and mica surface. Each group of

the parameters were collected with at least 10 measurements, and the results were calculated as Mean ±SD values.

To improve the quality of the MFM images obtained in the liquid environment, the parameters of the magnetic probe in air and liquid environments are analyzed. The MFM images of a hard disk obtained in both ambient and liquid environments are compared.

The resonance frequency of the magnetic probe in ambient and water environments is shown in Fig. 3.15. The resonance frequency of the probe working in the ambient environment is 74.21 kHz and its amplitude is 1.52 V with the drive amplitude of 0.17 V, as shown in Fig. 3.15(a). With the same drive amplitude, the resonance frequency of the probe tapping in the water is 28.61 kHz and its amplitude is 0.08 V, as shown in Fig. 3.15(b). It is known that the amplitude is too low to scan the magnetic samples and acquire their magnetic features. The drive amplitude is increased to 1.90 V to improve the amplitude of the probe oscillating in the water, as shown in Fig. 3.15(c). Then the amplitude is raised to 1.50 V with the resonance frequency of 27.2 kHz. It can be seen that the resonance frequency and its amplitude are affected significantly by the liquid. The amplitude can be improved by the increase of the drive amplitude.

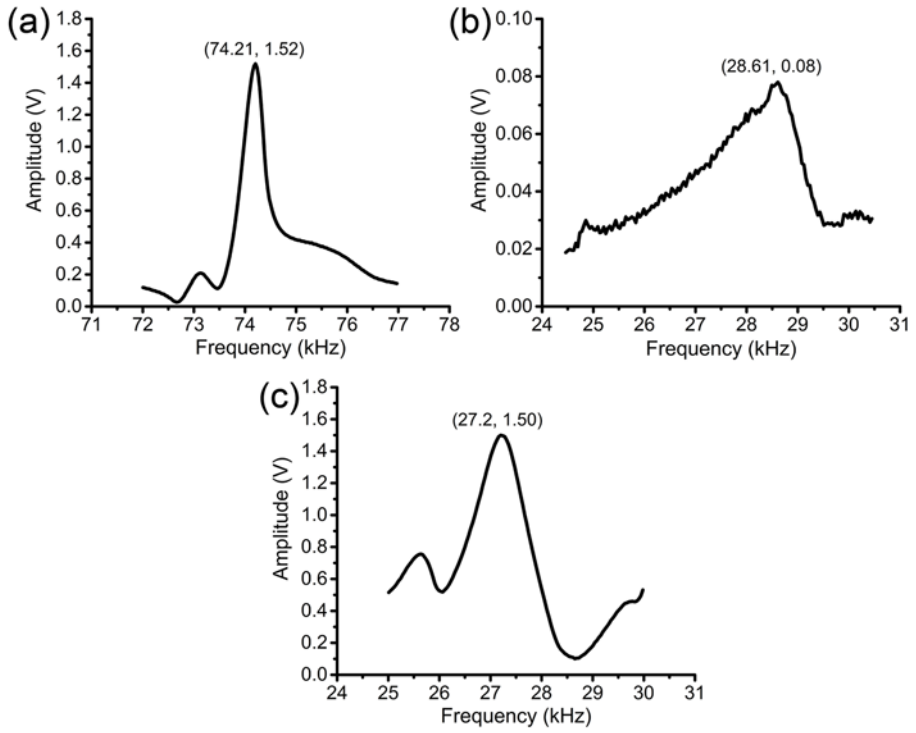

Fig. 3.15 Resonance frequency of the magnetic probe obtained in the ambient and water environments. (a) is obtained with a drive amplitude of 0.17 V in the ambient environment. (b) is obtained with a drive amplitude of 0.17 V in the water and (c) is obtained with a drive amplitude of 1.90 V in the water.

The resonant frequency of the magnetic probe in ambient and water environments is collected on the mica and hard disk substrate surfaces, as shown in Fig. 3.16. The resonant frequency values on the mica surface and hard disk surface are similar in the ambient environment, and the values are 72.02±0.01 kHz and 72.14±0.01 kHz, respectively. In the water, the resonant frequencies are 28.76±0.39 kHz and 28.72±0.18 kHz, respectively. It can be concluded that there are insignificant effects of substrate on the resonant frequency due to the hydration force of the water, and the resonant frequency are reduced significantly in the water.

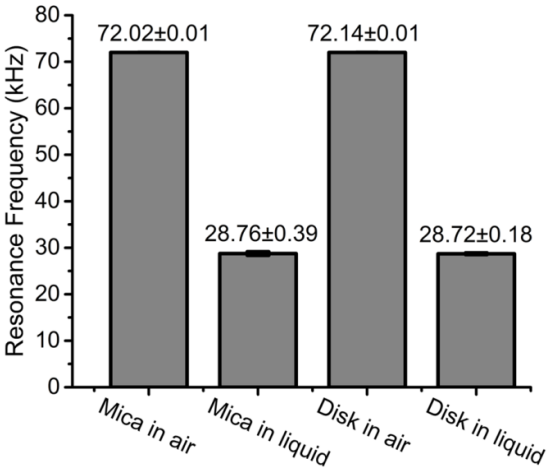

Fig. 3.16 Resonance frequency of the magnetic probe obtained in ambient and water environments.

The Q-factor of the magnetic probe in ambient and water environments are shown in Fig. 3.17(a). In the ambient environment, for the mica sample the Q-factor is 192.48±22.97 and for the disk sample the Q-factor is 165.07±12.24. In the water, the Q-factor on the mica surface is 3.66±0.13 and on the hard disk surface is 3.68±0.16. It can be seen that the substrates have little effect on the Q-factor in the ambient environment but unaffected on it in the water environment. Because of the resistance of the water, the oscillation of the probe is significantly damped and the quality factor Q is reduced dramatically. Thus, the Q-factor in the air is larger than that in the liquid environment.

The spring constants of the magnetic probe obtained in various environments are shown in Fig. 3.17(b). In the ambient environment, the spring constant is 3.40±0.22 N/m for the mica substrate and it is 3.11±0.25 N/m for the hard disk substrate. It can be seen that the magnetic field has little effect on the spring constant of the magnetic probe in the air. In the water, the spring constant on the mica surface is the same as that on the hard disk, and the substrate has no effect on the spring constant.

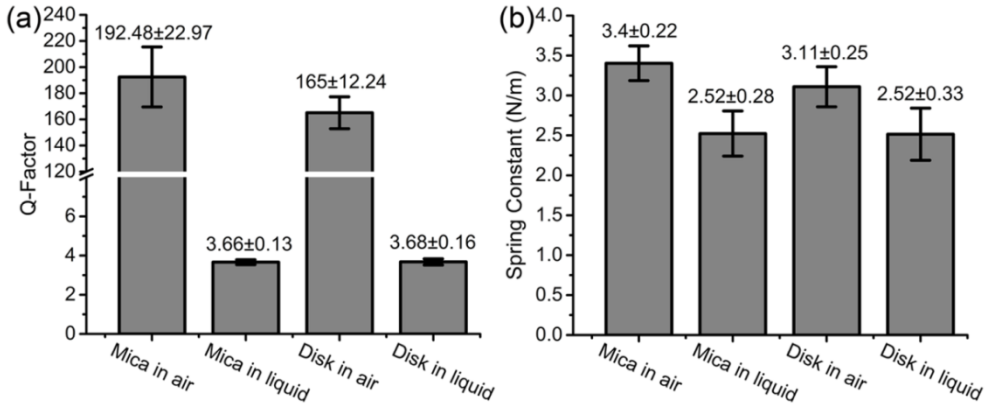

Fig. 3.17 Q-factor and spring constant of the magnetic probe obtained in the ambient and water environments.

From Fig. 3.17 it can be seen that the reduction of the Q from the air to water is larger than the decrease of *k* from the air to water. Thus, $(Q/k)_{air}>(Q/k)_{water}$. For the same *F'*, $\Delta\varphi_{air}>\Delta\varphi_{water}$, and the quality of MFM images is affected by liquid.

In Fig. 3.18, force-displacement curves of the four groups are compared. It can be seen that the maximum adhesive forces (the lowest position of the curve) of the probe retracted from the disk and mica surfaces are significantly different in the ambient environment. It is because that there is a magnetic force (attractive/repulsive force) between the probe and the disk. However, due to the resistance of the liquid there are little differences between the disk and mica in the water environment. The retraction speed is 2.0 μm/s.

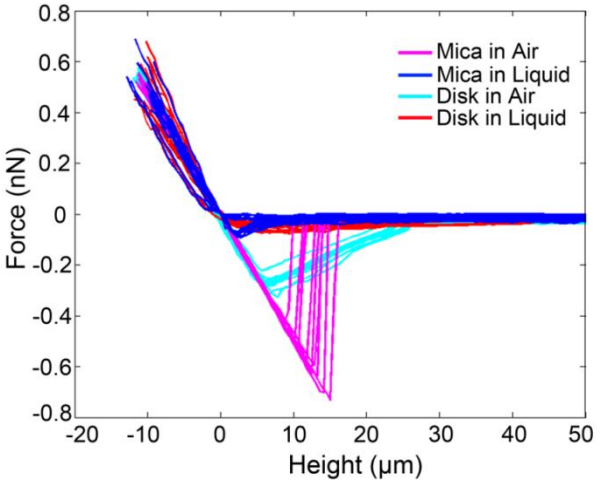

Fig. 3.18 Force-displacement curves of the magnetic probe in water and ambient environments.

The phase shift signals are used for the imaging of hard disk obtained in air and water environments, as shown in Fig. 3.19. Fig. 3.19(a) is obtained with the lift height of 50 nm and with the scan rate of 1.00 Hz, and the drive amplitude is 2.537 V in the air. It can be seen that the magnetic domain structures are clearly recognized in the air. Fig. 3.19 (b) is acquired with the lift height of 20 nm and the scan rate of 0.5 kHz, and the drive amplitude of 3.387 V in the water. The magnetic domain structures cannot be found. Fig. 3.19 (c) is observed with the lift height of 20 nm and with the scan rate of 0.5 kHz, and the drive amplitude is increased to 4.511 V in the water. It can be seen that the magnetic domains can be observed with the increase of the drive amplitude in the liquid environment.

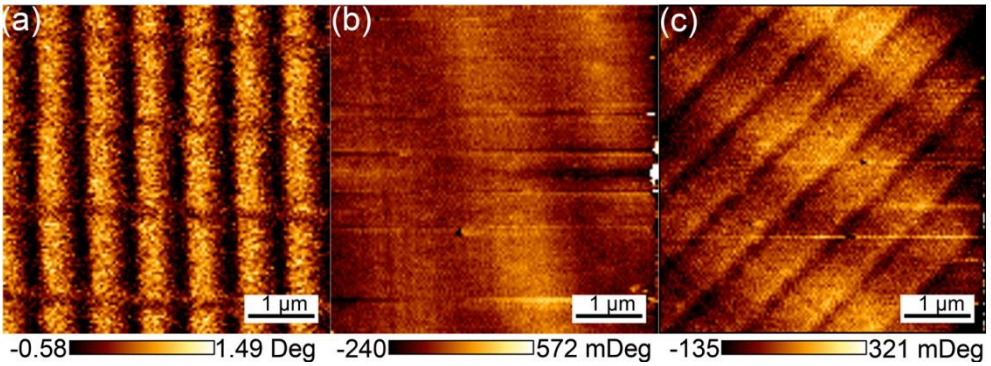

Fig. 3.19 MFM images of a hard disk obtained in the air and water. (a) MFM image of the hard disk obtained in the air with the drive amplitude of 2.537 V. (b) MFM image of the hard disk obtained in the water with the drive amplitude of 3.387 V. (c) MFM image of the hard disk obtained in the water with the drive amplitude of 4.511 V. The image size is 128×128 pixels.

The lift height significantly influences the MFM imaging in the liquid, as shown in Fig. 3.20. In the experiments, the scan rate is 0.60 Hz and the drive amplitude is 4.782 V. Fig. 3.20(a) is the topography image of the hard disk. Fig. 3.20(b) is obtained with the lift height of 10 nm. The topography significantly affects the MFM imaging, and the topography characters are clearly as shown in the figure with arrow. Fig. 3.20(c) is acquired by the increase of the lift height to 20 nm and the effect of the topography is reduced with the magnetic features enhanced. Fig. 3.20(d) is obtained with the lift height of 50 nm and there is little effect on the topography but the magnetic features are weakened. It can be concluded that the lift heights affect the topography and significantly influence the quality of MFM images.

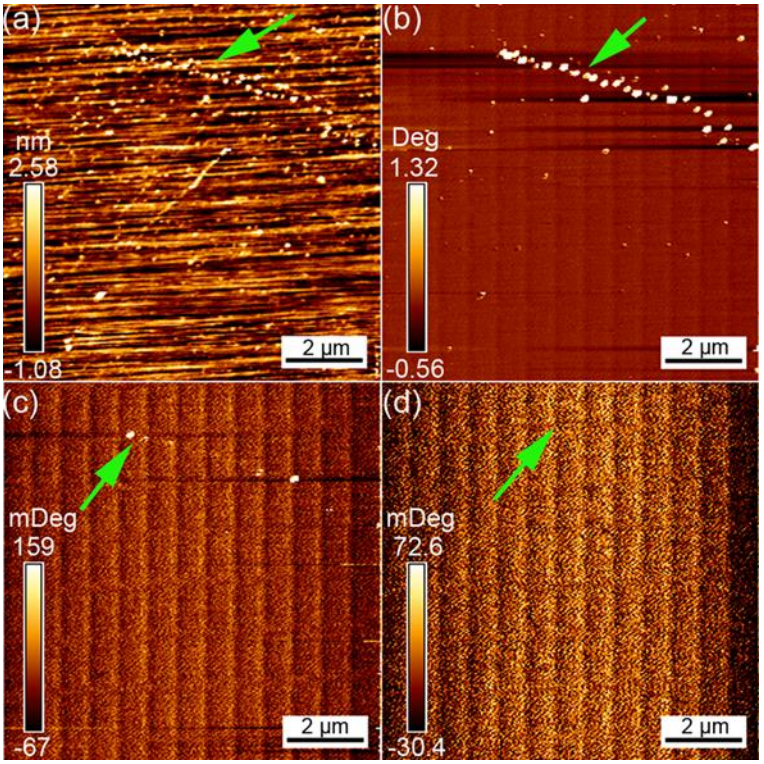

Fig. 3.20 MFM images of the hard disk acquired with different lift heights in the water. (a) Topography of the hard disk. (b) MFM image with the lift height of 10 nm. (c) MFM image with the lift height of 20 nm. (d) MFM image with the lift height of 50 nm. The arrows show the topography characters. The image size is 256×256 pixels.

3.4 Summary

This chapter focuses on the quality improvement of MFM imaging. First, differential MFM imaging has been explored using the proposed two-pass scanning procedure which is able to extract differential magnetic forces and to eliminate or even significantly reduce background forces with the reversed tip magnetization. The theoretical and experimental results have shown that the image contrast and SNR can be significantly improved in the MFM imaging.

Secondly, the effect of scanning directions on the magnetic imaging was investigated and a compensation method was proposed. It can be concluded from the experimental results that the probe scanning direction parallel to the magnetic domain structure can cause a distortion of the scanned structure with a minimum phase shift difference. The compensation method was developed to improve the accuracy of magnetic domain structures. With the proposed compensation method, the distortion structures were corrected and the effect of scanning directions on the MFM imaging was significantly reduced. This work provides a way for the acquisition of the correct images of magnetic structures using an MFM and the improvement of imaging quality in a wide range of MFM applications.

Finally, the effect of liquid on the parameters of the magnetic probe was investigated. It is found that the resonant frequency, amplitude, Q-factor, spring constant and the adhesive force were reduced significantly in the liquid, and the MFM images were often with unclear magnetic features. To improve the quality of the magnetic images, the drive amplitude and the lift height should be adjusted. The results have shown that the magnetic features can be recognized with the increase of the drive amplitude and the appropriate lift height.

CHAPTER 4

SYNTHESIS OF MNPS AND MANIPULATION OF MNPS BY MAGNETIC PROBE

Due to their unique features such as the high reactivity, larger surface area and biocompatibility [175], magnetic nanoparticles (MNPs) are widely used for targeting specific diseases, drug delivering, MRI [176], electronic device measurement [177] and sewage disposal management [178]. In biomedicine applications, various methods have been studied to synthesise MNPs that can be used to treat cells [53, 54]. To implant the MNPs into cancer cells for them to be treated, the methods for picking up MNPs and releasing them down using MFM have been investigated.

Most existing MNPs synthesis methods have limitations in operating normal laboratory settings as they require high temperature and high pressure. The cost to meet such required conditions is high. Chemical co-precipitation method is a relatively simple method under a common laboratory condition and it was used to obtain Fe_3O_4 MNPs [111]. In this research, this method is adopted to synthesise Fe_3O_4 MNPs with the moderation on stoichiometric ratio of Fe^{2+}/Fe^{3+} to obtain efficient chemical reactions.

A group of methods for pushing or sliding a target object along a planned straight line path is commonly used in manipulation of nanoparticles [118]. As the target object is manipulated laterally, it is hard for MFM probe pick up the particles with those

methods. The flexibility of the manipulations in many applications is also limited due to the planned path being a straight line. In this research, a helical curve is designed as the capture path for MFM probe to follow, enabling a flexible picking up of MNPs.

Many methods have been used to release the adhered objects from magnetic probe [179, 180]. However, these methods could cause damage to the probes. They are also not suitable for releasing MNPs from the magnetic probe. In this research, a method of using a biaxiably-oriented polypropylene (BOPP) film together with an external magnetic field is developed for releasing MNPs from MFM probe tips.

4.1 Synthesis of Fe_3O_4

The chemical co-precipitation method together with the dispersant of polyethylene glycol 2000 (PEG-2000) were used to synthesise MNPs with well dispersed Fe_3O_4. It was found that poor MNPs were obtained with the stoichiometric ratio of Fe^{2+}/Fe^{3+} 1:2 and the ratio was changed to 2:3 for improving the yield of the reactants. The X-ray diffractometer (XRD), scanning electron microscope (SEM) and MFM were used to characterize the MNPs. SEM images were acquired with and without the use of PEG-2000 to compare the effect of the polymer on the dispersion of MNPs.

4.1.1 Materials and Methods

Chemical co-precipitation for Fe_3O_4 formation can be expressed as [111]

$$Fe^{2+} + 2Fe^{3+} + 8OH^{-} \rightarrow Fe_3O_4 + 4OH \qquad (4.1)$$

To synthesise Fe_3O_4 MNPs, several chemicals and instruments were used, as shown in Table 4.1.

Table 4.1 Chemicals and instruments used in Fe_3O_4 MNPs synthesis.

	Chemical	Instrument
1	$FeCl_2 \cdot 4H_2O$	Beaker
2	$FeCl_3 \cdot 6H_2O$	Conical Flask
3	HCl	Magnetic Stirrer (HJ-3)
4	$NH_3 \cdot H_2O$	High-speed Centrifugation (5430R, Eppendorf)
5	PEG-2000	Diffractometer (TongDa TD-3000)
6	N_2	SEM (FEI QUANT-250 FEG)
7	C_2H_6O	MFM (CSPM-5500, BENYUAN)

$NH_3 \cdot H_2O$ (0.5 mol/L) was used as the precipitant and PEG-2000 was used for dispersing the particles. High purity N_2 was used to protect the process in the experiment. Magnetic stirrer (HJ-3) was used for the synthesis and the high-speed centrifugation (5430R, Eppendorf) was used to separate the MNPs.

Properties of Fe_3O_4 MNPs synthesised by chemical co-precipitation together with PEG-2000 were analysed by a diffractometer using Cu-Kα (λ=0.154 nm). The sizes and structures of the particles were examined by SEM at the 5 kV accelerated voltage, from which the samples were prepared by dispersing the particles in absolute ethyl alcohol and then depositing the MNPs on a clean silicon wafer surface and subsequently dried in the air at room temperature. MFM system was used to analyze

the nanoscale magnetic properties of the Fe_3O_4 MNPs at a lift height of 15 nm. The employed magnetic probe was the BudgetSensors' Multi75M-G, and the resonant frequency was 75 kHz. The MFM images of Fe_3O_4 MNPs were acquired under the conditions of the clean room environment with controlled room temperature, and the tapping-lift mode was used for imaging.

No further purification was applied to chemicals used in the experiment. The Fe_3O_4 MNPs were fabricated by chemical co-precipitation in liquid and several steps were performed:

1) 0.0795 g $FeCl_2 \cdot 4H_2O$ was diluted with ultrapure water to 50 mL.

2) A few drops of concentrated hydrochloric acid were added into 0.1621 g $FeCl_3 \cdot 6H_2O$ to prevent the hydrolysis of Fe^{3+}, and then ultrapure water was added to 50 mL.

3) The two solutions were mixed together in a conical flask after the dissociation of them with ultrasonic oscillation completely.

4) 1 g PEG-2000 was then added as dispersant and mixed with the solution again by ultrasonic oscillation.

5) The solution was continuously stirred for 10 minutes, and then $NH_3 \cdot H_2O$ was gradually added into the solution as precipitant until the colour of the mixture was changed from yellow to black.

6) 45 minutes later, the synthesis was completed.

The constant temperature magnetic stirrer was set to work at the temperature of 70 ℃ ensure the required synthesis temperature. The whole synthesis process was protected with N_2. After the reaction, the solution was naturally cooled down to the room temperature, and the MNPs were separated using a power permanent magnet. Large particles and unreacted materials were then removed with the centrifugation (1000 rpm/min, 5 min), and the MNPs were washed with absolute ethyl alcohol (C_2H_6O) until the washing liquid became neutral. The resultant MNPs were dispersed in absolute ethyl alcohol.

4.1.2 Results and Discussions

It was found in the experiments that the Fe_3O_4 synthesis results with the stoichiometric ratio of Fe^{2+}/Fe^{3+} of 1:2 is poor, as given in Fig. 4.1 (a-c). After 12 hours standing, the solution is still in muddy, shown in Fig. 4.1(a). Although with the applied magnetic fields, the particles were concentrated to the magnet, depicted in Fig. 4.1(b), which indicates that the obtained particles were with magnetic characters, the particles size of the obtained nanoparticles were unregularly and they were aggregative together as shown in Fig. 4.1(c).

Fe_3O_4 MNPs synthesised with the stoichiometric ratio of Fe^{2+}/Fe^{3+} of 2:3 and its XRD pattern are shown in Fig. 4.1(d-f). Fig. 4.1(d) is the resultant solution after standing for 1h and it has clearly been separated. Fig. 4.1(e) is the resultant solution in a magnetic field. It can be observed that when the reaction solution is placed adjacent to a permanent magnet, it becomes limpid in a few seconds. This indicates that the obtained MNPs have good magnetism. Fig. 4.1(f) shows the XRD pattern of Fe_3O_4 MNPs synthesized by the chemical co-precipitation method and it clearly shows the

XRD signals. It is worth to point out that, when comparing with the obtained results, all the diffraction peaks were assigned to the pure Fe_3O_4 structure and the broadening of reflection peaks is obvious, which includes the formation of ultrafine particles.

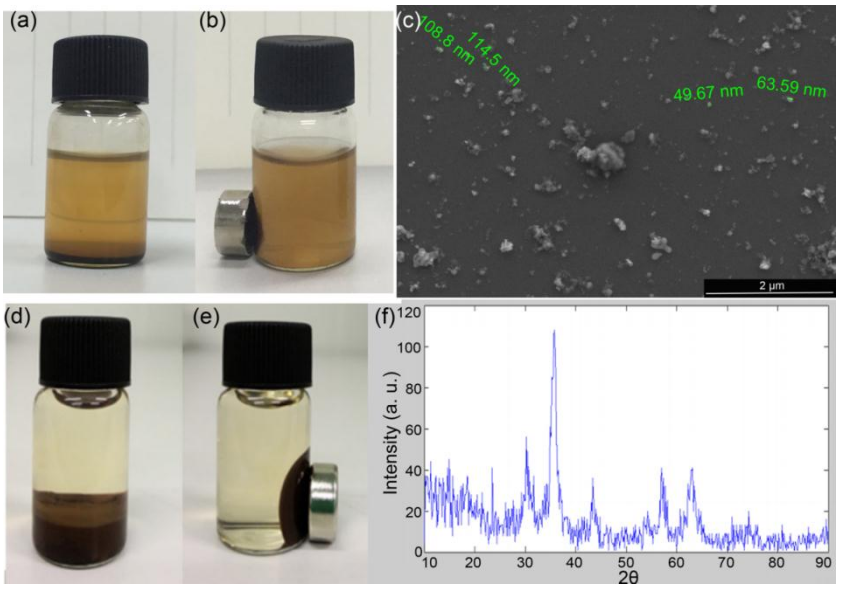

Fig. 4.1 Fe_3O_4 MNPs after reaction. (a) is the solution after standing for 12 hours and (b) is the solution in a magnetic field, and (c) is the SEM results of the obtained nanoparticles (Fe^{2+}/Fe^{3+} is 1:2). (d) is the solution after standing for 1 hour and (e) the solution in a magnetic field, and (f) is the XRD pattern of Fe_3O_4 MNPs (Fe^{2+}/Fe^{3+} is 2:3).

It can be conclude from Fig. 4.1 that the precipitation reactions of the Fe^{2+} and Fe^{3+} solutions using aqueous ammonia usually produce a mixture of magnetite and maghemite. Compared with the Fe^{2+}/Fe^{3+} ratio of 1:2, the ratio of 2:3 produces much better results in the sense of efficiency, regular MNP size and separate individual MNPs. Although the differentiation between them is not possible from the X-ray data in Fig. 4.1(f), magnetite presence is evident due to the black colour of the result products.

To analyse the dispersion and nanostructure of the obtained Fe_3O_4 MNPs with the use of PEG-2000, SEM was applied to detect their size and dispersion, as shown in Fig. 4.2. It can be seen that the Fe_3O_4 MNPs are of quasi-spherical shaped and are well dispersed. The average diameter of the particles is 100 nm. Some large Fe_3O_4 MNPs are also observed and this suggests that part of Fe_3O_4 MNPs could be agglomerated during the reaction process.

For comparison, the SEM image of the agglomerated Fe_3O_4 MNPs synthesized without the use of PEG-2000 is shown in Fig. 4.3. All reactions have rendered the black colour of the particles and there is no visually difference between the particles fabricated with and without the use of dispersants. According to the formation principle of Fe_3O_4 MNPs, PEG-2000 is significant in the process. It is clear that the Fe_3O_4 particles obtained without the use of PEG-2000 aggregate with each other and the polymer affects the crystallinity of the precipitation reaction products.

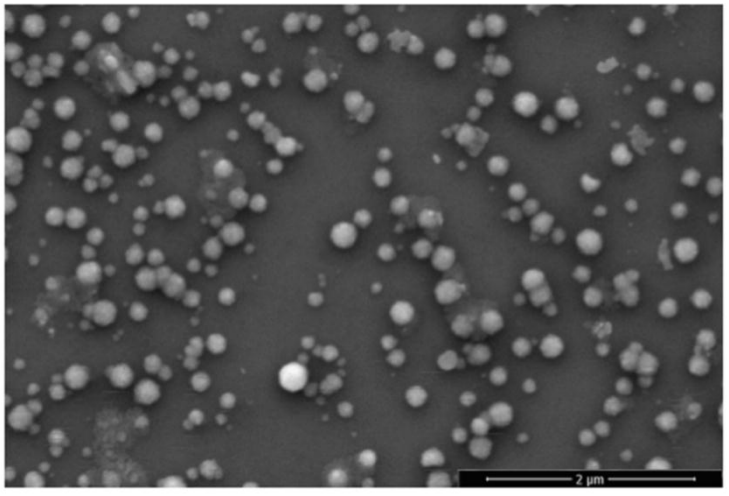

Fig. 4.2 SEM image of Fe_3O_4 MNPs obtained with PEG-2000.

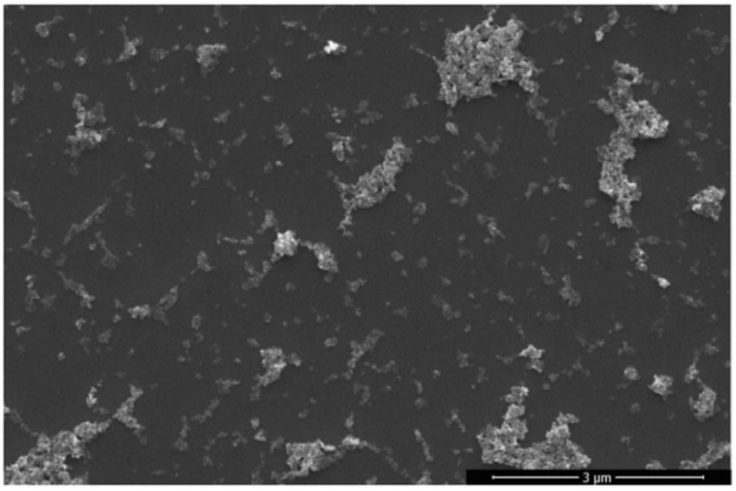

Fig. 4.3 SEM image of Fe_3O_4 MNPs without the use of PEG-2000.

To estimate the actual magnetic information of Fe_3O_4 MNPs, their magnetic characteristics were analyzed by MFM, as shown in Fig. 4.4. It shows the MFM images of Fe_3O_4 MNPs and they present the paramagnetic behaviours of the Fe_3O_4 particles. In the MFM images, magnetic signals from the MNPs are obvious. Although the magnetic anisotropy barrier is low and the magnetization of particles can be changed easily by the external magnetic fields, the particles have their stable magnetic domains. Fig. 4.5 shows the cross-sectional curves extracted from Fig. 4.4(a). It can be seen that the diameter of the MNPs was about 100 nm.

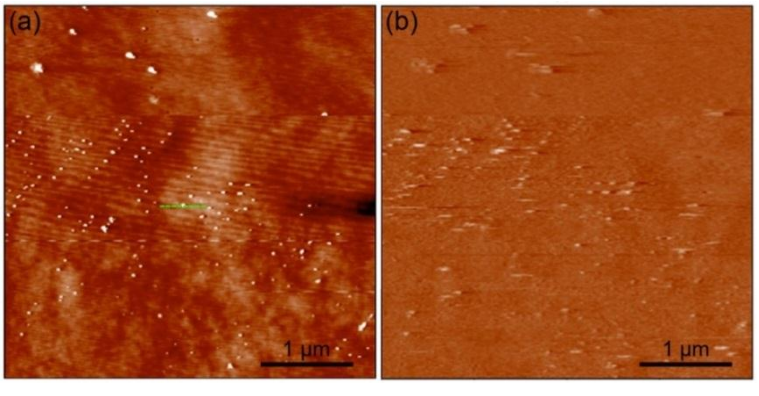

Fig. 4.4 MFM images of Fe_3O_4 MNPs. (a) is the topography image and (b) is its corresponding magnetic force image.

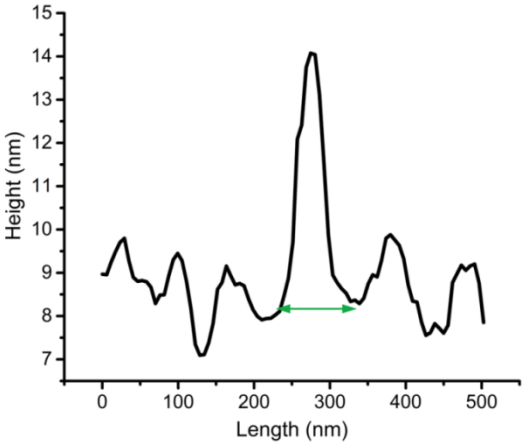

Fig. 4.5 Cross-sectional curves extracted from Fig. 4.4(a).

4.2 Helical Curve Path for MNPs Lifting up

4.2.1 Theory

The diameter of particle size being less than 100 nm, leads to the particle superparamagnetic or paramagnetic character [181]. The significant feature of superparamagnetic particles is that they will only be magnetized by an applied magnetic field, consequently presenting a single magnetic domain with a moment of the magnetic direction being impacted by the applied magnetic field [182, 183]. The MNPs magnetized by a magnetic probe are shown in Fig. 4.6. Additionally, the single magnetic domain direction of MNPs is presented.

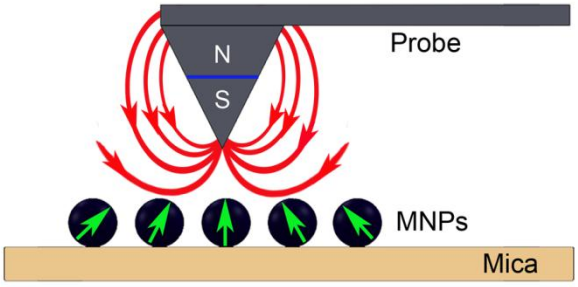

Fig. 4.6 Magnetic domain directions of MNPs magnetized by magnetic probe.

A helical curve was designed as the capture path and it was followed by the magnetic tip for manipulating the MNPs, as shown in Fig. 4.7(a). The lift-tapping mode was first used for scanning the distributions of MNPs on the mica surface and a nanoparticle was selected as the target to be picked up. It was then switched to the manipulation mode drawn a helical curve, and moved the tip along the designed helical path with a specified speed and pushing force to approach the target nanoparticle, as presented in Fig. 4.7(b). The force for the scanning was smaller than that for operating the nanoparticle. Finally, the tip was retracted from the mica surface and the nanoparticle was picked up, as shown in Fig. 4.7(c).

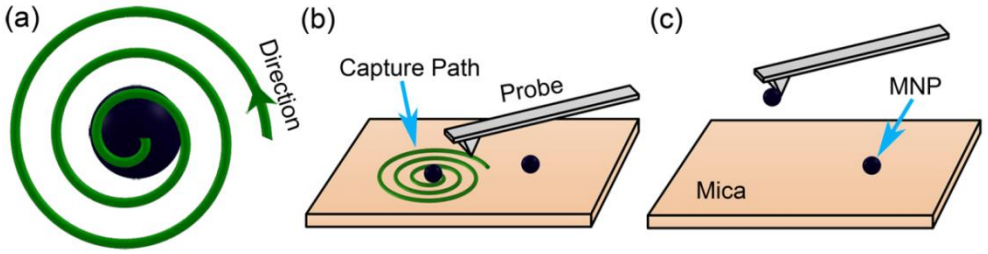

Fig. 4.7 Mechanical manipulation of MNPs. (a) A helical curve was designed as the capture path. (b) The probe followed the capture path to approach the target MNP. (c) The target MNP was picked up by magnetic tip and removed from the mica surface.

The interaction forces between the magnetic probe and the MNP in the approaching process are presented in Fig. 4.8. Fig. 4.8(a) shows the forces acting on the MNP during the process of tip approaching to the target nanoparticle on the mica surface in the x/y plane. F_m is the magnetic force to attract the nanoparticle attached to the tip surface. F_r is the resistance force against the particle to move, whereas it constitutes with the van der Waals', capillary, electrostatic and friction forces between the particle and the substrate surface. In the approaching process, there should be a maximum value for F_r. When F_m is not large enough, the nanoparticle does not move on the surface, namely at the equilibrium state, thus F_m=F_r. Apparently, the magnetic force direction always changes when the tip move along the capture path and the value of F_m increases with the decrease of the distance between the probe and the particle. The F_m acting onto the particle is presented in Fig. 4.8(b).

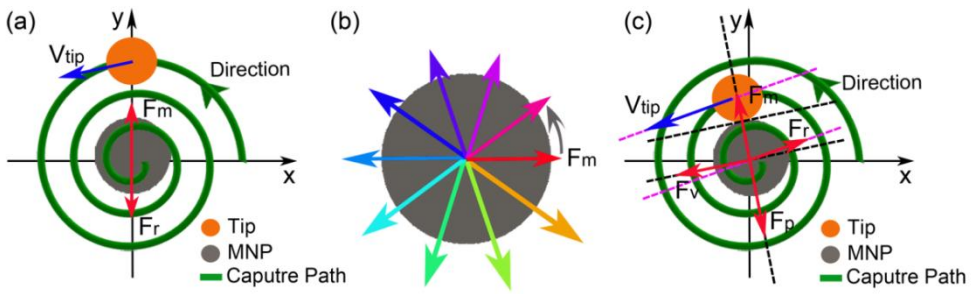

Fig. 4.8 Forces acting on the MNP on the substrate surface in the process of tip approaching. (a) Forces acting on the particle when the magnetic tip approaching to the particle. (b) Magnetic force alteration when the magnetic tip approaching to the particle. (c) Forces acting on the MNP when the magnetic tip contacts the particle.

As shown in Fig. 4.8(c), the magnetic force F_m will reach its maximum value with the direction towards the tip when the magnetic tip contacts the target particle. The tangential force F_v is parallel to the tangential direction of the tip and the particle

contact surface. The push force F_p is opposite to the direction of F_m, and F_p is proven to be controllable and set by the MFM system. F_r is opposite to the tangential direction of the moving path against the particle moving on the surface. The directions of F_m, F_v, F_p and F_r are always changed during the movements of the tip following the designed helical path. Due to the existence of F_v and F_p, when the tip moves along the capture path and pushes the particle, the particle will be slid on the substrate and then F_r will be decreased to the minimum [118, 184, 185].

The tip will retract from the mica surface when the MNP is attached on the tip surface, as shown in Fig. 4.7(c). The force model of the magnetic tip picking up the MNP vertically is presented in Fig. 4.9 [40, 116, 117].

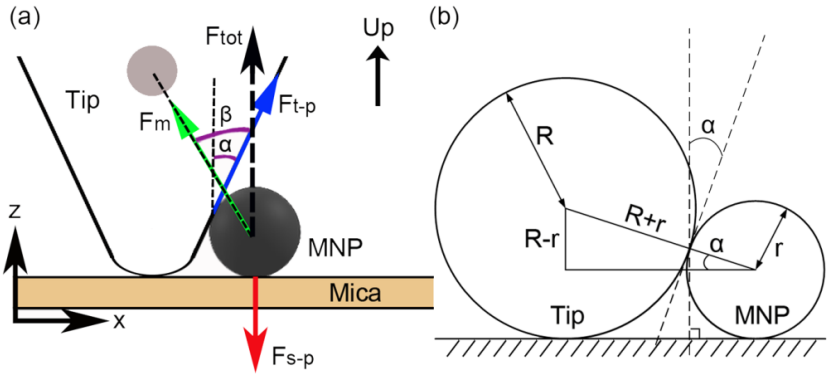

Fig. 4.9 Force model of magnetic tip picking up the MNP vertically. (a) Forces during the pick-up of the particle by the tip. (b) Angle between the tip and the particle.

In Fig. 4.9(a), the forces are expressed as [186]

$$F_{t-p} = F_{tv} + F_{tc} + F_{te} + f_{t-p} \tag{4.2}$$

$$F_{s-p} = F_{sv} + F_{sc} + F_{se} + F_g + f_{s-p} \tag{4.3}$$

where, $F_{t\text{-}p}$ and $F_{s\text{-}p}$ are the tip-particle and surface-particle forces, respectively,

including the van der Waals' force F_{tv} and F_{sv} [187], capillary force F_{tc} and F_{sc} [188, 189], electrostatic force F_{te} and F_{se} [46]. $f_{t\text{-}p}$ is the friction force between the tip surface and the particle, $f_{s\text{-}p}$ is the adhesive force between the substrate surface and the particle [117, 190], and F_g is the gravity of the particle.

F_m is the magnetic force between the probe and the particle [41], it is expressed as Eq. (2.5). F_{tot} is the total interaction force of $F_{t\text{-}p}$ and F_m in the vertical direction. It can be expressed as

$$F_{\text{tot}} = F_{t-p}\cos\alpha + F_m\cos\beta \tag{4.4}$$

Because the tip radius R is smaller than 60 nm and the radius of nanoparticle r is smaller than 50 nm, the value of $cos\alpha$ is close to 1. The tip height is 17 μm and significantly larger than the particle size. The angle β is very small and it can be assumed to be 0. Thus, Eq. (4.4) can be calculated by

$$F_{\text{tot}} \approx F_{t-p} + F_m \tag{4.5}$$

The vertical direction force of the particle is:

$$F_p\Big|_z = F_{tot} - F_{s-p} \tag{4.6}$$

Since the van der Waals', capillary, electrostatic forces and friction exist simultaneously at the tip and the mica surface, it can be assumed that $F_{tv}=F_{sv}$, $F_{tc}=F_{sc}$, $F_{te}=F_{se}$ and $f_{t\text{-}p}=f_{s\text{-}p}$. Combining Eqs. (4.2), (4.3) and (4.5), Eq. (4.6) can be rewritten as

$$F_p\Big|_z \approx F_m - F_g \tag{4.7}$$

Due to the small particle gravity of the particles used ranging from 10 nm to 100 nm in diameter [191], and the superparamagnetic character of nanoparticles, F_m will be large enough if the particle is attached on the tip surface and the following relation is observed: $F_m >> F_g$. Thus, the particle can be separated from the mica surface and picked up by the magnetic tip.

4.2.2 Experiment Setting

The co-precipitation method was used to synthesize Fe_3O_4 MNPs [192]. Then the MNPs were functioned by acetate for the dispersion. 2.5 μg/mL of MNPs were dispersed by ultrasounds for 30 minutes below 30°C. 2.5 μL of the solution was deposited on the surface of mica and dried at room temperature in the air. The diameters of MNPs were in the range of 10 nm to 100 nm.

A JPK (NanoWizard®3, Germany) MFM system was used for the imaging and manipulation of MNPs carried out in the air condition. The MFM used in the experiment was equipped with a closed loop scanner. The typical spring constant of the utilized magnetic probe was 3 N/m and the resonant frequency was 75 kHz (MagneticMulti75-G, BudgetSensors). The tip was magnetized by an external magnet field in the vertical direction.

A manipulation mode (contact) was used for drawing the capture path on the substrate surface and picking up the target magnetic nanoparticle. To successful pick up the target nanoparticle, the helical curve was drawn from the outer to inside and the ending position was located on the target nanoparticle, and the curve with at least 3 turns.

4.2.3 Results and Discussions

In the experiment, the MNPs with a diameter of 30 nm were manipulated by the proposed method. The results were presented in Fig. 4.10. The target particle was selected and labelled by a circle, as shown in Fig. 4.10(a), whereas the corresponding magnetic domain distribution was presented in Fig. 4.10(b). The capture path used for the target particle manipulation was drawn as a green helical curve, as presented in Fig. 4.10(c). The magnetic tip followed the designed helical path approaching to the target particle and finally the particle was attached onto the tip surface. The particle was removed from the mica surface after the tip retracted, as presented in Fig. 4.10(d) and the corresponding magnetic domain of the particle did not exist, as shown in Fig. 4.10(e). The lift height was 7 nm for MFM imaging. The speed for the capture of the particle was 0.3 μm/s and the applied force was 45 nN.

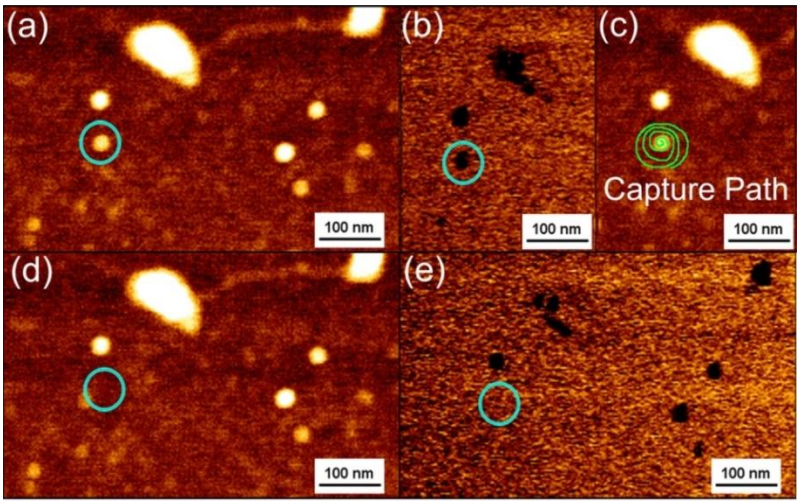

Fig. 4.10 Images of MNPs previous to and following the manipulation by MFM. (a) The topography image of MNPs before the pick-up. (b) The corresponding MFM image of (a). (c) The helical curve designed as the capture path for the particle pick-up. (d) The topography image of the target particle after the pick-up. (e) The corresponding MFM image of (d).

For the evaluation of the method in terms of flexibility and control capability, a series of manipulations were successively carried out for three targeted MNPs. The results were presented in Fig. 4.11. It can be clearly observed that particle P1 with a diameter of 25 nm, particle P2 with a diameter of 15 nm and particle P3 with a diameter of 40 nm were successively picked up. In the experiment, the lift height was 7 nm for MFM imaging. The capture speed of particles was 0.3 μm/s and the push force was 60 nN. The arrows were corresponding to the target particles.

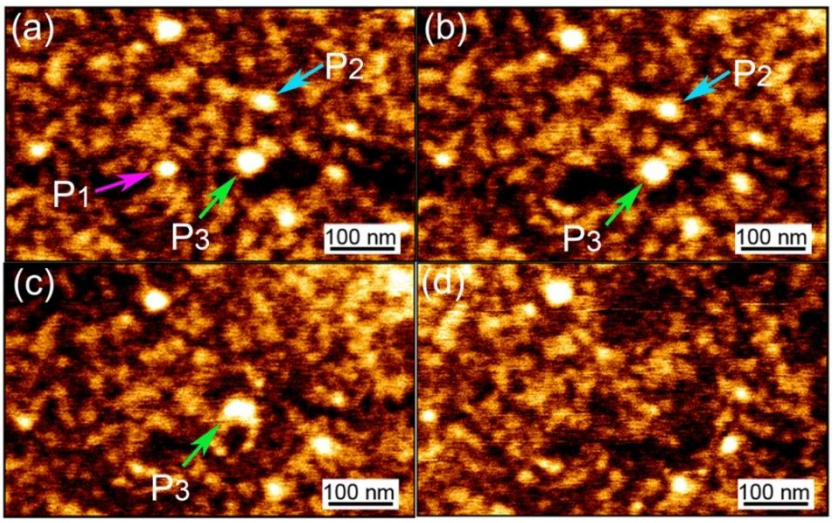

Fig. 4.11 Successive manipulations of three MNPs. (a) Topography image of MNPs previous to the pick-up, particles P1, P2 and P3 displayed with arrows. (b) The result following the pick-up of particle P1. (c) The removal result of particle P2. (d) The following pick-up result of particle P3.

Xu et al. [193] used a hybrid-conductive AFM probe to manipulate Au nanoparticles. Mirowski et al. [194] provided the magnetic field gradient by magnetic probe to sort out magnetic particles on an microfluidic platform with an array of magnetic trap elements and the particle size was 1 μm in diameter. Currently, the common methods used for the manipulation of single nanoscale objects by AFM are pushing, rolling,

cutting, drilling and dissecting [113-115]. Also, the main methods are pushing and sliding of the particle along a linear path. With the methods, the target particle can be moved from one position to another position on the surface [115-117]. For the particles with disordered and complicated distributions, it is hard to design a simple straight line path for the tip to push a selected particle to the target location. In practice, the linear path should be precisely determined for each operation, and it is difficult to be successfully performed. Due to the limitation of the tip radius, reliability and repeatability of the AFM system, flexible manipulation of particles with a size below 100 nm is still a challenge [117].

Because the interaction forces between the substrate surface and the particle are difficult to overcome in the vertical direction, it is hard to separate the particle away from the surface and pick up it by the method of simple tip approaching and retracting.

For the proposed helical path method, the pushing force and tangential force in the horizontal direction make the particle moving on the surface when the tip contacts the particle. Due to the role of tangential force, the particle will be rotated under the moment and the contact area between the particle and the surface will be decreased. Accordingly, the forces between the particle and the substrate surface are reduced.

In the experiments, MNPs were successfully picked up and removed with the proposed method. The success rate of pick up the MNPs by the proposed method was >90 % for the MNPs with the diameters of 10~90 nm, and the success rate was ~50 % for the MNPs with the diameters of 100~200 nm.

4.3 External Magnetic Field Aided MNPs Releasing

4.3.1 Application of External Magnetic Field

The probe cleaning process is shown in Fig. 4.12. With this method, the MNPs can be releasing from MFM probe tips. The BOPP film with a square size of 10 mm×10 mm, which was pasted on the magnet and put on the sample stage, was used as a sample. Before pushing the tip into the BOPP film by manipulating the MFM, the contact mode was used for imaging the BOPP film and a relatively flat area was selected as the target area. In the cleaning process, the probe was placed above the target area, as shown in Fig. 4.12(a). The system parameters were adjusted to provide a loading force on the probe to push the tip into the BOPP film with a depth of 50-100 nm and hold for 5 seconds, as shown in Fig. 4.12(b), and then the probe was lifted from the BOPP film, as shown in Fig. 4.12(c). The procedure was repeated five times.

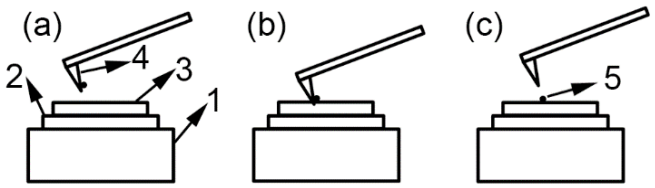

Fig. 4.12. Illustration of a probe cleaning process. 1 is the sample stage, 2 is the permanent magnet, 3 is the BOPP film, 4 is the probe tip, and 5 is the magnetic particle (contaminant)**.**

The Young's modulus of the BOPP film was 2.2 GPa, far less than that of the silicon probe ranged from 132 GPa to 190 GPa [195]. Because of the good stretch property and the Young's modulus of the BOPP film, it was suitable for the cleaning of contaminated probes and no damage was caused to the probes.

There are mainly four types of adhesive forces between the MFM probe and the magnetic contaminants including the magnetic force, van der Waals force, electrostatic force and capillary force. The mechanisms and characteristics of the forces are different, and the separation force should be larger than those adhesive forces to remove the contaminants from the magnetic probe.

Fig. 4.13 shows the mechanical model of cleaning magnetic particles. In Fig. 4.13, *A* is a BOPP film, *B* is a permanent magnet, F_1 is the resultant force between the magnetic particle and the probe, F_2 is the resultant force of the magnetic particle in the vertical downward direction during cleaning, *Z* is the vertical axis, β is the angle between F_1 and the *Z* axis, a_1 and a_2 are the angles viewed from the probe side with the centre line on the both sides, and $a_2 > a_1$. The angle a_1 was 10 degrees and a_2 was 30 degrees in the experiments.

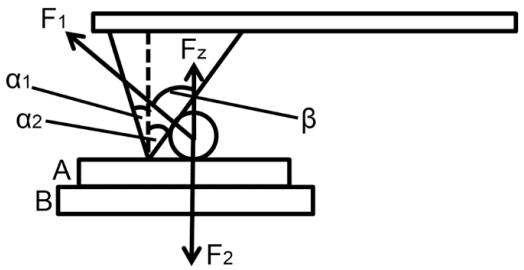

Fig. 4.13 Mechanical model of cleaning magnetic particles.

The force between the magnetic particle and the probe can be written as

$$F_1 = F_{mg} + F_{van} + F_e + F_c \tag{4.8}$$

where, F_{mg} is the magnetic force, F_{van} is the van der Waals force, F_e is the electrostatic force and F_c is the capillary force.

The component of F_1 in the Z axis can be computed by

$$F_Z = F_1 \cos\beta = F_1 \cos(90 - \alpha_2) \tag{4.9}$$

The sum of adhesive forces in the Z direction can be expressed as

$$F_2 = G + M + F_a \tag{4.10}$$

where, G is the gravity of the magnetic particle, M is the magnetic force from the magnet, and F_a is the adhesive force between the magnetic particle and the BOPP film. The magnetic contaminants can be adhered to the BOPP film if $F_2 > F_z$, so that the component M in F_2 needs to be large enough. A high retentivity permanent magnet was used in the experiments. The experiments are described in the following sections.

4.3.2 Experiments

A common BOPP film with the thickness of 25 μm was used in the experiments. The density of the BOPP film was 0.91 g/cm^3, and the tensile strength in the machine direction was ≥125 MPa and that in the transverse direction was ≥ 220 MPa. The Young's modulus in the machine direction was 2.2 GPa [196]. A permanent magnet (NdFeB N52) with the retentivity of 12200 Gauss, diameter of 10 mm and thickness of 2 mm was used together with the BOPP film in the experiments. Fe_3O_4 magnetic particles with the diameter range from 50 nm to 100 nm were used as magnetic contaminants.

An MFM (JPK Nona Wizard) was used for the manipulation and measurement of the magnetic samples. The magnetic probe Magnetic Multi75-G (Budget Sensors) was used in the experiments. The resonant frequency of the magnetic probe was 75 kHz

and the spring constant was 3 N/m. The FEI QUANT-250 FEG SEM was used for observing the probe with an everhart-thornley detector in a high vacuum environment.

4.3.3 Results and Discussions

The separation force and the adhesive force between the contaminated probe and the BOPP film and the magnet have been studied, and the force-displacement curves of the contaminated probe pushing into the BOPP film are shown in Fig. 4.14. It can be seen from each of the curves that there is a jump of the cantilever in the process of retraction. It indicates that an attractive force was presented when the tip was separating from the surface of the BOPP film. For curve A, the loading force was 35 nN and the separation force was 280.3 nN. The loading forces of curves B and C were 60 nN and 90 nN, and their corresponding separation forces were 298.1 nN and 314.9 nN. When the tip was separated from the surface of the BOPP film there was a pulling force generated by the BOPP film, as marked by a black square in Fig. 4.14.

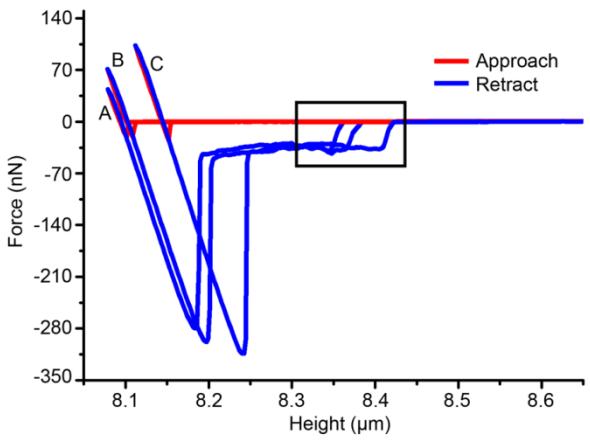

Fig. 4.14 Force-displacement curves of the contaminated probe pushing into the BOPP film.

In the cleaning process, the magnetic particles and the probe were both affected by the permanent magnet. To study the adhesive force between the magnetic particles and the BOPP film, the relationships between the loading forces and the separating forces from the uncontaminated magnetic probe and the contaminated magnetic probe were obtained, as shown in Fig. 4.15.

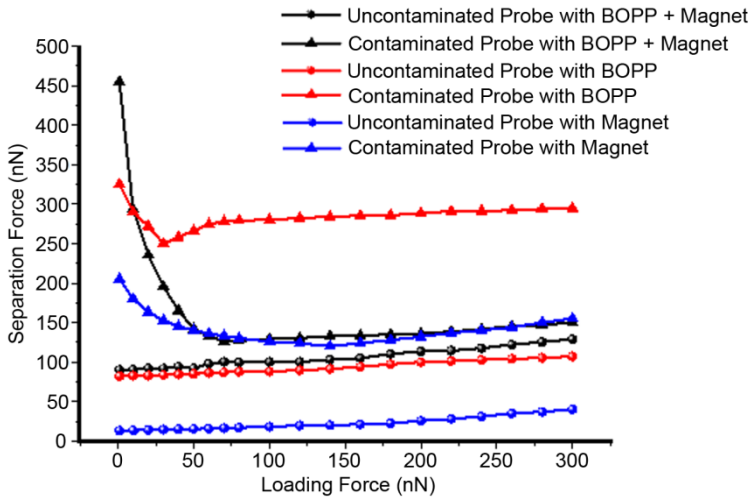

Fig. 4.15 Relationships between the loading forces and the separating forces of the uncontaminated magnetic probe and the contaminated magnetic probe.

In the experiments, different setpoint voltages were set to change the loading force of the cantilever. It can be seen that the separating forces are slowly increased with the increase of the loading force for the uncontaminated probe. Because of the good stretch property and the Young's modulus of BOPP film, the separating force from the BOPP film is larger than that from the magnet surface, and the separating force from the BOPP film together with the magnet is larger than that from the BOPP film itself due to the effect of the external magnetic force field. For a contaminated probe, separating forces are rapidly decreased with the loading force increased from 0 nN to 50 nN which indicates that the magnetic particles are removed from the magnetic

probe, and the separating forces are changed slowly with the increase of the loading force from 50 nN to 300 nN. It can be observed that the separating forces obtained from the BOPP film together with the magnet are all rapidly decreased, which demonstrates that the adhesive force between the magnetic contaminant and the BOPP film together with the external magnetic field is greater than the magnetic force between the magnetic contaminant and the probe.

The cleaning results of a magnetically-contaminated MFM probe were observed by SEM, as shown in Fig. 4.16. Fig. 4.16(a) and (b) show the results before and after cleaning once, respectively. It can be seen that part of the magnetic contaminants marked by the circle was removed. Fig. 4.16(c) is the probe image before the cleaning and Fig. 4.16(d) shows the result after cleaning three times. It is clear that the magnetically-contaminated MFM probe can be cleaned by the method of using the BOPP film together with the external magnet field. In 40 experiments, the success rate was ~50% for cleaning once, and the success rate was ~85% after cleaning 6-8 times for the magnetically-contaminated MFM probes.

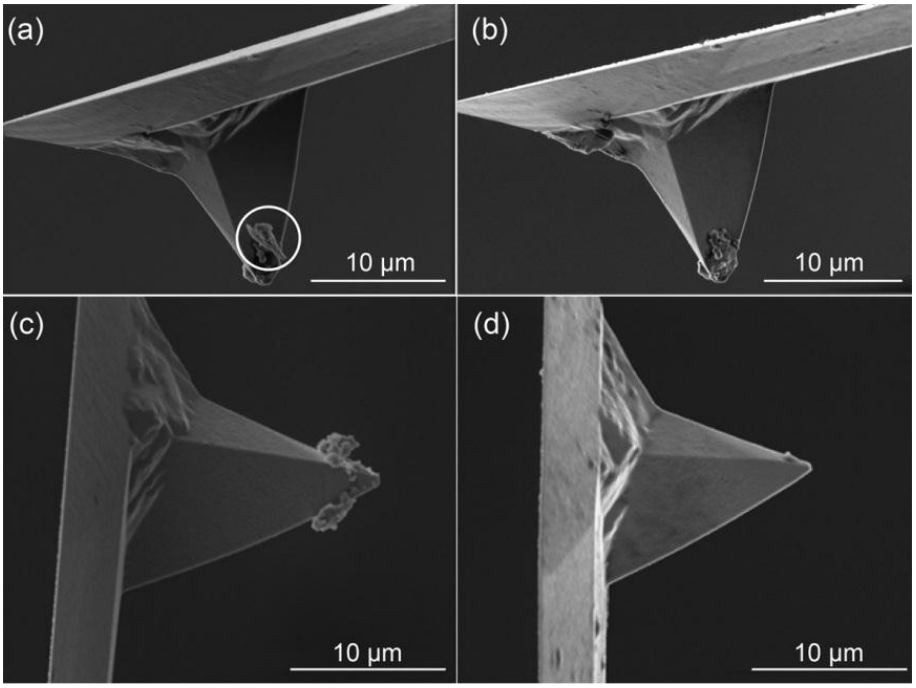

Fig. 4.16 SEM images of the magnetically-contaminated MFM probes before and after cleaning. (a) is the image of the probe before cleaning and (b) is its corresponding result after cleaning once. (c) is the image of the probe before cleaning and (d) is its corresponding image after cleaning three times.

To examine the imaging capability after the cleaning of the magnetically-contaminated MFM probe, the morphological images of magnetic particles and their corresponding magnetic images were obtained, as shown in Fig. 4.17. It can be seen from the figure that there are drag lines in the morphological and MFM images caused by the contaminated MFM probe, as shown in Fig. 4.17(a) and 4.17(b). The magnetic particles in the morphological image and the magnetic features of the MFM image are clearly recognized by the probe after the cleaning, as shown in Fig. 4.17(c) and 4.17(d).

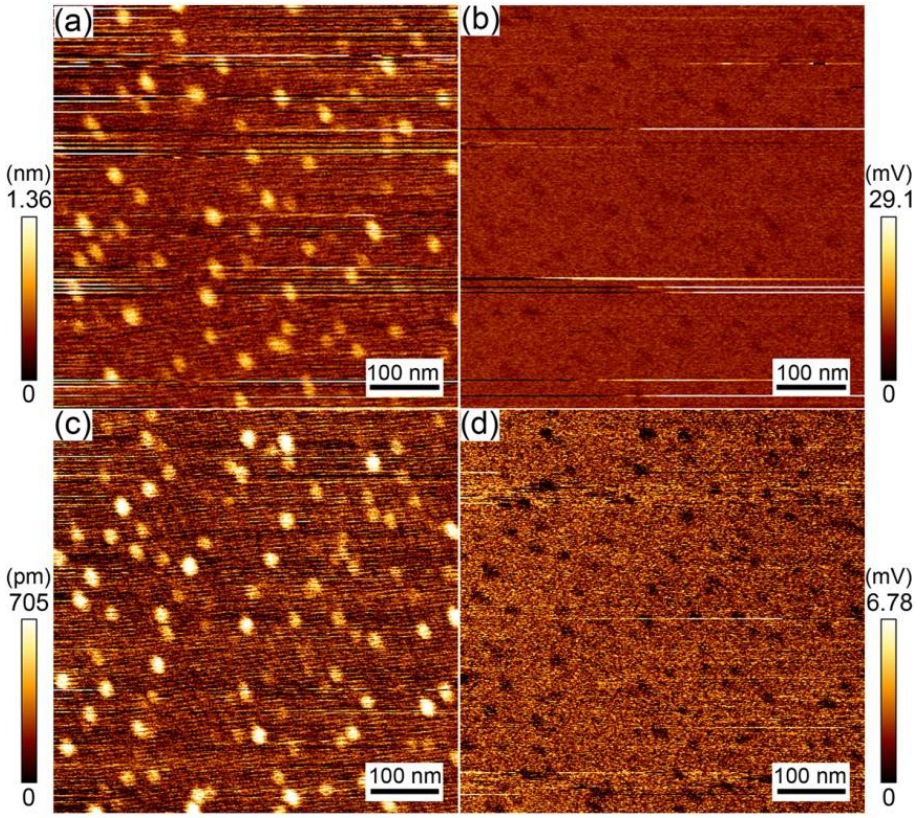

Fig. 4.17 MFM images of magnetic nanoparticles. (a) and (b) are the morphological and magnetic images obtained by a contaminated MFM probe; (c) and (d) are the morphological and magnetic images obtained by the MFM probe after cleaning.

It is clear that the quality of the morphological and magnetic images obtained with the cleaned MFM probe is significantly improved. The experiment results indicate that the BOPP film together with an external magnetic field is effective for cleaning the magnetically-contaminated MFM probe.

4.4 Summary

This chapter firstly represents the research in the using of chemical co-precipitation

method for the synthesis of Fe_3O_4 MNPs. PEG-2000 was used as the dispersant to prevent the particles from agglomeration. XRD, SEM, AFM and MFM were used to characterize the properties of Fe_3O_4 MNPs. The experiment results have shown that the Fe_3O_4 MNPs with the average diameter of 100 nm were successfully obtained by changed the stoichiometric ratio of Fe^{2+}/Fe^{3+} from 1:2 to 2:3 and the chemical reaction were efficient, and the fabricated Fe_3O_4 MNPs were paramagnetic and easily separated from the solution by external magnetic field.

Secondly, this chapter presents a helical curve as the capture path for MNPs lifting up. Due to the interactions of tangential, pushing and magnetic forces caused by magnetic probe movements, the resistance force was reduced and the particle attached on the surface of the magnetic probe tip when the tip contacted the particle. The experimental results indicate that with this method MNPs can be picked up successfully. The method significantly improves the precision and flexibility of manipulations, and provides a guide for the manipulation of MNPs for different applications.

Finally, this chapter introduces the method of separation of MNPs from tip surface to release them using a BOPP film together with an external magnetic field, which was developed in this research. An MFM system was used for manipulating the tip to push into the BOPP film with a depth of 50-100 nm under a magnetic field and hold for 5 s. The experimental results have shown that this method is effective for separation of MNPs from MFM probes. It can greatly improve quality of magnetic imaging, prolong the service life of magnetic probes, and reduce the experimental costs in many MFM applications. Especially, the work develops applications of the MFM working in biomedicine.

CHAPTER 5

SELECTION OF CANCER CELLS THROUGH INVESTIGATING MORPHOLOGICAL FEATURES AND MECHANICAL PROPERTIES

It is necessary to select cancer cells that have certain levels of viability for the further investigations of the effect of anticancer drugs. Changes in the morphological features and mechanical properties of cancer cells, after applying anticancer drugs to the cells, reflect their viability [197, 198]. Inspired by the research that found that some tumour cells have single nucleus and others have more nuclei [143-145, 154-156], this research investigated the differences in viability of the two types of cells in terms of their drug resistance after being treated with anticancer drugs. This research discovered the differences from the perspectives of the morphological features and the mechanical properties between multinuclear and mononuclear cancer cells. The differences have the significance to the selection of cancer cells for the further MNPs-based treatment investigation.

Research presented in this chapter aims to produce recommendations regarding the selections of multinuclear or mononuclear cancer cells according to their morphological features and the mechanical properties. To achieve this goal, the morphology features (height, roughness, length and width) and mechanical properties (adhesive force and Young's modulus) of multinuclear and mononuclear SW480

colon cancer cells were measured with AFM and fullerenol (C_{60}(OH)x) was used as an anticancer drug in this research.

5.1 Morphological Feature Investigation

The aim of this investigation is to find the relation between cell viability and cell morphological features. Experiments carried out in this research confirmed the relation and, more important, revealed the differences in drug resistance between mononuclear cells and multinuclear cells. MTT (methyl thiazolyl tetrazolium), which can measure the cell viability of cancer cells before and after being treated with anti-cancer drugs but is unable to show the morphological features, was used as a reference so that the changes in morphological features can be linked to the cell viability.

5.1.1 Experiments

Colon cancer cells SW480 (CBTCCCAS, Shanghai, China) were used in the experiments. Fullerenol (C_{60}(OH)x) [199-201] (Hengqiu Tech, China) was used as anticancer drugs [202-206] due to its unique structures and properties. Dimethyl thiazolyl tetrazolium bromide (MTT) was used measure cell viability. An Agilent 5500 AFM system, as shown in Fig. 5.1, was used for the measurement of morphology features (height, length, width and roughness) of SW480 cells in the air. SPSS 18.0 software was used to perform statistical analysis.

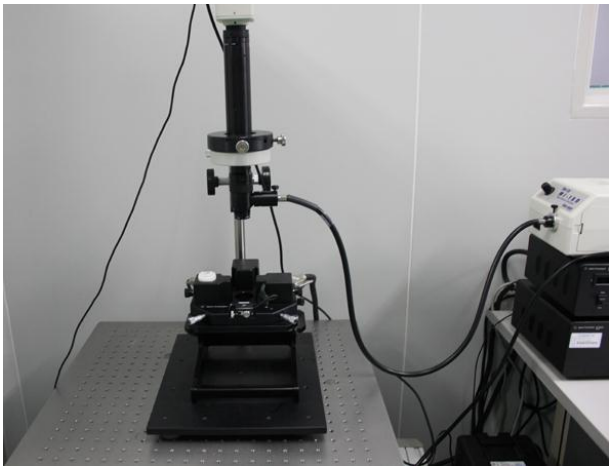

Fig. 5.1 Agilent AFM system.

SW480 cells were maintained under 5% CO_2 at 37 ℃. This is the standard condition for biological experiments which causes the least damages to the cell. Also by following the biological standard, the cells were attached to 0.01 mg/mL Poly-L-Lysine (HyClone) treated glass bottom culture dishes (18 mm × 18 mm) and were cultured in the RPMI-1640 media (HyClone) including 10% fetal bovine serum (FBS) (HyClone).

In this work, SW480 cells were divided into three groups, namely, control group where no fullerenol was applied to the cells, 1 mg/mL group where the fullerenol concentration of 1 mg/mL was applied to SW480 cells, and 2 mg/mL group where fullerenol concentration of 2 mg/mL was applied. The cells in the last two groups were further divided into three sub-groups where the cells were treated by fullerenol for 24, 48 and 72 hours before the measurement experiment to study their drug-resistance difference. It is normal in biological experiments that cells are examined after they are treated for different time periods.

In the experiments with MTT, SW480 cells were planted (2×10^4) in a 96-well plate

and incubated at 37 ℃ for 48 hours to confirm that the number of the cells is sufficient and the cells are in the state that is good enough to assay MTT. They were then divided into the three groups treated with 0 mg/mL, 1 mg/mL and 2 mg/mL of fullerenol and incubated for 24 hours for 1/3 cells of each group, 48 hours for the second 1/3 cells in each group and 72 hours for the rest cells in each group, respectively, as mentioned earlier. Following the normal practice in biological experiments, three steps were performed:

- 20 μL of 5 mg/mL dimethyl thiazolyl tetrazolium bromide (MTT) was added to each well.
- Each well was treated with the 150 μL DMSO solution after the incubation at 37 ℃ for 4 hours and all media were aspirated
- The growth inhibitory of cells was measured using the microplate reader (Sanco, China) at an absorbance wavelength of 570 nm.

These three steps were repeated to all three sub-groups.

To study the morphological features of the cells by AFM, SW480 cells were also divided into three groups and further three sub-groups, as described earlier. They were immersed in 2.5% gluteraldehyde for 15~20 minutes to have their structures best fixed at their status and save their morphology. The samples were then rinsed three times with phosphate buffer saline (PBS) and naturally dried up at the room temperature and humidity. The prepared samples were stored at 2~4 ℃ in the dark to minimise changes in morphological features from their current status.

With the AFM, the tapping mode was used for imaging, the scanning rang was varied

from 20 μm × 20 μm to 90 μm × 90 μm, and the scanning speed was 0.2 line/s. The tip radius was 10 nm. The thickness of cantilever was 4 μm, and the width and length were 30 μm and 125 μm, respectively. The normal spring constant of cantilever was 40 N/m, and the resonance frequency was 300 kHz (Tap300, BudgetSensors).

10 mononuclear cells from the control group, the 1 mg/ml group and the 2 mg/ml group, respectively and 10 multinuclear cells from the control group, the 1 mg/ml group and the 2 mg/ml group, respectively were used to measure their morphological features with AFM. In the experiments, with the help of optical microscope, the target cell was selected. Moving the tip located the selected cell and set the scanning parameters, including scanning range, speed, pixels and setpoint. Approaching the tip and scanning to obtain the images of the cells. The height, length, width and roughness features of each cell in each group were produced by applying image processing on the images obtained by the AFM using the software called "Pico Image Expert 6.2" from Agilent (USA).

Statistical analysis was then performed using SPSS 18.0 software. One-way analysis of variance (ANOVA) was used to evaluate the data distribution. Data were shown as Mean±SD. The value of $p<0.05$ was considered significant and $p<0.01$ was considered highly significant.

5.1.2 Results and Discussions

Fig. 5.2(a-c) show the optical images of SW480 cells of the control group, the 1 mg/ml group and the 2 mg/ml group, respectively, with 48 hours incubation. In Fig. 5.2(a), the shapes of the SW480 cells are normal (like fusiform) and there are a large

number of cells in control group. The shapes of SW480 cells treated with 1 mg/ml fullerenol are spherical and the numbers of the cells decreased, as shown in Fig. 5.2(b). Those cells treated with 2 mg/ml fullerenol are with more round shapes and with the numbers is further reduced, as shown in Fig. 5.2(c). It clearly observed that with the increase of the concentration of fullerenol, the number and the size of cells are declined. This result is in line with the result with MTT assay which evaluates cell viability through the growth inhibitory. Fig. 5.2(d) shows the results of cell viability distributions of SW480 cells after treated with two concentrations of fullerenol for 24, 48 and 72 hours with MTT. It can be seen that the viabilities of SW480 cells after the treatment with 2 mg/mL fullerenol are smaller than those cells that were treated with 1 mg/mL fullerenol.

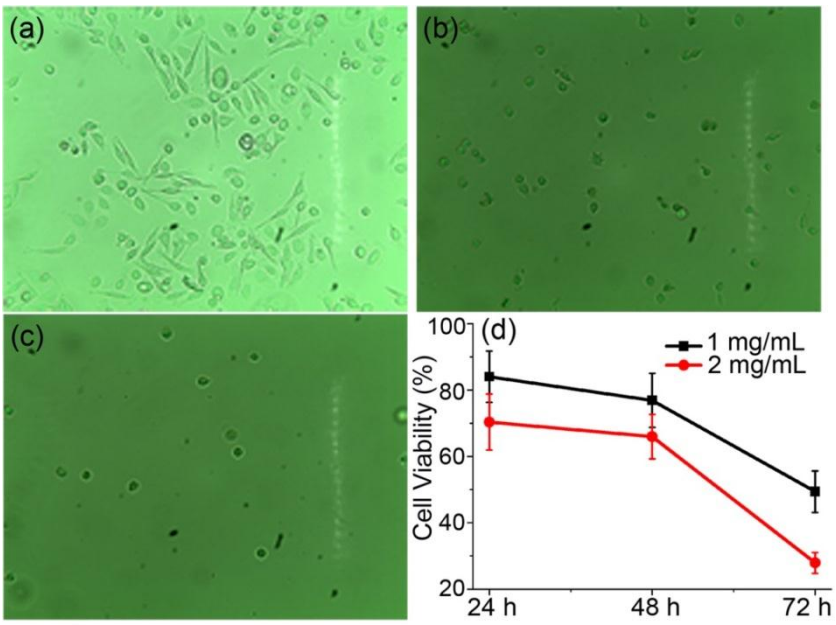

Fig. 5.2 Optical images and viabilities of SW480 cells after the treatment with two concentrations of fullerenol. (a) Control group, (b) treatment with 1 mg/ml fullerenol, (c) treatment with 2 mg/ml fullerenol, and (d) distributions of SW480 cell viabilities (p<0.05, when compared with the control group).

Fig. 5.3 shows the AFM morphological images of control group, 1 mg/mL group and 2 mg/mL group, respectively, fullerenol treated for 24, 48 and 72 hours. The colour bar indicates the height of the cells. The image resolution is 512×512 pixels. The scan range is 60 μm × 60 μm. It has been found that the shapes of SW480 cells treated with the fullerenol have been changed, whilst, the shape of the cells in control group are normal (like fusiform) as shown in Fig. 5.3(a, d, g). The cell heights increased and length/width decreased with the treated time and fullerenol concentrations increased. For the groups treated with fullernol for 24 hours, Fig. 5.3(a-c), the shape changes of cells are smallest compared with 48 and 72 hours groups. The shape changes of cells after treatment with 1mg/mL and 2 mg/mL fullerenol for 48 and 72 hours are obviously, as shown in Fig. 5.3(e, f, h, i). And it can be seen from Fig. 5.3(i) that the cells after 2mg/mL fullerenol treatment for 72 hours, the height of the cells too higher to be scanned and lead distortions where the drag lines can be found.

To analysis of the morphological features of mononuclear and multinuclear cancer cells, the groups treated with fullerenol for 48 hours were selected because the cells after 48 hours culture have the best states (not too higher to be scanned) and changed obviously. Fig. 5.4 shows AFM images of mononuclear and multinuclear SW480 cells incubated with fullerenol for 48 hours. Fig. 5.4(a) is the 3D structure of mononuclear SW480 cell. Fig. 5.4(b, c) show the 3D structures of multinuclear cells. It can be clearly seen that there are two nuclei in Fig. 5.4(b) and three nuclei in Fig. 5.4(c).

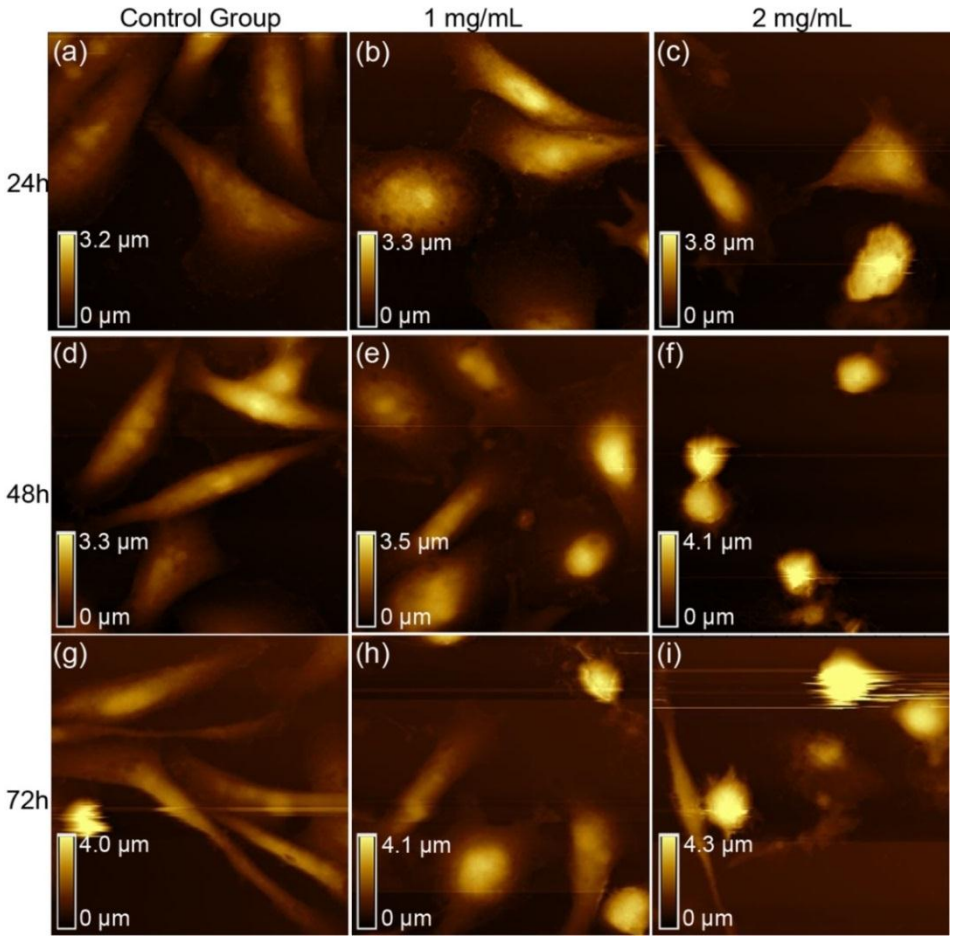

Fig. 5.3 AFM images of SW480 cells incubated with fullerenol.

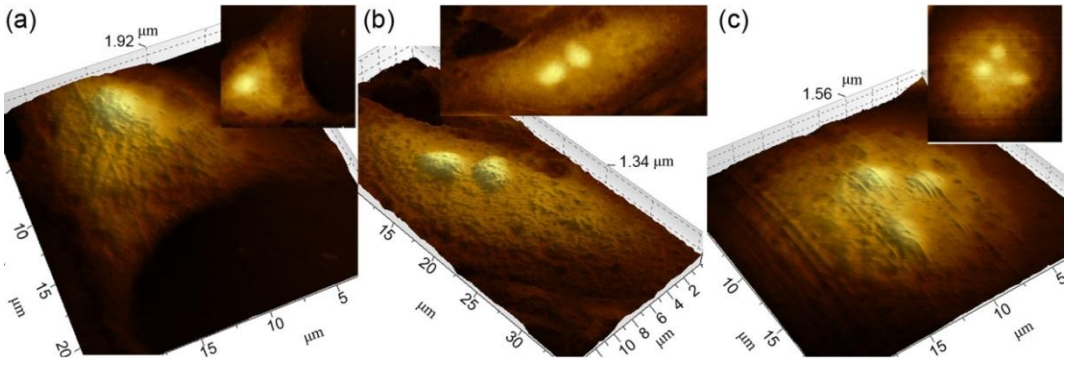

Fig. 5.4 AFM images of mononuclear and multinuclear SW480 cells incubated with fullerenol for 48 hours. (a) is the 3D structure of mononuclear SW480 cell. (b) and (c) are the 3D structures of multinuclear SW480 cells.

Fig. 5.5 shows the distributions of height, length, width and roughness of mononuclear and multinuclear SW480 cells in the control group and the two groups treated with fullerenol for 48 hours. Fig. 5.5(a) is the mononuclear SW480 cell and (b) is the two-nuclear SW480 cell. From the optical images, the number of nuclei can be seen clearly and they are labelled by arrows.

The height distributions of the mononuclear and multinuclear SW480 cells are shown in Fig. 5.5(c). The height of mononuclear cells in the control group is 2.16±0.29 μm, and after 2 mg/mL fullerenol treatment it is increased to 3.32±0.15 μm. The height of multinuclear cells in the control group is 1.74±0.20 μm and it is changed to 2.47 ±0.38 μm after 2 mg/mL fullerenol treatment.

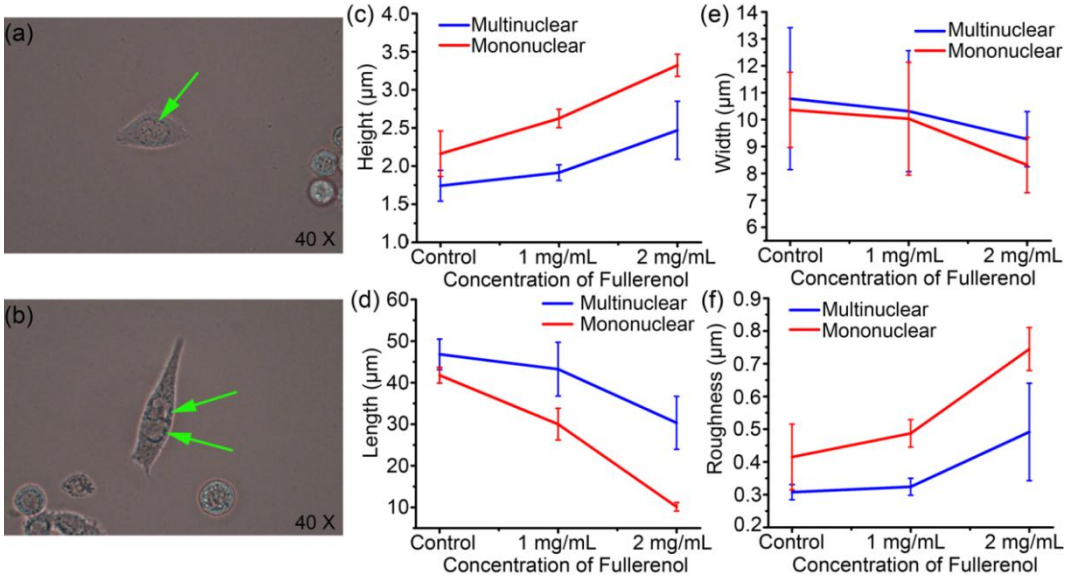

Fig. 5.5 Effects of fullerenol on the morphological features of SW480 cells. (a) and (b) are the optical images of mononuclear and multinuclear SW480 cells, respectively. (c) and (d) are the height and length distributions of mononuclear and multinuclear SW480 cells. (e) and (f) are the width and roughness distributions of mononuclear and multinuclear SW480 cells. $p<0.05$, when compared with the control group.

The length distributions of mononuclear and multinuclear SW480 cells are shown in Fig. 5.5(d). The length of mononuclear cells in the control group is 41.78±1.90 μm, and after 2 mg/mL fullerenol treatment it is decreased to 10.13±1.02 μm. The length of multinuclear cells in the control group is 46.82±3.68 μm and it is changed to 30.32±6.36 μm after 2 mg/mL fullerenol treatment.

The width distributions of mononuclear and multinuclear SW480 cells are shown in Fig. 5.5(e).The width of mononuclear cells untreated with fullerenol is 10.36±1.39 μm, and after 2 mg/mL fullerenol treatment it is decreased to 8.31±1.03 μm. For the multinuclear SW480 cells, the width in the control group is 10.78±2.64 μm, and after 2 mg/mL fullerenol treatment it is reduced to 9.27±1.03 μm.

The roughness distributions of mononuclear and multinuclear SW480 cells are shown in Fig. 5.5(f). The roughness of mononuclear cells untreated with fullerenol is 0.42±0.10 μm, and after 2 mg/mL fullerenol treatment it is increased to 0.74±0.07 μm. For the multinuclear SW480 cells, the roughness in the control group is 0.30±0.02 μm, and after 2 mg/mL fullerenol treatment it is increased to 0.49±0.15 μm. $p<0.05$.

The followings can be concluded from the experimental results:

- The changes in morphological features of SW480 cells are in line with the changes in the number of the cells after being treated with anti-cancer drug fullerenol.

- The changes morphological features of mononuclear SW480 cells are significantly larger than the multinuclear cells. Therefore, mononuclear SW480 cells are more sensitive to fullerenol than the multinuclear SW480 cells, and multinuclear SW480 cells have much stronger drug resistance than mononuclear

cells and, therefore, much stronger viability.

- For further MNPs-based treatment investigation, multinuclear cancer cells are more proper than mononuclear cells due to their stronger viability.

5.2 Mechanical Properties Investigation

Research represented in this section confirmed the stronger drug resistance of multinuclear cells than mononuclear cells from the aspect of their mechanical properties.

The mechanical properties referred in this work are adhesive force and Young's modulus which have a significant implication on drug resistance of cells. Young's modulus was obtained through Hooke's law and Hertz model. The former calculates adhesive force between AFM tip and cell based on the displacement of the cell when manipulated using the tip. The latter calculate Young's modulus with the obtained force [187, 207]. Hooke's law is expressed as

$$F = k \times \Delta L \tag{5.1}$$

where, k is the spring constant of the cantilever (k=0.03 N/m). ΔL is the deflection of the cantilever.

The original Hertz theory is an approximation for the contact of the very shallow indentation of two spheres in contact. For a pyramidal tip, the Hertz model can be modified as [208]

$$F = \frac{1}{\sqrt{2}} \frac{E}{1-v^2} \delta^2 \tan\alpha \tag{5.2}$$

where, F is the force. E is the Young's modulus of the sample. v is the Poisson's ratio (v=0.5). δ is the indentation depth calculated from the force-displacement curve. In this work, δ is in the range of 350-600 nm. α is the angle of the pyramidal tip (α=15 °).

5.2.1 Experiments

In this work, SW480 cells were prepared in the same way as in the investigation into the morphological features. They were divided into three groups, that is, control group, the 1 mg/mL fullerenol (Hengqiu Tech, China) concentration group and 2 mg/mL group. Each of these groups were further divided into three sub-groups according the time period they were treated, namely 24, 48 and 72 hours, before the experiments.

To investigate the mechanical properties of living cells using AFM, the cell culture glass slides were washed three times by the PBS to sweep away the suspend cells, and then immersed in RPMI-1640 media to keep the living environment. All steps were taken in a super-clean bench.

A JPK AFM system (NanoWizard®3, Germany) was used for the measurement of the mechanical features (adhesive force and Young's modulus) of living SW480 cells in the RPMI-1640 medium. The quantitative imaging (QI) mode was applied to obtain the force mapping images of the living cells and the loading speed is 200 μm/s. The scan rate was in the range of 0.5-0.8 Hz. The probe used in the experiments was MLCT (BRUKER). The tip radius was 20 nm. The thickness of cantilever was 0.55 μm, and the width and length were 20 μm and 225 μm, respectively. The resonance

frequency of cantilever was 15 kHz and the spring constant was 0.03 N/m.

For measuring the adhesive force, at least 10 cells were detected in each of the groups (control group, 1 mg/ml and 2 mg/ml groups) and 15 force curves were recorded for each cell. The AFM force-displacement curves were obtained from measuring the nucleus areas of cells [209]. 5 cells were studied in each of the groups and 100 measurements were made for each cell to investigate the Young's moduli. The distributions of Young's moduli were obtained by Gaussian curve fitting. The probing positions were the nucleus areas of cells. The adhesive forces and Young's moduli were obtained by image processing software "JPKSPM Data Processing" from JPK Instruments AG (Germany).

5.2.2 Results and Discussions

Fig. 5.6 shows the adhesive force images of mononuclear and multinuclear SW480 cells after the treatment with 1 mg/mL fullerenol for 48 hours. The colour bar indicates the adhesive force of the cells. It can be seen that the adhesive forces between mononuclear cells and multinuclear cells are different. The optical microscope images in Fig. 5.6(b, d) show that the multinuclear cells are normal but the mononuclear cells are in apoptosis.

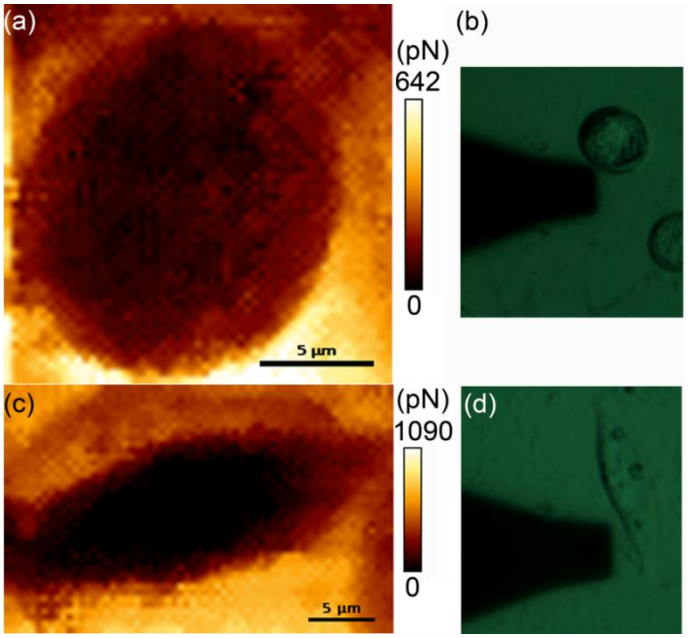

Fig. 5.6 Adhesive force images of mononuclear and multinuclear SW480 cells after the treatment with 1 mg/mL fullerenol for 48 hours. (a) is the adhesive force image of a mononuclear SW480 cell. The image resolution is 64×64 pixels. (c) is the adhesive force image of a multinuclear SW480 cell. The image resolution is 64×45 pixels. (b) and (d) are the detected cells captured by optical microscope.

Fig. 5.7 shows the force-displacement curves of living SW480 cells after the treatment with fullerenol for 48 hours. Fig. 5.7(b) is the enlarged image of the square area in Fig. 5.7(a). The distance between the lowest position and the base line is the adhesive force of tip-cell. It can be seen that the adhesive forces between the mononuclear and the multinuclear SW480 cells are different. It can be found that the adhesive forces are declined with the increase of the concentration of fullerenol and the adhesive forces of multinuclear cells are larger than those of mononuclear cells after the treatment with fullerenol with the same concentration.

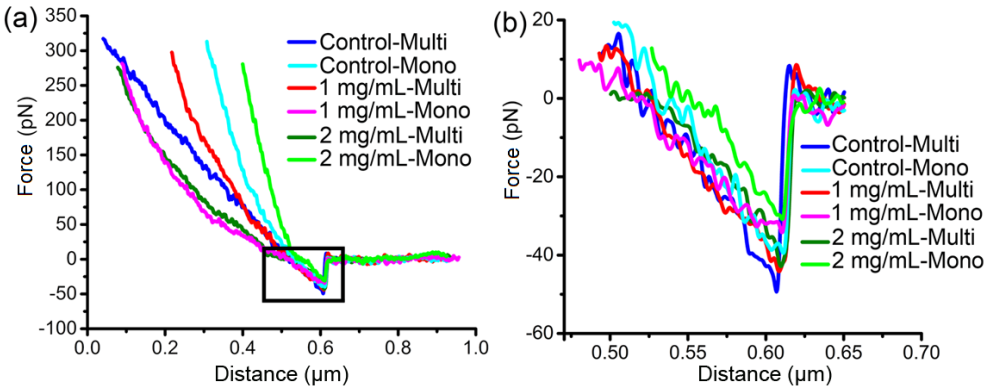

Fig. 5.7 (a) Shows the force-displacement curves of living SW480 cells in culture. (b) Shows the enlarged image of the square area of (a).

Fig. 5.8 shows the adhesive force distributions of multinuclear and mononuclear SW480 cells in the control group and the two groups treated with the two concentrations of fullerenol for 24, 48 and 72 hours. For the control groups untreated with fullerenol, the adhesive forces of mononuclear cells and multinuclear cells after incubation for 24 hours are 49.4±2.5 pN and 50.3±2.4 pN, respectively. The values are almost the same. After incubation for 48 hours, the adhesive force of mononuclear cells is 44.9±4.2 pN and the adhesive force of multinuclear cells is 49.0±2.4 pN. After 72 hours incubation, the adhesive force of mononuclear cells is 42.7±3.2 pN and the adhesive force of multinuclear cells is 47.6±1.9 pN. It can be seen that the adhesive force differences of multinuclear and mononuclear cells untreated with fullerenol are insignificant in the same time periods.

Fig. 5.8(a) shows the SW480 cells treated with fullerenol for 24 hours, the adhesive forces of mononuclear cells and multinuclear cells after treatment with 1 mg/mL of fullerenol are 42.2±2.9 pN and 48.7±1.5 pN, respectively. For the SW480 cells treated with 2 mg/mL of fullerenol for 24 hours, the adhesive forces of mononuclear cells and multinuclear cells are 33.9±3.5 pN and 48.5±3.5 pN.

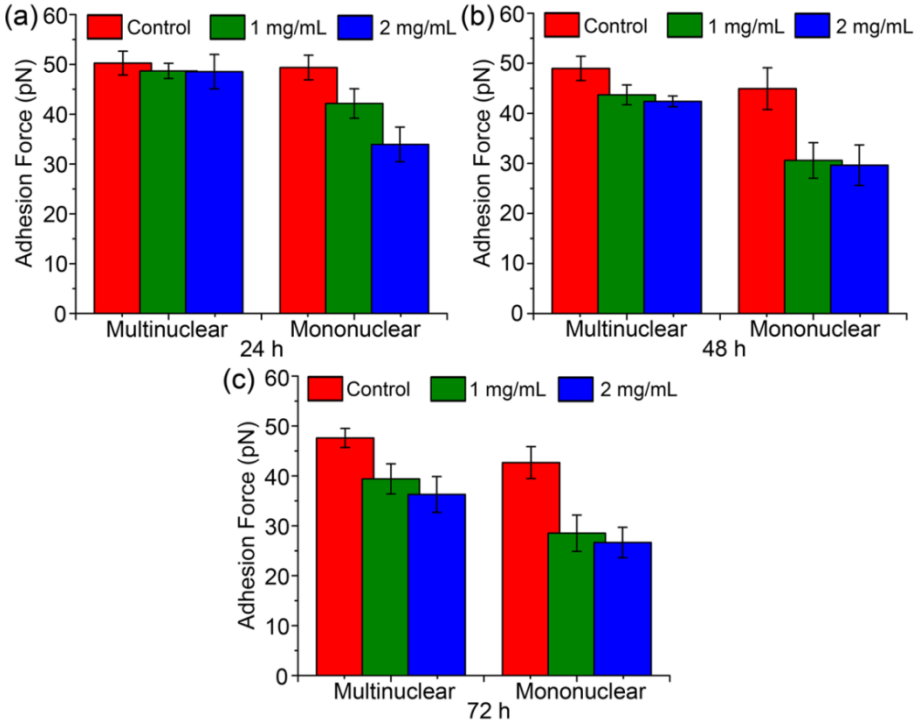

Fig. 5.8 Adhesive force distributions of multinuclear and mononuclear SW480 cells treated with fullerenol. $p<0.05$, when compared with the control group.

Fig. 5.8(b) presents the SW480 cells treated with fullerenol for 48 hours, the adhesive forces of mononuclear cells and multinuclear cells treated with 1 mg/mL of fullerenol are 30.6±3.6 pN and 43.7±2.0 pN. For the SW480 cells treated with 2 mg/mL of fullerenol for 48 hours, the adhesive forces of mononuclear cells and multinuclear cells are 29.7±4.0 pN and 42.4±1.1 pN.

Fig. 5.8(c) shows the SW480 cells treated with fullerenol for 72 hours, the adhesive forces of mononuclear cells and multinuclear cells treated with 1 mg/mL of fullerenol are 28.5±3.6 pN and 39.4±3.0 pN. For the SW480 cells treated with 2 mg/mL of fullerenol for 72 hours, the adhesive forces of mononuclear cells and multinuclear cells are 26.6±3.0 pN and 36.3±3.6 pN, respectively.

Significantly higher adhesive forces of multinuclear cells are observed than the

mononuclear cells after the treatment with 1 mg/mL or 2 mg/mL fullerenol for the same time periods. It can be concluded that after the treatment with fullerenol, the multinuclear SW480 cancer cells exhibit significant drug-resistance than the mononuclear cells.

Fig. 5.9 shows the distributions of Young's moduli of multinuclear and mononuclear SW480 cancer cells after treatment with fullerenol for 24, 48 and 72 hours. The Young's moduli are calculated from 5 cells in each of groups and 100 measurements were made for each cell, as shown in Table 5.1. $p<0.01$, when compared with the control group.

Fig. 5.9(a) shows the distributions of Young's moduli of SW480 cells exposed to fullerenol for 24 hours. For the multinuclear cells, the Young's moduli are distributed between 150-400 Pa. The Mean±SD modulus of the control group is 295.0±112.1 Pa, and those of the SW480 cells treated with 1 mg/mL and 2 mg/mL fullerenol are 297.7±104.3 Pa and 302.5±109.8 Pa, respectively. For the mononuclear cells, the Young's moduli of control group and the group treated with 1 mg/mL fullerenol SW480 cells are distributed between 150-400 Pa, and there are insignificant difference between their Mean±SD moduli, 311.8±142.3 Pa and 310.3±113.8 Pa, respectively. The Young's moduli of mononuclear SW480 cells treated with 2 mg/mL fullerenol are distributed between 200-500 Pa and the Mean±SD modulus is 357.8±111.8 Pa. It can be observed that after 24 hours treatment with fullerenol, the Young's moduli distributions of multinuclear cells and their Mean±SD values were not significantly changed. However, there is a significant difference in Young's moduli of the mononuclear cells treated with 2 mg/mL fullerenol group.

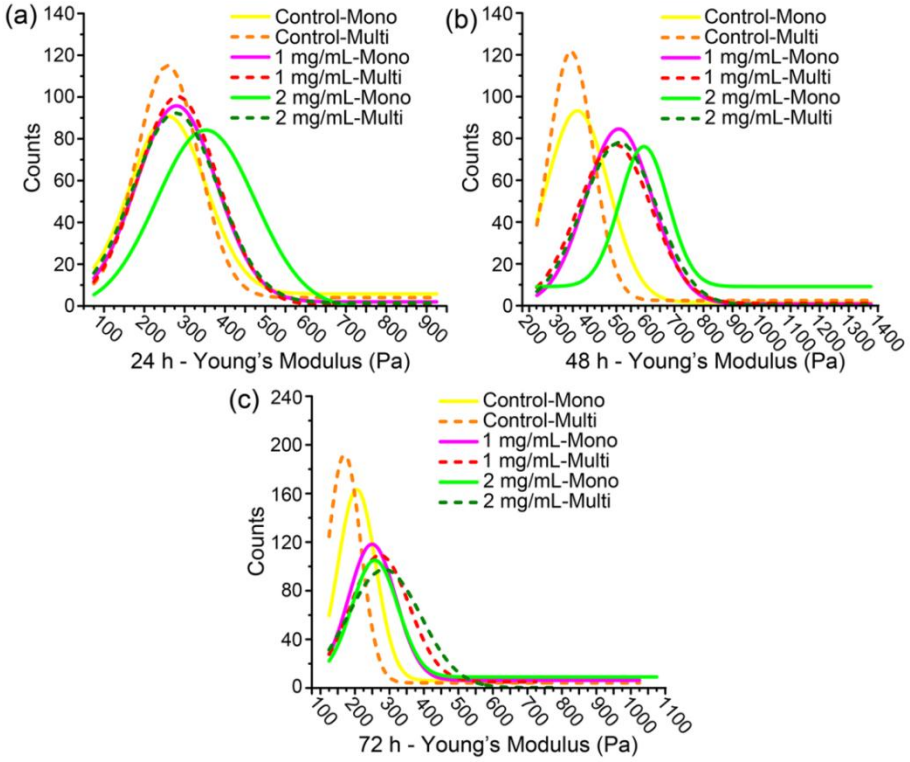

Fig. 5.9 Distributions of the Young's moduli of multinuclear and mononuclear SW480 cancer cells treated with fullerenol. $p<0.01$, when compared with the control group.

Fig. 5.9(b) shows the distributions of Young's moduli of SW480 cells exposed to the fullerenol for 48 hours. The Young's moduli of the multinuclear cells and mononuclear cells of control groups are distributed between 250-500 Pa and their Mean±SD moduli are 375.8±93.6 Pa and 395.9±113.5 Pa, respectively. The Young's moduli of the multinuclear cells treated with 1 mg/mL and 2 mg/mL fullerenol are distributed between 350-650 Pa and their Mean±SD values are 528.4±130.0 Pa and 536.3±125.1 Pa, respectively. The Young's moduli among the groups of multinuclear cells treated with fullerenol showed a small variation in their distributions and Mean±SD values. For mononuclear cells, the Young's moduli of the SW480 cells treated with 1 mg/mL fullerenol are distributed between 350-650 Pa and the Mean±SD value is 538.5±137.1 Pa. The Young's moduli of the SW480 cells after 2

mg/mL fullerenol treatment are distributed between 500-850 Pa and the Mean±SD value is significantly increased to 724.7±207.1 Pa. It can be stated that the Young's moduli of the mononuclear cells are significantly different from the multinuclear cells groups.

Table 5.1 Young's modulus (Pa) of SW480 cancer cells treated with fullerenol.

Group		Control Group	1 mg/mL	2 mg/mL
24 h	**Multi**	295.0±112.1	297.7±104.3	302.5±109.8
	Mono	311.8±142.3	310.3±113.8	357.8±111.8
48 h	**Multi**	375.8±93.6	528.4±130.0	536.3±125.1
	Mono	395.9±113.5	538.5±137.1	724.7±207.1
72 h	**Multi**	202.5±80.2	301.1±101.8	302.0±95.8
	Mono	235.5±83.0	316.8±152.2	377.2±226.5

Fig. 5.9(c) shows the distributions of Young's moduli of SW480 cells treated with fullerenol for 72 h. The Young's moduli of the control group of the multinuclear cells and mononuclear cells are distributed between 100-350 Pa, and their Mean±SD values are 202.5±80.2 Pa and 235.5±83.0 Pa, respectively. For the groups treated with 1 mg/mL fullerenol, the Young's moduli of multinuclear cells and mononuclear cells are distributed between 150-400 Pa, and their Mean±SD values are 301.1±101.8 Pa and 316.8±152.2 Pa, respectively. For the groups treated with 2 mg/mL fullerenol, the Young's moduli of multinuclear cells and mononuclear cells are distributed between 150-450 Pa and 150-400 Pa, respectively and the Mean±SD value increased from 302.0±95.8 Pa to 377.2±226.5. It can be observed that after the treatment with

fullernol, there is a significant change of the Young's moduli of mononuclear cells groups.

The experimental results can be summarised as:

- Young's modulus of multinuclear SW480 cells is significantly smaller than that of mononuclear cells after they were treated with fullerenol, regardless the dose of the drug and the time period treated to the cells.

- Young's modulus of multinuclear cells shows smaller changes than that of mononuclear cells when the dose of fullerenol increased from 1 mg/ml to 2 mg/mL

- Young's modulus of multinuclear cells shows similar changes as that of mononuclear cells when the dose of fullerenol was 1 mg/ml, but smaller changes with 2 mg/mL fullerenol.

The reason behind these experimental results may be explained as the following. Fullerenol influenced the conformation and the function of membranes of cells and deformed the protein in the binding residues [205, 210]. Thus, the skeleton and structure of cells were changed [211] and led to the alterations of mechanical properties [139]. Therefore, it can be conclude that the mononuclear SW480 cells are more sensitive to fullerenol than the multinuclear SW480 cells, and multinuclear cells have stronger drug resistance compared with mononulcear cells, as indicated by their adhesive force and Young's moduli.

5.3 Summary

Works reported in this chapter show that there are significant differences in the morphological features and mechanical properties between the mononuclear and multinuclear SW480 cells after treating them with fullerenol. The distributions of the height, length, width and roughness of the multinuclear SW480 cells untreated with fullerenol and treated with two concentrations of fullerenol are similar, but for the mononuclear SW480 cells, their distributions are clearly different. The adhesive force of mononuclear SW480 cells is significantly less than that of the multinuclear cells after the treatment with fullerenol for the same time period. The variation of Young's modulus of mononuclear SW480 cells is significantly larger than the multinuclear SW480 cells after exposure to the fullerenol for the same time period. The AFM results indicated that the mononuclear SW480 cells are more sensitive to fullerenol than the multinuclear SW480 cells, and the multinuclear SW480 cells exhibit a stronger drug-resistance than the mononuclear SW480 cells. This work provides a recommendation of selecting multinuclear cells as the target cells for the purpose of MNPs-based cancer treatment investigation.

CHAPTER 6

MNPS IMPLANTATION AND CELL-MNPS MANIPULATION

Culturing cells with drugs is a common method used to investigate cancer therapy in experiments [212]. However, traditionally the application of this method to cancer treatment is limited because of the lack of means of handling cells, targeting specific cells and measuring the nanoscale changes in cell structures to tailor the treatments. MNPs provide a new way to enhance the application. MNPs can be adhered to the surface of the cells and swallowed by the cells due to cells' cytophagic capability. The magnetic features of MNPs allow MNPs coated with drugs to be implanted into cells in more controllable manners and allow the cells treated with MNPs (cell-MNPs) to be manipulated by magnetic force. This chapter reports the research in MNPs implantation into the target SMCC-7721 cancer cells for tracing and manipulating the target cancer cells. For investigating the MNPs' toxicity, cell viabilities of SMCC-7721 and HL-7702 cells were studied. The distributions of SMCC-7721 cancer cells including cell-MNPs and those that were untreated with MNPs, both of which were manipulated with magnet were studied to evaluate the magnetic force manipulated capability of cell-MNPs. For more flexibly moving cell-MNPs to the target locations, a more controllable method with controllable electromagnetic magnets was studied.

6.1 Implant MNPs into the Cells

6.1.1 Method

To implant MNPs into cells, the process of penetrating cells with MFM probe was analysed. The process is illustrated in Fig.6.1. At the first, the tip approaches towards the cell at a constant rate and contacts the cell, as shown in Fig. 6.1(a). Then, the tip is pushed with an appropriate force further against the cell, resulting in the change in the shape of cell membrane, as shown in Fig. 6.1(b). When the membrane cannot bear the stress, it is punctured, as shown in Fig. 6.1(c). It is known that puncturing cell membrane is an instant process and the tip penetrates into the cell within a pretty short time. For the withdraw process of the tip from the cell, the cell membrane was gradually constricted to pull the tip surface, as shown in Fig. 6.1(d), and the MNPs will be stripped from the tip surface and remained within the cell.

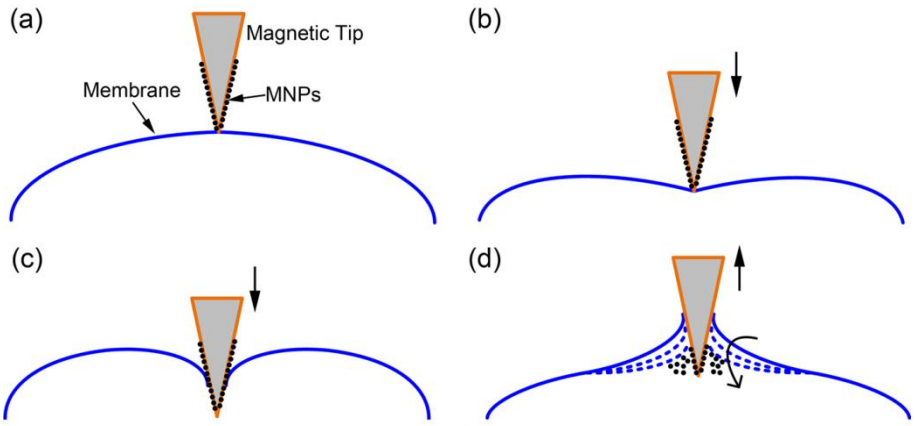

Fig. 6.1 Illustration of cell penetrating with magnetic tip functioned with the MNPs. (a) approached the tip and then contacted the cell membrane. (b) Continue approaching caused cell membrane changed. (c) Tip inserted into the membrane. (c) Tip retracted process. The arrows show the tip movement directions.

The process for implanting fluorescein functioned MNPs into a target cell is shown in Fig. 6.2. Before implanting the particles into the cells using the functioned magnetic probe, one of the SMCC-7721 cells is selected (as described in Chapter 5) as the target. Then, the probe is moved above it, as shown in Fig. 6.2(a). The "Setpoint" value of the MFM system is adjusted to provide an appropriate loading force on the magnetic probe to push the functioned tip into the target cell and keep for 3 ms, as shown in Fig. 6.2(b). Then the probe is retracted from the target cells. Because of the squeeze of the cell membrane, the fluorescein functioned MNPs could be remained into the cells, as shown in Fig. 6.2(c).

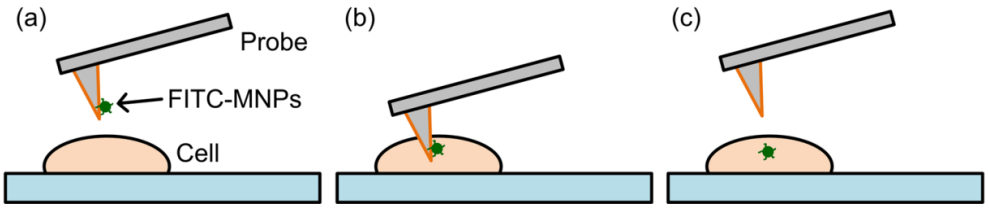

Fig. 6.2 Illustration of the MNPs implanted into the target cell by magnetic tip. (a) Selected the target cell. (b) Approached the tip and inserted into the target cell. (c) Retracted the tip from the cell surface.

6.1.2 Experiments

Human hepatoma cells SMCC-7721 (CBTCCCAS, Shanghai, China) were seed on the glass slide and cultured in RPMI-1640 media with a 10% FBS all from HyClone, and maintained at 37 ℃ and 5% CO_2. The cells were cultured for 48 hours to well adhere to the glass. Before implanted using magnetic probe, the cell culture glass slides were washed three times by the PBS to sweep away the suspend cells, and then immersed in RPMI-1640 media to keep the living environment. All steps were taken

in a super-clean bench.

Fluorescein isothiocyanat (FITC) fluorescein functioned Fe_3O_4@SiO_2 MNPs (FITC-MNPs) (Xi'an Ruixi Biological Technology, Shanghai, China) with diameter of 50 nm were used in the experiments. Due to MNPs' superparamagnetic properties, attractive magnetic forces exist between the magnetic tip and the MNPs, resulting in the MNPs being attached onto the tip surface. The magnetic probe was immersed in FITC-MNPs solution (50 μg/mL) for 8 hours to function these particles onto the tip surface. The functioned process was implemented in dark at 4℃ to prevent the fluorescence quenching. The tip was rinsed three times by the deionized water before the implanted manipulation [213].

The implanted manipulation was operated by JPK (NanoWizard®3, Germany) MFM system. The force spectroscopy mode was used to puncture the cell membrane. The tip used in the experiments was MagneticMulti75-G (BudgetSensors). The typical spring constant of the magnetic probe was 3 N/m and the resonant frequency was 75 kHz.

In the experiments with MTT, human hepatoma cells SMCC-7721 and hepatic cells HL-7702 were placed (3×10^3) in a 96-well plate and incubated at 37℃ for 24 hours. They were then treated with 0 μg/mL, 50 μg/mL, 100 μg/mL, 200 μg/mL and 500 μg/mL of MNPs and incubated for another 24, 48 and 72 hours, respectively. After that, MTT was assay as the steps described in Chapter 5.

6.1.3 Results and Discussions

Fig. 6.3 shows extend and retract force-displacement curves for implanting the MNPs into the target cells with a loading force of 160 nN. In the approaching process, magnetic tip contacted the cells firstly, as shown in point P1. Continually approaching the tip with the loading force leaded to a force relaxed (point P2) in the extend curve. The presence of P2 proved that the tip is penetrated into the membrane of the cells [214]. The force relaxed at point P3 is find in the retracted curve when the tip withdrawn. It confirmed that there is an adhesive force to prevent the tip away from the cell membrane.

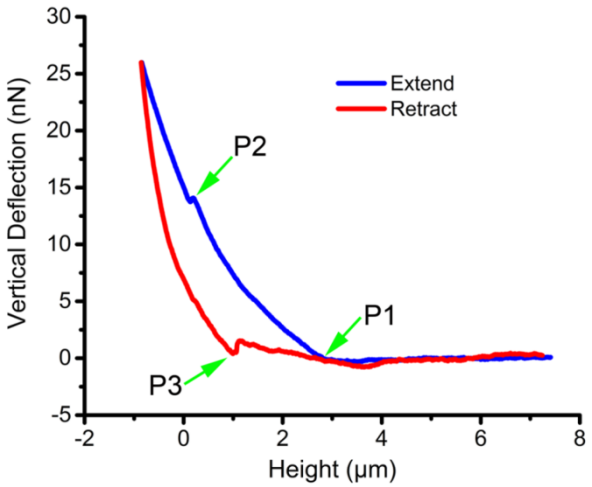

Fig. 6.3 Force-displacement curves of the tip inserted into the cell.

Fig. 6.4 shows the curves of the tip penetrated into a cell with different loading forces (extend curve). It is found that with the loading force of 120 nN, there is a force relaxed point P1. With the loading force of 130 nN, the relaxed point P2 and P3 are found. With the loading force of 140 nN, the relaxed point P4 and P5 are detected. With the loading force of 150 nN, the relaxed point P6 and P7 are explored. The first relaxed point is caused by the cell membrane inserted and the second relaxed point is

leaded by the nucleus membrane penetrated [214, 215]. It can be seen that with the increase of the loading force the cell membrane can be punctured and even the nucleus membrane.

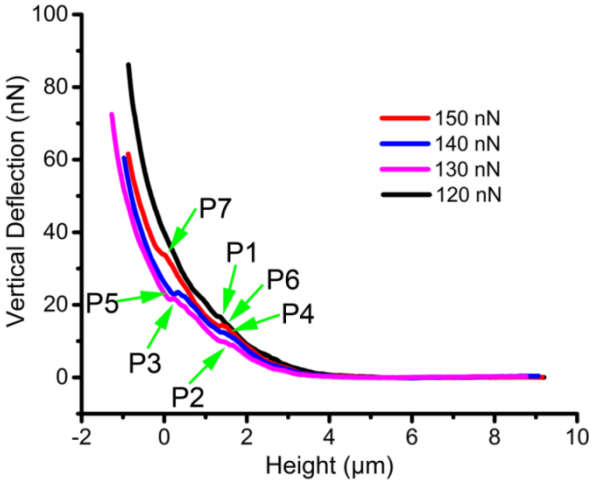

Fig. 6.4 Curves of the magnetic tip inserted into the cell by different loading forces.

The functioned magnetic tip is used to insert into the cells to implant the FITC-MNPs into the target cells and the results are shown in Fig. 6.5. Before observed by the fluorescence microscope, the cultured cells were rinsed by PBS at least 3 times to carry away the particles on the surface of the cells. It can be seen that the FITC-MNPs are released into the cells successfully by observe the fluorescence expression. The targeted cells which are implanted the FITC-MNPs into the cells are labelled by the circles.

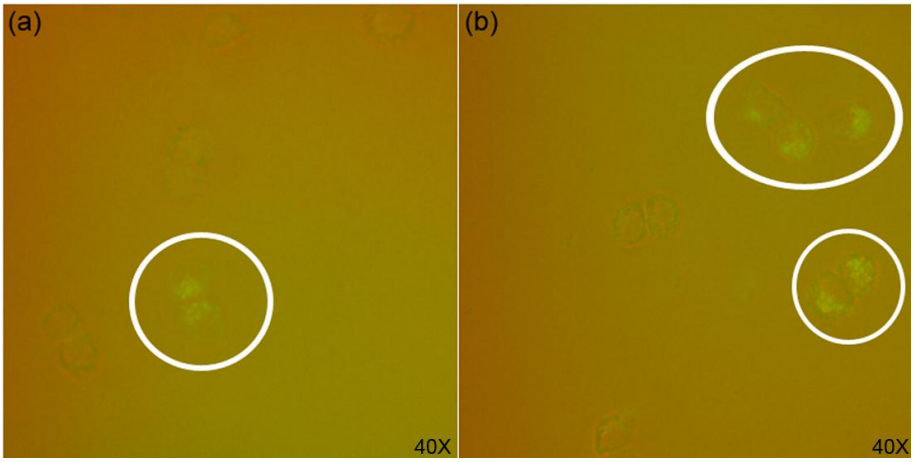

Fig. 6.5 Fluorescence microscope images of the target cells after the injected. The injected cells were labelled by the circles.

The toxicity of MNPs on the cancer cells was assayed by the MTT. The cell viability after the treatment with 50 μg/mL, 100 μg/mL, 200 μg/mL and 500 μg/mL concentrations of the MNPs for 24, 48 and 72 hours are studied, the results as shown in Fig. 6.6. After the 24 hours treatment with MNPs, the cell viability is shown in Fig. 6.6(a). The viability of SMMC-7721 cancer cells treatment with MNPs for 24 hours is 97.9% after the affected by 50 μg/mL, and it is reduce to 91.1% after the treatment with 100 μg/mL, and the cell viabilities are changed to 74.2% and 53.1% after 200 μg/mL and 500 μg/mL MNPs treatment, respectively. After the 48 hours and 72 hours treatments with MNPs, the cell viability is shown in Fig. 6.6(b) and (c).

The viability of HL-7702 cells after treated with MNPs for 24 hours is shown in Fig. 6.6(a). After the treatment with the MNPs concentration of 50 μg/mL, the cell viability is 93.9%. When the concentration of MNPs increased to 100 μg/mL, the cells viability raise to 98.1%. And after the 200 μg/mL and 500 μg/mL MNPs treatment, the cells viabilities decrease to 85.9% and 60.7%, respectively. It can be seen from Fig. 6.6(b) and(c) that the cells viabilities are increased under the concentrations of 100

μg/mL MNPs. However, the viabilities are decreased when the MNPs concentrations larger than 100 μg/mL. Fig. 6.6(d) is the 96-well culture dish after added the drugs of MTT, the culture dish seed with SMMC-7721 and HL-7702 cells and treated with the concentrations of MNPs of 24 hours.

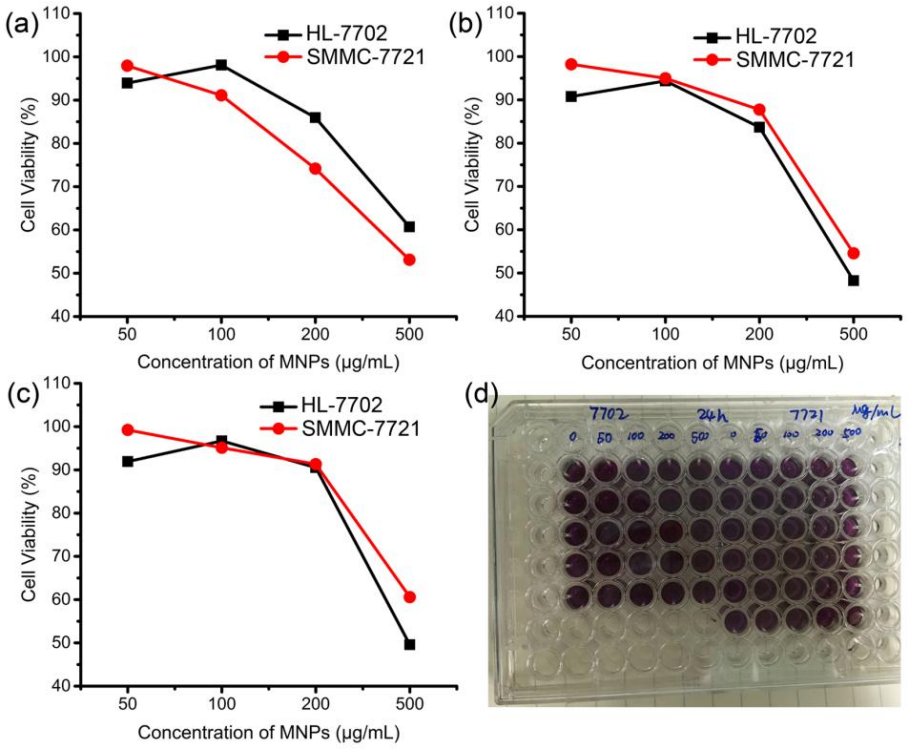

Fig. 6.6 Viabilities of SMCC-7721 cells and HL-7702 cells after treated with different concentrations of MNPs. (a) After 24 hours treatment. (b) After 48 hours treatment. (c) After 72 hours treatment. (d) The 96-well culture dish used for MTT assay.

It indicates that the cell viabilities are reduced with the increase of MNPs concentrations for the SMMC-7721 cancer cells and there is toxicity of the MNPs for the SMMC-7721 cancer cells. However, the cell viabilities are increased under the appropriate MNPs concentrations for the HL-7702 cells and there is nontoxicity of the MNPs for the HL-7702 cells under that concentration. For different cell lines, the MNPs toxicities are different.

6.2 Manipulation of Cell-MNPs with Magnet

6.2.1 Method

Cell-MNPs can be manipulated by external magnetic field. Fig. 6.7 shows cell-MNPs manipulation using a magnet. Before the magnet is applied, cells untreated and treated with MNPs are dispersed freely, as given in Fig. 6.7(a, c). After applying the magnet, the cell-MNPs are concentrated to the magnet because of the attractive force, as shown in Fig. 6.7 (b, d). In the experiments, a permanent magnet with magnet field intensity of 500 mT and diameter of 10 mm was used to affect the cell-MNPs.

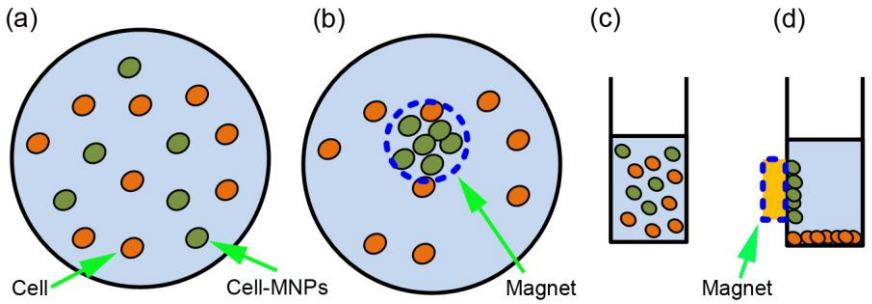

Fig. 6.7 Magnet manipulation of the cell-MNPs. (a) and (c) are cells/cell-MNPs distributes in the culture dish dispersedly. (b) is the result with the effect of a magnet in the horizontal direction. (d) is the result with the effect of a magnet in the vertical direction.

6.2.2 Experiments and Discussions

Human hepatoma cells SMCC-7721 (CBTCCCAS, Shanghai, China) were cultured in the RPMI-1640 media (HyClone) including 10% FBS (HyClone). The cells were maintained in 5% CO_2 at 37 ℃. In the experiments, SMCC-7721 cells without MNPs

treatment and SMCC-7721 cells treated with a concentration of 20 μg/mL MNPs with a diameter of 50 nm were used to manipulate using magnet. The cells treated with MNPs for 12 hours to ensure the cells carried MNPs. They were then treated with pancreatin to separate them from the substrate and make them suspension in the medium to be affected by magnetic force.

The untreated SMCC-7721 cells and those that are treated with MNPs are scanned by MFM, as shown in Fig. 6.8. Fig. 6.8(a) and (b) are the topography and phase shift images of the untreated SMCC-7721 cells. Fig. 6.8(c) and (d) are the topography and phase shift images of the SMCC-7721 cells treated with 20 μg/mL MNPs (50 nm in diameter) for 12 hours. It seems that there are clearly magnetic domains (black dots) distributed on the cells, as shown in Fig. 6.8(d). It concludes that after 12 hours culture of the MNPs together with the cells, MNPs will adhere to the cells surface or swallowed by the cells. In the experiments, the lift height used for MFM imaging was 20 nm.

To study the magnetic manipulation capability along the horizontal directions, a magnet is placed under the culture dish that is set up horizontally, as shown in Fig. 6.9(a). In the experiments, the untreated and treated SMCC-7721 cells were mixed and the magnet was applied for 12 hours. Fig. 6.9(b, c) are cell images taken from the locations with and without magnet, respectively. It can be seen that the cells are gathered to the area where magnet is and the density of the cells in this area is larger than the areas where no magnet is applied. It indicates that the cells after the treated with the MNPs can be manipulated on the horizontal plane by the external magnetic field.

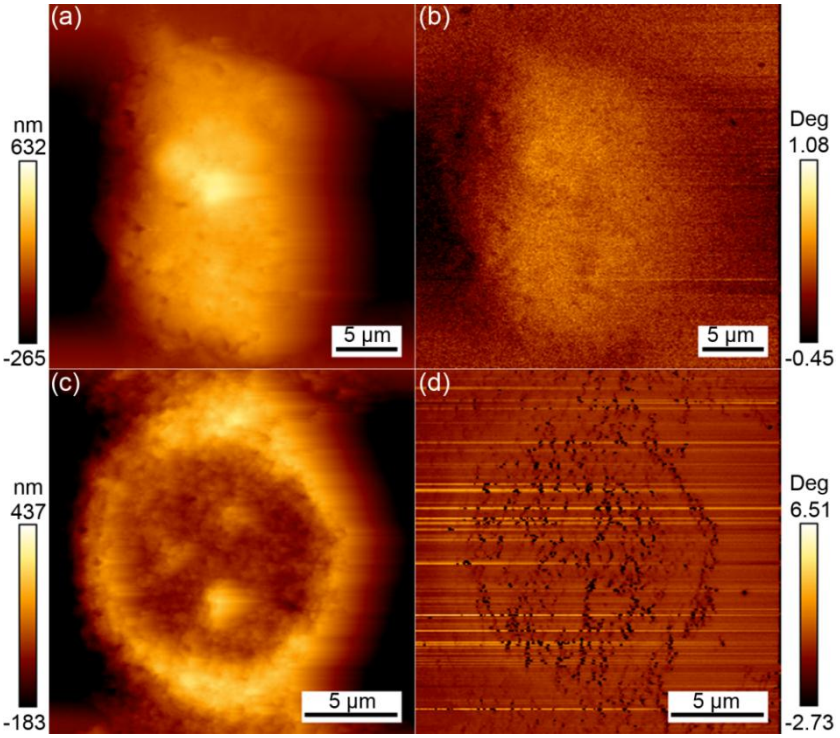

Fig. 6.8 MFM images of SMCC-7721 cells. (a) is the topography image of the SMCC-7721 cell without MNPs and (b) is its corresponding MFM image. (c) is the topography image of the SMCC-7721 cell treated with MNPs and (d) is its corresponding MFM image.

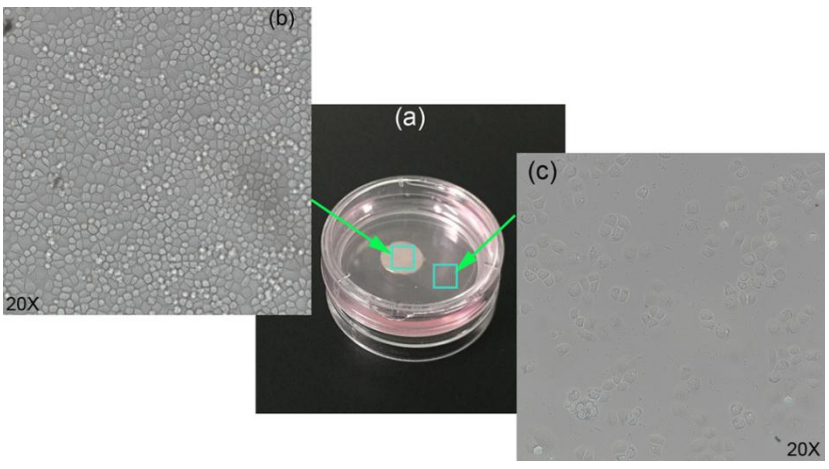

Fig. 6.9 Cells/cell-MNPs in the culture dish affected by a magnet. (a) The culture dish with the effect of magnet. (b) Cell-MNPs distribution of the location under the magnet effects. (c) Cells distribution of the location without the magnet effects.

To study the magnetic manipulation capability along the vertical direction, a magnet is put on the side of the culture dish, as shown in Fig. 6.10(a). In the experiments, the untreated and treated SMCC-7721 cells were mixed and a magnet was applied for 12 hours. The cell-MNPs concentrated to the location where the magnet is and it is labelled by an arrow in Fig. 6.10(b). Fig. 6.10(c) is taken from the bottom of the culture dish and there is no magnet. The cells are randomly and dispersedly distributed in that area. Fig. 6.10(d) shows that because of the magnet cell-MNPs are gathered together and there are a mass of MNPs accumulated (circle labelled). It indicates that cell-MNPs have capability overcome the gravity under the stronger magnetic force affected and they can be manipulated by magnetic force in the vertical direction.

The SMCC-7721 cells treated with MNPs for 12 hours are suspending in the medium and a magnet is added on the side of the culture bottle and cultured the cells erectly, as shown in Fig. 6.11(a). After other 12 hours cultured, the cells gathered to the location where the magnet is, as labelled by the red circle in Fig. 6.11(b). Fig. 6.11(c) shows the result of cell-MNPs after magnet is applied. The MNPs accumulated on the cells surface or inside the cells by the cytophagy. Fig. 6.11(d) shows the results of the bottle bottom location labelled by the green circle. It can be seen that there are only the suspended cells in the medium and without any living cells adhered to the substrate. It indicates that all of the cell-MNPs are attracted to the magnet.

It can be concluded that the cells without MNPs treatment are non-affected by magnet and the cell-MNPs can be influenced by the magnetic force. Thus, MNPs could be used to separate and manipulate the cells using external magnetic fields.

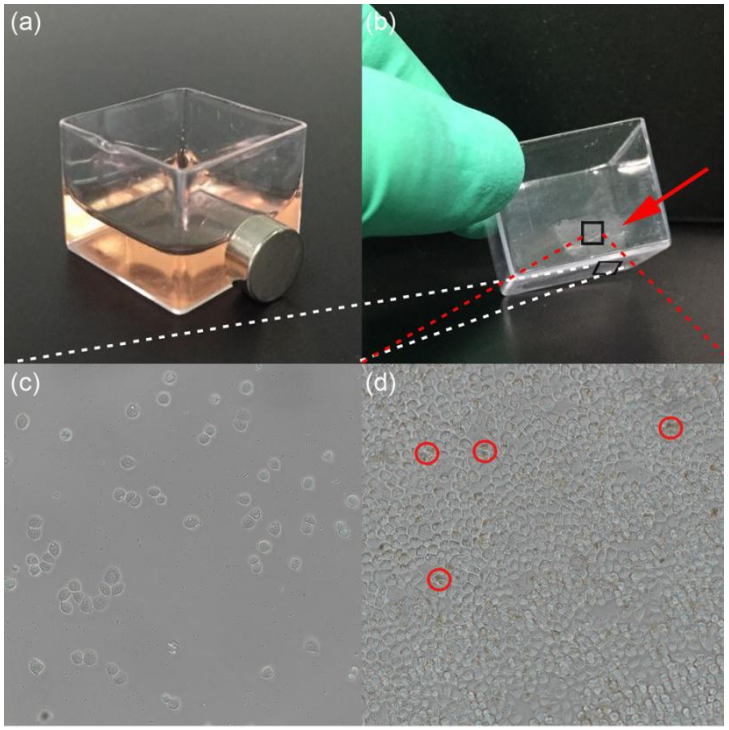

Fig. 6.10 Cells/cell-MNPs in the culture dish and affected by a magnet. (a) A magnet is put on the side of culture dish. (b) Cell-MNPs are concentrated to the location of the magnet affected. (c) Cell distribution of the location without the magnet effects. (d) Cell-MNPs distribution of the location under the magnet effects.

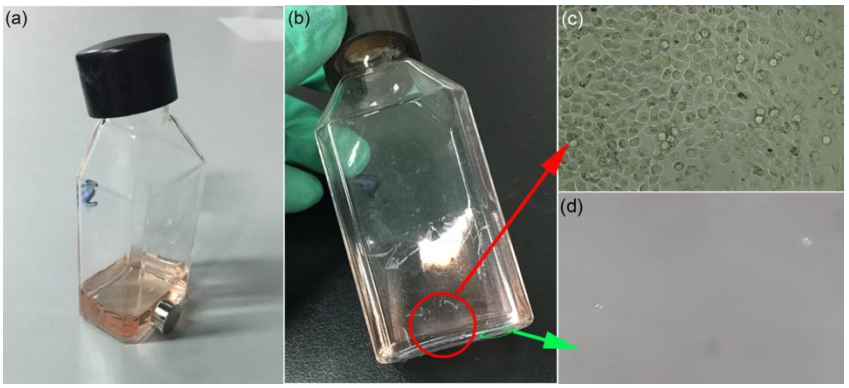

Fig. 6.11 Cell-MNPs in the culture bottle were affected by a magnet. (a) A magnet is put on the side of culture bottle. (b) Cell-MNPs are concentrated to the location of the magnet affected and adhered to the culture bottle. (c) Optical image of cell-MNPs affected by the magnet. (d) Optical image of the location labelled by the green circle.

6.3 Manipulation of the Cell-MNPs by Electromagnet

6.3.1 Method

Fig. 6.12 shows four electromagnets, namely, A, B, C and D, used for the manipulation of the target cell-MNPs in the X and Y directions. The direct current (DC) was used as the electricity supply. Magnetic force in the back direction generated from electromagnet A and the cell-MNPs will be attracted by the magnetic force to the back direction. Magnetic force in the right direction generated from electromagnet B, the cell-MNPs will be attracted by the magnetic force to the right direction. Magnetic force in the front direction generated from electromagnet C, the cell-MNPs will be attracted by the magnetic force to the front direction. Magnetic force in the left direction generated from electromagnet D, the cell-MNPs will be attracted by the magnetic force to the left direction. Accordingly, cell-MNPs can be manipulated by the electromagnet in X and Y directions flexibly by controlling the electricity supplies to those electromagnets.

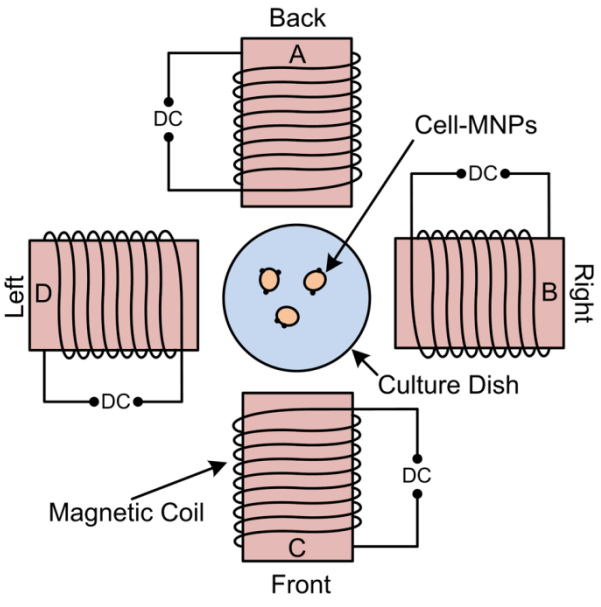

Fig. 6.12 Electromagnet manipulation of the cell-MNPs.

6.3.2 Experiments and Discussions

Yeast cells were cultured for 8 hours before treated with MNPs (Fe_3O_4 MNPs) in a test tube at room temperature. The MNPs with the concentration of 20 μg/mL was used to treat the yeast cells for 12 hours, which ensures good cell viability and the cells to carry enough MNPs before the manipulation experiment. As smaller size MNPs are easy to be swallowed by cells, MNPs with the diameter of 10 nm were used in the experiments to make the yeast cells easy carry or swallow enough MNPs.

To effectively manipulate the cell-MNPs, the gap between the electromagnets and the cell-MNPs must be decided. The following experiments were undertaken for this purpose. An electromagnet was designed as described in the last sub-section, and the electric current of 1 A and voltage of 6.3 V was firstly applied to the electromagnet. The magnetic flux densities (Tesla) are measured using a Teslameter from different distances away the electromagnet, as shown in Fig. 6.13(a). To select the appropriate working distance and current, the electric current of 2 A and voltage of 13.6 V is applied. The magnetic flux densities measured from different distances are shown in Fig. 6.13(b).

It can be seen that with the increase of the distances between the Teslameter and the electromagnet, the magnetic flux density reduces exponentially. It can be seen from Fig. 6.13(a, b) that there are insignificant changes in flux density when the distance larger than 16 mm and hence the distance of 15 mm between the centre of samples and the electromagnetic is selected to successful manipulate the cell-MNPs in the culture dish (culture dish with a radius of 15mm) by electromagnetic. And under the distance of the 15 mm, the magnetizations are measured under differ currents, the

results shown in Fig. 6.13(c). Fig. 6.13(d) is the detector and the electromagnet used to measure the magnetic flux density.

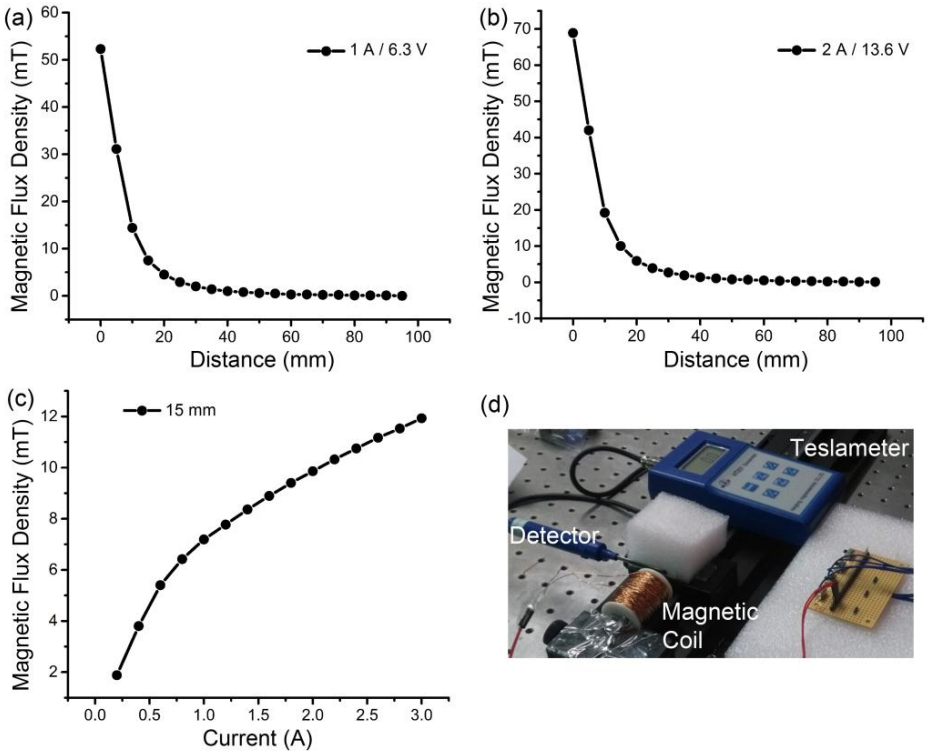

Fig. 6.13 Magnetic flux density of the electromagnet. (a) Obtained with the current of 1 A and voltage of 6.3 V. (b) Obtained with the current of 2 A and voltage of 13.6 V. (c) Obtained at a distance of 15 mm. (d) The instruments used for measuring the magnetic flux density.

Experiments with electric currents ranged in 0.2-3.0A were performed to the range of the current that is able to effectively manipulate cell-MNPs. It was found from optical microscopy results that the cell-MNPs can be flexibly manipulated with the electric current of 1.4-3.0 A under the distance of 15 mm. The trajectories of the cell-MNPs under the electromagnet field with five different electric currents, including 1.4 A, 1.8 A, 2.0 A, 2.3 A and 2.5 A, are shown in Fig. 6.14. Fig. 6.14(a) is the illustration of the experiments and the cell-MNPs' moves along Y-direction with the effect of

electromagnet. Five cell-MNPs were randomly selected from each group and their moving trajectories in 25 seconds were recorded. To easily compare, their trajectories are draw together, as shown in Fig. 6.14(b). It seems that the average migration distance of cell-MNPs under the effect of electromagnet with electric current of 1.4 A is ~60 μm in 25 seconds. Under the effect of electromagnet with electric current of 1.8 A and 2.0 A, the average migration distance of cell-MNPs are ~100 μm and ~140 μm in 25 seconds, respectively. Under the effect of electromagnet with electric current of 2.3 A, the average migration distance of cell-MNPs is ~180 μm in 25 seconds. Under the effect of electromagnet with electric current 2.5 A, the average displacement distance of cell-MNPs is ~320 μm in 25 seconds. It seems that for the same time period, higher speed of cell-MNPs moved under larger electric current.

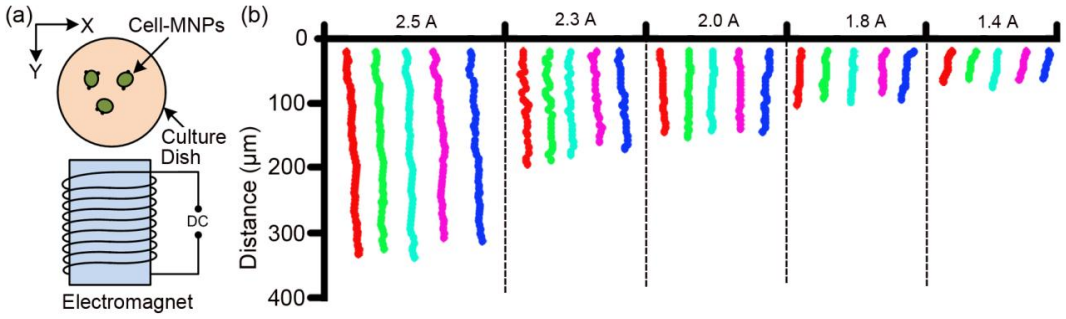

Fig. 6.14 Trajectories of the cell-MNPs under the electromagnet effects.

It was also found that with the electric current larger than 2.2 A, the electromagnetic coil generate heat quickly and this will cause an unsafe experiment. To manipulate the cell-MNPs successfully under a safe environment, the electric current of 2.0 A was selected and the magnetic flux density was 9.86 mT at the distance of 15 mm.

Results of manipulations of the cell-MNPs by the electromagnetics are shown in Fig. 6.15. The moving path of the cell-MNPs is shown in Fig. 6.15(a). The target

cell-MNPs will be manipulated to the left direction (L) from original location (O) first and then to the right location (R). Next the target cell-MNPs is going to the downward direction (D) and finally move to the upward location (U).

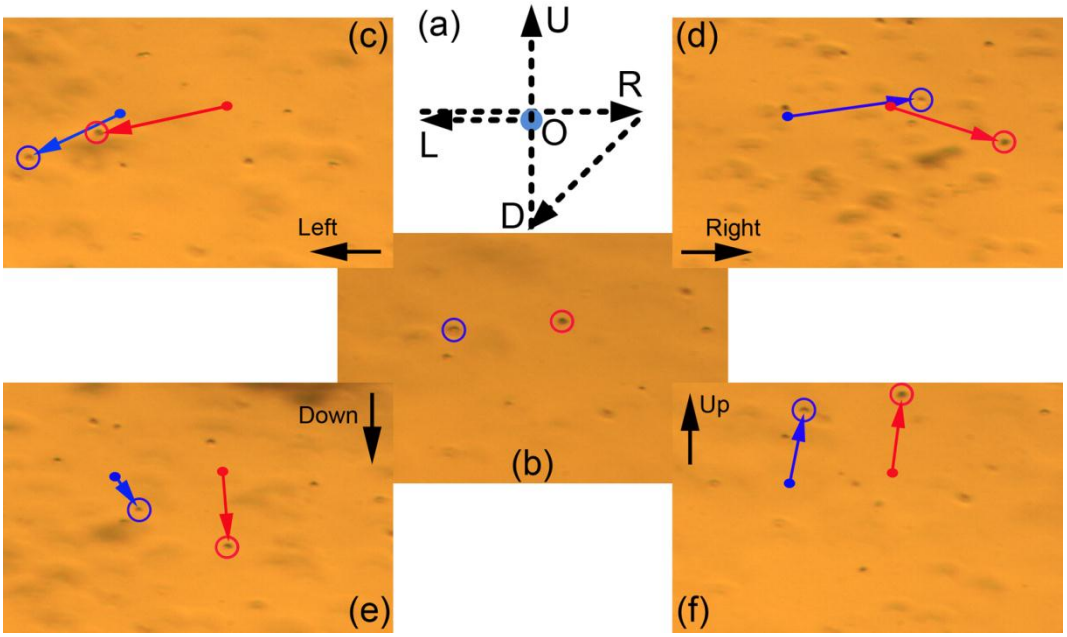

Fig. 6.15 Electromagnetic manipulation of the cell-MNPs. (a) Cell-MNPs moving path. (b) Yeast cells in the environment without the magnetic field. (c) Yeast cells manipulated to the left. (d) Yeast cells manipulated to the right. (e) Yeast cells downward manipulated. (f) Yeast cells upward manipulated.

The original locations of the cells are labelled by circles before the manipulation, as shown in Fig. 6.15(b). The original locations are used as the reference for the manipulation and labelled by points. After the affected by the "Left" electromagnet, the cells are moved to the left side, as shown in Fig. 6.15(c). Then the cells moved from the left side to the right side under the effect of the electromagnetic fields of "Right", as shown in Fig. 6.15(d). Under the combined effect of the electromagnetic fields of "Front" and "Left", the cells moved from right side to the downward side, as shown in Fig. 6.15(e). After the "Back" electromagnetic field affected, the cells

moved to the up side, as shown in Fig. 6.15(f). It shows that the electromagnet can be used to manipulate the cell-MNPs flexibly. This method can manipulate the cell-MNPs to any directions on a plane, cell-MNPs can be moved not only along a straight line but also curve lines with the combined of two neighbouring electromagnets.

6.4 Summary

This chapter firstly implanted FITC-MNPs into the target cancer cells by functioning them onto the magnetic tip surface. The extend curves were studied and found the relaxed points that indicated the tip was successfully inserted into the cell membrane. It clearly seen from the fluorescence microscope images that the fluorescence exhibited and this indicated that the FITC-MNPs were released into the cells successfully. The viabilities of SMCC-7721 and HL-7702 cells after treatment with MNPs were measured to evaluate the toxicity of MNPs. Cell viabilities were reduced with the increase of MNPs concentrations for the SMMC-7721 cancer cells, but there is nontoxicity of the MNPs for the HL-7702 cells under appropriate MNPs concentrations. This work provides guide for target treatment of the cancer cells by MNPs.

Secondly, magnetic force manipulated capability of cell-MNPs was evaluated. SMCC-7721 cancer cells untreated and treated with MNPs were studied by MFM. Clearly magnetic domains were distributed in the cells and indicated that MNPs can adhere to the cells surface or swallowed by the cells. The distribution of SMCC-7721

cancer cells, including cell-MNPs and those that were untreated with MNPs, after affected by magnet were studied in the horizontal and vertical direction and the results indicated that the cell-MNPs concentrated to the position of the magnet affected. It can be concluded that cell-MNPs can be manipulated by the external magnetic field and they can overcome the gravity under the stronger magnetic force. Thus, cell-MNPs can be manipulated by magnetic force in the horizontal and vertical directions.

Finally, controllable electromagnetic magnets were used to manipulate the MNPs treated yeast cells. Four electromagnets used for manipulation of the target cell-MNPs in the X/Y directions. The results shown that cell-MNPs can be handled by controlling these four electromagnets to have the leftward, rightward, upward and downward flexibilities. It indicated that cell-MNPs can be flexibly manipulated to the aimed position by the control of the magnetic forces. This method can be used for the purpose of specific treatment of cancer cells.

CHAPTER 7

CONCLUSIONS AND FUTURE WORK

7.1 Conclusions

The research presented in this thesis focuses on magnetic force imaging and handling of targeted cancer cells on the nanoscale for possible new cancer therapies. This work has demonstrated the accuracy of the proposed new magnetic force imaging technique, the effectiveness of implanting MNPs into the target cells by magnetic probe and the feasibility of manipulating the cell-MNPs with magnetic force. This work forms a part of foundation from engineering perspective for research in new cancer therapies at cell level. The innovative parts of this work are highlighted in the followings:

- MFM imaging quality improvement – A method of differentiating MFM imaging by magnetic probe magnetized upward and downward was developed. The image contrast and SNR of the obtained differential image were significantly improved. Three different scanning directions with the angles of $0°$, $45°$ and $90°$ were used to measure the magnetic domain structures distributions of magnetic sample, and a distortion compensation method was used to improve the accuracy of the MFM images. With this compensation method, the distortion structures were corrected and the effect of scanning directions on the MFM imaging was significantly reduced.

- MNPs picking up and releasing – A helical curve was designed as the capture

path for MFM probe to follow and to pick up target MNPs. Compared with pushing and sliding methods, this proposed method was able to pick up and to move MNPs of the diameters of 10~90 nm with the success rate over 90%. A BOPP film together with an external magnetic field was used for releasing MNPs from MFM probe tips. The magnetic tip was manipulated to push into the BOPP film with a depth of 50-100 nm under a magnetic field and hold for 5 seconds. The experimental results have shown that this method was effective for the separation of MNPs from MFM probes. These two methods enable the flexible manipulation of MNPs.

- Identification of differences in morphological features and mechanical properties between multinuclear and mononuclear cancer cells – Morphological features (height, length, width and roughness) and mechanical properties (adhesive force and Young's modulus) of mononuclear and multinuclear SW480 cells after treating with fullerenol were studied. The results indicated that the mononuclear SW480 cells were more sensitive to fullerenol than the multinuclear SW480 cells, and the multinuclear SW480 cells exhibited a stronger drug-resistance than the mononuclear SW480 cells. This work provides a recommendation of selecting multinuclear cells as the target cells for the purpose of MNPs-based cancer treatment investigation.

- MNPs implantation and cell-MNPs manipulation – FITC-MNPs were functioned onto the magnetic tip surface and implanted them into the target cancer cells by inserted the tip into the cells. Fluorescence microscope images indicated that the FITC-MNPs were released into the cells successfully. This provides a guide for target treatment of the cancer cells by MNPs. Magnet was used to evaluate the

magnetic force manipulated capability of cell-MNPs and results found that cell-MNPs can be manipulated by magnet in the horizontal and vertical directions. Controllable electromagnetic magnets in four directions were used to flexibly manipulate cell-MNPs and the results found that the cell-MNPs can be handled to have the leftward, rightward, upward and downward flexibilities. It indicates that cell-MNPs can be flexibly manipulated to the aimed position by the control of the magnetic forces. This method can be used for the purpose of specific treatment of cancer cells.

7.2 Future Work

The work presented in the thesis has attained a number of significant achievements in the fields of magnetic force imaging and MNPs handling, which have the potential for new cancer therapies. The following issues may need to be further explored.

- Imaging and manipulation of MNPs by MFM in liquid environments – Although MFM imaging improved techniques and MNPs manipulation methods have been developed in Chapters 3 and 4, there are still challenges in imaging and handling MNPs in liquid environments because the hydration forces resist the oscillation of the cantilever and make the low magnetic forces between the magnetic probe and the MNPs hard to be detected. Thus, a further investigation into MFM imaging and manipulation techniques to successfully obtain the MNPs distributions in liquid environments and manipulate the target MNPs in liquid environments is needed.

- Techniques to separate the multinuclear cells from mononuclear cells to specific treatment of the multinuclear cells – As it was mentioned in Chapter 5, mononuclear SW480 cells were more sensitive than multinuclear SW480 cells and multinuclear SW480 cells exhibited stronger drug-resistance than mononuclear SW480 cells. This means that multinuclear cells are more likely to survive from the anti-cancer drug and they are difficult to be killed in the cancer treatment. Thus, techniques that can label multinuclear cells and to separate them from mononuclear ones are needed.

- Techniques for target cancer cells treatment and manipulation in large scale – In Chapter 6, the target cells were successfully treated with MNPs by implanted MNPs into the cells using the MFM tip. This means that functioned MNPs need to be injected into each target cell using the magnetic tip. In large scales where there are a large number of cancer cells, the implantation will take a longer time period with the current manual method. To improve the efficiency, automation techniques which can identify and label target cancer cells, and can implant MNPs into multiple cells simultaneously and automatically are needed.

REFERENCES

[1] A. Akbarzadeh, M. Samiei and S. Davaran. (2012) Magnetic nanoparticles: preparation, physical properties, and applications in biomedicine. *Nanoscale Reseach Letters*, 7, 144.

[2] Y. Cheng, R. A. Morshed, B. Auffinger, A. L. Tobias and M. S. Lesniak. (2014) Multifunctional nanoparticles for brain tumor imaging and therapy. *Advanced Drug Delivery Reviews*, 66, 42-57.

[3] R. Lin, Y. Li, T. MacDonald, H. Wu, J. Provenzale, X. Peng, J. Huang, L. Wang, A. Y. Wang, J. Yang and H. Mao. (2017) Improving sensitivity and specificity of capturing and detecting targeted cancer cells with anti-biofouling polymer coated magnetic iron oxide nanoparticles. *Colloids and Surfaces B: Biointerfaces*, 150, 261-270.

[4] U. Sang Shin, J. W. Seo, B. Kundu, H. W. Kim and M. Eltohamy. (2017) Super-magnetic smart hybrid doxorubicin loaded nanoparticles effectively target breast adenocarcinoma cells. *Microporous and Mesoporous Materials*, 243, 206-213.

[5] A. Latorre, P. Couleaud, A. Aires, A. L. Cortajarena and A. Somoza. (2014) Multifunctionalization of magnetic nanoparticles for controlled drug release: a general approach. *European Journal of Medicinal Chemistry*, 82, 355-362.

[6] A. K. Hoshiar, T. A. Le, F. U. Amin, M. O. Kim and J. Yoon. (2017) Studies of aggregated nanoparticles steering during magnetic-guided drug delivery in the blood vessels. *Journal of Magnetism and Magnetic Materials*, 427, 181-187.

[7] F. Mouffouk, T. Simão, D. F. Dornelles, A. D. Lopes, P. Sau, J. Martins, K. M. Abu-Salah, S. A. Alrokayan, A. M. Rosa da Costa and N. R. dos Santos. (2015) Self-assembled polymeric nanoparticles as new, smart contrast agents for cancer early detection using magnetic resonance imaging. *International Journal of Nanomededicine*, 10, 63-76.

[8] J. Mosafer, K. Abnous, M. Tafaghodi, A. Mokhtarzadeh and M. Ramezani. (2017) In vitro and in vivo evaluation of anti-nucleolin-targeted magnetic PLGA nanoparticles loaded with doxorubicin as a theranostic agent for enhanced targeted cancer imaging and therapy. *European Journal of Pharmaceutics and Biopharmaceutics*, 113, 60-74.

[9] F. Wakaya, M. Kajiwara, K. Kubo, S. Abo and M. Takai. (2011) Improvement of current sensitivity in detecting current-induced magnetic field using magnetic force microscopy. *Microelectronic Engineering*, 88, 2778-2780.

[10] S. M. Watson, H. D. Mohamed, B. R. Horrocks and A. Houlton. (2013) Electrically conductive magnetic nanowires using an electrochemical DNA-templating route. *Nanoscale*, 5, 5349-5359.

[11] H. D. Mohamed, S. M. Watson, B. R. Horrocks and A. Houlton. (2012) Magnetic and conductive magnetite nanowires by DNA-templating. *Nanoscale*, 4, 5936-5945.

[12] G. Lorusso, M. Jenkins, P. Gonzalez-Monje, A. Arauzo, J. Sese, D. Ruiz-Molina, O. Roubeau and M. Evangelisti. (2013) Surface-confined molecular coolers for cryogenics. *Advanced Materials*, 25, 2984-2988.

[13] N. Domingo, E. Bellido and D. Ruiz-Molina. (2012) Advances on structuring, integration and magnetic characterization of molecular nanomagnets on surfaces and devices. *Chemical Society Reviews*, 41, 258-302.

[14] Y. Amemiya, T. Tanaka, B. Yoza and T. Matsunaga. (2005) Novel detection system for biomolecules using nano-sized bacterial magnetic particles and magnetic force microscopy. *Journal of Biotechnology*, 120, 308-314.

[15] F. Z. Leandro, J. Martins, A. M. Fontes and A. C. Tedesco. (2017) Evaluation of theranostic nanocarriers for near-infrared imaging and photodynamic therapy on human prostate cancer cells. *Colloids and Surfaces B: Biointerfaces*, 154, 341-349.

[16] R. P. Jones, S. Hamann, H. Z. Malik, S. W. Fenwick, G. J. Poston and G.

Folprecht. (2014) Defined criteria for resectability improves rates of secondary resection after systemic therapy for liver limited metastatic colorectal cancer. *European Journal of Cancer*, 50, 1590-1601.

[17] A. P. Sokolenko, E. L. Savonevich, A. O. Ivantsov, G. A. Raskin, E. S. Kuligina, T. V. Gorodnova, E. V. Preobrazhenskaya, M. A. Kleshchov, V. I. Tiurin, M. S. Mukhina, K. B. Kotiv, A. V. Shulga, S. G. Kuznetsov, I. V. Berlev and E. N. Imyanitov. (2017) Rapid selection of BRCA1-proficient tumor cells during neoadjuvant therapy for ovarian cancer in BRCA1 mutation carriers. *Cancer Letters*, 397, 127-132.

[18] Y. Minegishi, N. Kokuho, Y. Miura, M. Matsumoto, A. Miyanaga, R. Noro, Y. Saito, M. Seike, K. Kubota, A. Azuma, K. Kida and A. Gemma. (2014) Clinical features, anti-cancer treatments and outcomes of lung cancer patients with combined pulmonary fibrosis and emphysema. *Lung Cancer*, 85, 258-263.

[19] X. Hou, H. Zhou, L. Wang, J. Tang, C. Chen, G. Jiang and Y. Liu. (2017) Multifunctional near-infrared dye-magnetic nanoparticles for bioimaging and cancer therapy. *Cancer Letters*, 390, 168-175.

[20] A. Körnig, M. A. Hartmann, C. Teichert, P. Fratzl and D. Faivre. (2014) Magnetic force imaging of a chain of biogenic magnetite and Monte Carlo analysis of tip-particle interaction. *Journal of Physics D: Applied Physics*, 47, 235403.

[21] A. Hubert, W. Rave and S. L. Tomlinson. (1997) Imaging magnetic charges with magnetic force microscopy. *Physica Status Solidi (B)*, 204, 12.

[22] G. Binning, H. Rohrer, C. Gerber and E. Weibel. (1982) Surface studies by scanning tunneling microscopy. *Physical Review Letters*, 49, 5.

[23] G. Binnig, C. F. Quate and C. Gerber. (1986) Atomic force microscope. *Physical Review Letters*, 56, 930-933.

[24] A. Schwarz and R. Wiesendanger. (2008) Magnetic sensitive force microscopy.

Nano Today, 3, 28-39.

[25] G. V. K. Kishore, A. Kumar, G. Chakraborty, S. K. Albert, B. P. C. Rao, A. K. Bhaduri and T. Jayakumar. (2015) Study of magnetism in Ni–Cr hardface alloy deposit on 316LN stainless steel using magnetic force microscopy. *Journal of Magnetism and Magnetic Materials*, 385, 112-118.

[26] V. Cambel, P. Eliáš, D. Gregušová, J. Fedor, J. Martaus, G. Karapetrov, V. Novosad and I. Kostič. (2010) Novel magnetic tips developed for the switching magnetization magnetic force microscopy. *Journal of Nanoscience and Nanotechnology*, 10, 4477-4481.

[27] M. Precner, J. Fedor, J. Soltys and V. Cambel. (2015) Dual-tip magnetic force microscopy with suppressed influence on magnetically soft samples. *Nanotechnology*, 26, 055304.

[28] V. Cambel, P. Eliáš, D. Gregušová, J. Martaus, J. Fedor, G. Karapetrov and V. Novosad. (2010) Magnetic elements for switching magnetization magnetic force microscopy tips. *Journal of Magnetism and Magnetic Materials*, 322, 2715-2721.

[29] C. Dietz, E. T. Herruzo, J. R. Lozano and R. Garcia. (2011) Nanomechanical coupling enables detection and imaging of 5 nm superparamagnetic particles in liquid. *Nanotechnology*, 22, 125708.

[30] A. Alekseev, A. Popkov, A. Shubin, F. Pudonin and N. Djuzhev. (2014) Effect of horizontal magnetization reversal of the tips on magnetic force microscopy images. *Ultramicroscopy*, 136, 91-95.

[31] A. Chiolerio and P. Allia. (2012) Towards a quantitative analysis of magnetic force microscopy data matrices. *Journal of Magnetism and Magnetic Materials*, 324, 2416-2428.

[32] P. Lambert and S. Régnier. (2006) Surface and contact forces models within the framework of microassembly. *Journal of Micromechatronics*, 3, 123-157.

[33] H. Xie, C. Onal, S. Régnier and M. Sitti. (2011) Atomic force microscopy

based nanorobotics. *Springer Tracts in Advanced Robotics*, 71, DOI 10.1007/1978-1003-1642-20329-20329.

[34] D. Rugar, H. J. Mamin, P. Guethner, S. E. Lambert, J. E. Stern, I. McFadyen and T. Yogi. (1990) Magnetic force microscopy: General principles and application to longitudinal recording media. *Journal of Applied Physics*, 68, 1169.

[35] D. Passeri, C. Dong, L. Angeloni, F. Pantanella, T. Natalizi, F. Berlutti, C. Marianecci, F. Ciccarello and M. Rossi. (2014) Thickness measurement of soft thin films on periodically patterned magnetic substrates by phase difference magnetic force microscopy. *Ultramicroscopy*, 136, 96-106.

[36] S. Takaya, T. Suzuki, Y. Matsumoto, K. Demachi and M. Uesaka. (2004) Estimation of stress corrosion cracking sensitivity of type 304 stainless steel by magnetic force microscope. *Journal of Nuclear Materials*, 327, 19-26.

[37] R. Engel-Herbert, D. M. Schaadt and T. Hesjedal. (2006) Analytical and numerical calculations of the magnetic force microscopy response: A comparison. *Journal of Applied Physics*, 99, 113905.

[38] Y. Martin and H. K. Wickramasinghe. (1987) Magnetic imaging by force microscopy with 1000 A resolution. *Applied Physics Letters*, 5, 1455-1457.

[39] P. Grütter. (1995) Applications of Magnetic Force Microscopy. *Forces in Scanning Probe Methods*, 447-470.

[40] D. Baronov and S. B. Andersson. (2010) Controlling a magnetic force microscope to track a magnetized nanosize particle. *IEEE Transactions on Nanotechnology*, 9, 367-374.

[41] D. Baronov and S. B. Andersson. (2008) Tracking a magnetic nanoparticle in 3-D with a magnetic force microscope. *In Proceedings of the 47th IEEE Conference on Decision and Control (CDC)*, Cancun, Mexico, 5170-5175.

[42] P. Grütter, D. Rugar and H. J. Mamin. (1992) Magnetic force microscopy of magnetic materials. *Ultramicroscopy*, 47, 393-399.

[43] S. Bhattacharjee, M. Elimelech and M. Borkovec. (1998) DLVO interaction between colloidal particles: beyond Derjaguin's approximation. *Croatica Chemica Acta*, 71(4), 883-903.

[44] A. Marmur. (1993) Tip-surface capillary interactions. *Langmuir: the ACS Journal of Surfaces and Colloids*, 9, 1922-1926.

[45] Y. Rollot, S. Régnier and J. C. Guinot. (1999) Simulation of micro-manipulations: adhesion forces and specific dynamic models. *International Journal of Adhesion and Adhesives*, 19, 35-48.

[46] S. Belaidi, P. Girard and G. Leveque. (1997) Electrostatic forces acting on the tip in atomic force microscopy: modelization and comparison with analytic expressions. *Journal of Applied Physics*, 81, 1023-1030.

[47] C. Dey, K. Baishya, A. Ghosh, M. M. Goswami, A. Ghosh and K. Mandal. (2017) Improvement of drug delivery by hyperthermia treatment using magnetic cubic cobalt ferrite nanoparticles. *Journal of Magnetism and Magnetic Materials*, 427, 168-174.

[48] M. Iv, N. Telischak, D. Feng, S. J. Holdsworth, K. W. Yeom and H. E. Daldrup-Link. (2015) Clinical applications of iron oxide nanoparticles for magnetic resonance imaging of brain tumors. *Nanomedicine*, 10, 993-1018.

[49] H. J. Hathaway, K. S. Butler, N. L. Adolphi, D. M. Lovato, R. Belfon, D. Fegan, T. C. Monson, J. E. Trujillo, T. E. Tessier, H. C. Bryant, D. L. Huber, R. S. Larson and E. R. Flynn. (2011) Detection of breast cancer cells using targeted magnetic nanoparticles and ultra-sensitive magnetic field sensors. *Breast Cancer Research*, 13, R108.

[50] R. Barbucci, G. Giani, S. Fedi, S. Bottari and M. Casolaro. (2012) Biohydrogels with magnetic nanoparticles as crosslinker: characteristics and potential use for controlled antitumor drug-delivery. *Acta Biomaterialia*, 8, 4244-4252.

[51] M. Arruebo, R. Fernández-Pacheco, M. R. Ibarra and J. Santamaría. (2007)

Magnetic nanoparticles for drug delivery. *Nano Today*, 2, 22-32.

[52] N. Taghavi Pourianazar and U. Gunduz. (2016) Changes in apoptosis-related gene expression and cytokine release in breast cancer cells treated with CpG-loaded magnetic PAMAM nanoparticles. *International Journal of Pharmaceutics*, 515, 11-19.

[53] M. Timko, M. KonerackáP, P. Kopčanský, C. N. Ramchand, L. Vékas and D. Bica. (2004) Application of magnetizable complex systems in biomedicine. *Czechoslovak Journal of Physics*, 54, 599-606.

[54] V. P. Torchilin. (2005) Recent advances with liposomes as pharmaceutical carriers. *Nature Reviews Drug Discovery*, 4, 145-160.

[55] J. Q. Zhang, Z. R. Zhang, H. Yang, Q. Y. Tan, S. R. Qin and X. L. Qiu. (2005) Lyophilized paclitaxel magnetoliposomes as a potential drug delivery system for breast carcinoma via parenteral administration: in vitro and in vivo studies. *Pharmaceutical Research*, 22, 573-583.

[56] J. Zhang and R. D. K. Misra. (2007) Magnetic drug-targeting carrier encapsulated with thermosensitive smart polymer: core–shell nanoparticle carrier and drug release response. *Acta Biomaterialia*, 3, 838-850.

[57] X. Chao, Z. Zhang, L. Guo, J. Zhu, M. Peng, A. J. Vermorken, W. J. Van de Ven, C. Chen and Y. Cui. (2012) A novel magnetic nanoparticle drug carrier for enhanced cancer chemotherapy. *PloS One*, 7, e40388.

[58] N. K. Verma, K. Crosbie-Staunton, A. Satti, S. Gallagher, K. B. Ryan, T. Doody, C. McAtamney, R. MacLoughlin, P. Galvin, C. S. Burke, Y. Volkov and Y. K. Gun'ko. (2013) Magnetic core-shell nanoparticles for drug delivery by nebulization. *Journal of Nanobiotechnology*, 11, 12.

[59] A. Tadayon, R. Jamshidi and A. Esmaeili. (2015) Delivery of tissue plasminogen activator and streptokinase magnetic nanoparticles to target vascular diseases. *International Journal of Pharmaceutics*, 495, 428-438.

[60] R. Tarasi, M. Khoobi, H. Niknejad, A. Ramazani, L. Ma'mani, S.

Bahadorikhalili and A. Shafiee. (2016) *β*-cyclodextrin functionalized poly (5-amidoisophthalicacid) grafted Fe_3O_4 magnetic nanoparticles: A novel biocompatible nanocomposite for targeted docetaxel delivery. *Journal of Magnetism and Magnetic Materials*, 417, 451-459.

[61] A. K. A. Silva, C. Wilhelm, J. Kolosnjaj-Tabi, N. Luciani and F. Gazeau. (2012) Cellular transfer of magnetic nanoparticles via cell microvesicles: impact on cell tracking by magnetic resonance imaging. *Pharmaceutical Research*, 29, 1392-1403.

[62] T. K. Jain, S. P. Foy, B. Erokwu, S. Dimitrijevic, C. A. Flask and V. Labhasetwar. (2009) Magnetic resonance imaging of multifunctional pluronic stabilized iron-oxide nanoparticles in tumor-bearing mice. *Biomaterials*, 30, 6748-6756.

[63] O. Veiseh, J. W. Gunn and M. Zhang. (2010) Design and fabrication of magnetic nanoparticles for targeted drug delivery and imaging. *Advanced Drug Delivery Reviews*, 62, 284-304.

[64] P. Ferguson, K. Feindel, A. Slocombe, M. MacKay, T. Wignall, B. Delahunt, R. D. Tilley and I. F. Hermans. (2013) Strongly magnetic iron nanoparticles improve the diagnosis of small tumours in the reticuloendothelial system by magnetic resonance imaging. *Plos One*, 8, e56572.

[65] A. Ito, M. Shinkai, H. Honda and T. Kobayashi. (2005) Medical application of functionalized magnetic nanoparticles. *Journal of Bioscience and Bioengineering*, 100, 1-11.

[66] G. Bierry, F. Jehl, A. Neuville, S. Lefevre, P. Robert, S. Kremer and J. L. Dietemann. (2010) MRI of macrophages in infectious knee synovitis. *American Journal of Roentgenology*, 194, W521-W526.

[67] H. Baraki, N. Zinne, D. Wedekind, M. Meier, A. Bleich, S. Glage, H. J. Hedrich, I. Kutschka and A. Haverich. (2012) Magnetic resonance imaging of soft tissue infection with iron oxide labeled granulocytes in a rat model. *PloS One*, 7, e51770.

[68] N. Chen, C. Shao, S. Li, Z. Wang, Y. Qu, W. Gu, C. Yu and L. Ye. (2015) Cy5.5 conjugated MnO nanoparticles for magnetic resonance/near-infrared fluorescence dual-modal imaging of brain gliomas. *Journal of Colloid and Interface Science*, 457, 27-34.

[69] M. K. Trivedi, A. Branton, D. Trivedi, G. Nayak, R. K. Mishra and S. Jana. (2015) Characterization of physicochemical and thermal properties of treated ethyl cellulose and methyl cellulose. *International Journal of Biomedical Materials Research*, 3, 83-91.

[70] M. Shahrousvand, M. S. Hoseinian, M. Ghollasi, A. Karbalaeimahdi, A. Salimi and F. A. Tabar. (2017) Flexible magnetic polyurethane/Fe2O3 nanoparticles as organic-inorganic nanocomposites for biomedical applications: Properties and cell behavior. *Materials Science and Engineering C*, 74, 556-567.

[71] M. Ishii, R. Shibata, Y. Numaguchi, T. Kito, H. Suzuki, K. Shimizu, A. Ito, H. Honda and T. Murohara. (2011) Enhanced angiogenesis by transplantation of mesenchymal stem cell sheet created by a novel magnetic tissue engineering method. *Arteriosclerosis, Thrombosis, and Vascular Biology*, 31, 2210-2215.

[72] A. Ito, Y. Takizawa, H. Honda, K. Hata, H. Kagami, M. Ueda and T. Kobayashi. (2004) Tissue engineering using magnetite nanoparticles and magnetic force: heterotypic layers of cocultured hepatocytes and endothelial cells. *Tissue Engineering*, 10, 833-840.

[73] N. Bock, A. Riminucci, C. Dionigi, A. Russo, A. Tampieri, E. Landi, V. A. Goranov, M. Marcacci and V. Dediu. (2010) A novel route in bone tissue engineering: magnetic biomimetic scaffolds. *Acta Biomaterialia*, 6, 786-796.

[74] A. Ito, K. Ino, M. Hayashida, T. Kobayashi, H. Matsunuma, H. Kagami, M. Ueda and H. Honda. (2005) Novel methodology for fabrication of tissue-engineered tubular constructs using magnetite nanoparticles and magnetic force. *Tissue Engineering*, 11, 1553-1561.

[75] S. Oshima, M. Ishikawa, Y. Mochizuki, T. Kobayashi, Y. Yasunaga and M.

Ochi. (2010) Enhancement of bone formation in an experimental bony defect using ferumoxidelabelled mesenchymal stromal cells and a magnetic targeting system. *The Bone & Joint Journal (JBJS)*, 92, 1606-1613.

[76] T. Kobayashi, M. Ochi, S. Yanada, M. Ishikawa, N. Adachi, M. Deie and K. Arihiro. (2008) A novel cell delivery system using magnetically labeled mesenchymal stem cells and an external magnetic device for clinical cartilage repair. *Arthroscopy: the journal of arthroscopic & related surgery: official publication of the Arthroscopy Association of North America and the International Arthroscopy Association*, 24, 69-76.

[77] T. Kobayashi, M. Ochi, S. Yanada, M. Ishikawa, N. Adachi, M. Deie and K. Arihiro. (2009) Augmentation of degenerated human cartilage in vitro using magnetically labeled mesenchymal stem cells and an external magnetic device. *Arthroscopy: the journal of arthroscopic & related surgery: official publication of the Arthroscopy Association of North America and the International Arthroscopy Association*, 25, 1435-1441.

[78] K. Shimizu, A. Ito, M. Arinobe, Y. Murase, Y. Iwata, Y. Narita, H. Kagami, M. Ueda and H. Honda. (2007) Effective cell-seeding technique using magnetite nanoparticles and magnetic force onto decellularized blood vessels for vascular tissue engineering. *Journal of Bioscience and Bioengineering*, 103, 472-478.

[79] T. Sasaki, N. Iwasaki, K. Kohno, M. Kishimoto, T. Majima, S. Nishimura and A. Minami. (2008) Magnetic nanoparticles for improving cell invasion in tissue engineering. *Journal of Biomedical Materials Research Part A*, 86, 969-978.

[80] Y. K. Fang, W. Li, W. Sun, M. G. Zhu, Z. H. Guo and B. S. Han. (2013) Revealing of magnetic domains of strong bulk anisotropic permanent magnets via magnetic force microscopy. *Journal of Magnetism and Magnetic Materials*, 345, 176-179.

[81] M. V. Zhukov, K. I. Belousov, A. M. Mozharov, I. S. Mukhin and A. O.

Golubok. (2015) Specialized probes with nanowhisker structures for high resolution magnetic force microscopy. *Journal of Physics: Conference Series*, 643, 012095.

[82] R. Wiesendanger, I. V. Shvets, D. Burgler, G. Tarrach, H. J. Guntherodt and J. M. D. Coey. (1992) Magnetic imaging at the atomic level. *Zeitschrift für Physik B Condensed Matter*, 86, 1-2.

[83] L. Batista, U. Rabe and S. Hirsekorn. (2014) Determination of the easy axes of small ferromagnetic precipitates in a bulk material by combined magnetic force microscopy and electron backscatter diffraction techniques. *Ultramicroscopy*, 146, 17-26.

[84] T. M. Nocera, Y. Zeng and G. Agarwal. (2014) Distinguishing ferritin from apoferritin using magnetic force microscopy. *Nanotechnology*, 25, 461001.

[85] M. Zhu, Y. Fang, Y. Guo, W. Li and B. Han. (2004) Study of magnetic microstructures of Nd-Fe-B casting strips by using magnetic force microscope. *Journal of Magnetism and Magnetic Materials*, 282, 180-185.

[86] M. Gavagnin, H. D. Wanzenboeck, D. Belic, M. M. Shawrav, A. Persson, K. Gunnarsson, P. Svedlindh and E. Bertagnolli. (2014) Magnetic force microscopy study of shape engineered FEBID iron nanostructures. *Physica Status Solidi (A)*, 211, 368-374.

[87] A. Sharma, S. Mohan and S. Suwas. (2016) The influence of deposition temperature on the structure, microstructure, morphology and magnetic properties of sputter deposited nickel thin films. *Thin Solid Films*, 619, 91-101.

[88] I. A. Mahdy. (2017) Magnetic performance of orthorhombic Mn35Ge35Te30 nanocrystals. *Journal of Magnetism and Magnetic Materials*, 422, 77-83.

[89] V. Karoutsos, P. Poulopoulos, V. Kapaklis, S. D. Pappas, D. Trachylis and C. Politis. (2010) Magnetic Force Microscopy on Nanocrystalline Co Films. *Journal of Nanoscience and Nanotechnology*, 10, 6120-6127.

[90] V. L. Mironov, B. A. Gribkov, A. A. Fraerman, S. A. Gusev, S. N. Vdovichev, I. R. Karetnikova, I. M. Nefedov and I. A. Shereshevsky. (2007) MFM probe control of magnetic vortex chirality in elliptical Co nanoparticles. *Journal of Magnetism and Magnetic Materials*, 312, 153-157.

[91] E. Pinilla-Cienfuegos, S. Kumar, S. Mañas-Valero, J. Canet-Ferrer, L. Catala, T. Mallah, A. Forment-Aliaga and E. Coronado. (2015) Imaging the magnetic reversal of isolated and organized molecular-based nanoparticles using magnetic force microscopy. *Particle & Particle Systems Characterization*, 32, 693-700.

[92] A. Kumar, D. K. Avasthi, J. C. Pivin, R. M. Papaléo, A. Tripathi, F. Singh and I. Sulania. (2007) Magnetic force microscopy of nano-size magnetic domain ordering in heavy ion irradiated fullerene films. *Journal of Nanoscience and Nanotechnology*, 7, 2201-2205.

[93] E. E. Flater, G. E. Zacharakis-Jutz, B. G. Dumba, I. A. White and C. A. Clifford. (2014) Towards easy and reliable AFM tip shape determination using blind tip reconstruction. *Ultramicroscopy*, 146, 130-143.

[94] D. J. Keller and F. S. Franke. (1993) Envelope reconstruction of probe microscope images. *Surface Science*, 294, 409-419.

[95] M. R. Koblischka, U. Hartmann and T. Sulzbach. (2003) Improvements of the lateral resolution of the MFM technique. *Thin Solid Films*, 428, 93-97.

[96] U. Memmert, A. N. Muller and U. Hartmann. (2000) Probes for magnetic force microscopy imaging of soft magnetic samples. *Measurement Science and Technology*, 11, 1342-1347.

[97] M. R. Koblischka, U. Hartmann and T. Sulzbach. (2004) Improving the lateral resolution of the MFM technique to the 10 nm range. *Journal of Magnetism and Magnetic Materials*, 272-276, 2138-2140.

[98] H. S. Huang, M. W. Lin, Y. C. Sun and L. J. Lin. (2007) Improving the spatial resolution of a magnetic force microscope tip via focused ion beam

modification and magnetic film coating. *Scripta Materialia*, 56, 365-368.

[99] S. J. Choi, K. H. Kim, Y. J. Cho, H. s. Lee, S. h. Cho, S. J. Kwon, J. h. Moon and K. J. Lee. (2010) Demonstration of ultra-high-resolution MFM images using $Co_{90}Fe_{10}$-coated CNT probes. *Journal of Magnetism and Magnetic Materials*, 322, 332-336.

[100] F. Wolny, Y. Obukhov, T. Muhl, U. Weissker, S. Philippi, A. Leonhardt, P. Banerjee, A. Reed, G. Xiang, R. Adur, I. Lee, A. J. Hauser, F. Y. Yang, D. V. Pelekhov, B. Buchner and P. C. Hammel. (2011) Quantitative magnetic force microscopy on permalloy dots using an iron filled carbon nanotube probe. *Ultramicroscopy*, 111, 1360-1365.

[101] L. Angeloni, D. Passeri, M. Reggente, D. Mantovani and M. Rossi. (2016) Removal of electrostatic artifacts in magnetic force microscopy by controlled magnetization of the tip: application to superparamagnetic nanoparticles. *Scientific Reports*, 6, 26293.

[102] P. Rice and S. E. Russek. (1999) Observation of the effects of tip magnetization states on magnetic force microscopy images. *Journal of Applied Physics*, 85, 5163-5165.

[103] H. Saito, J. Chen and S. Ishio. (1999) Description of magnetic force microscopy by three-dimensional tip Green' function for sample magnetic charges. *Journal of Magnetism and Magnetic Materials*, 191, 153-161.

[104] D. Nyamjav, J. M. Kinsella and A. Ivanisevic. (2005) Magnetic wires with DNA cores: A magnetic force microscopy study. *Applied Physics Letters*, 86, 093107.

[105] M. Nenadović, S. Štrbac and Z. Rakočević. (2010) Quantification of the lift height for magnetic force microscopy using 3D surface parameters. *Applied Surface Science*, 256, 1652-1656.

[106] L. H. Reddy, J. L. Arias, J. Nicolas and P. Couvreur. (2012) Magnetic nanoparticles: design and characterization, toxicity and biocompatibility,

pharmaceutical and biomedical applications. *Chemical Reviews*, 112, 5818-5878.

[107] W. Wu, Q. He and C. Jiang. (2008) Magnetic iron oxide nanoparticles: synthesis and surface functionalization strategies. *Nanoscale Reseach Letters*, 3, 397-415.

[108] J. G. King, W. Williams, C. D. W. Wilkinson, S. McVitie and J. N. Chapman. (1996) Magnetic properties of magnetite arrays produced by the method of electron beam lithography. *Geophysical Research Letters*, 23, 2847-2850.

[109] A.-H. Lu, E. L. Salabas and F. Schüth. (2007) Magnetic nanoparticles: synthesis, protection, functionalization, and application. *Angewandte Chemie International Edition*, 46, 1222-1244.

[110] Y. B. Khollam, S. R. Dhage, H. S. Potdar, S. B. Deshpande, P. P. Bakare, S. D. Kulkarni and S. K. Date. (2002) Microwave hydrothermal preparation of submicron-sized spherical magnetite (Fe_3O_4) powders. *Materials Letters*, 56, 571-577.

[111] S. Laurent, D. Forge, M. Port, A. Roch, C. Robic, V. L. Elst and R. N. Muller. (2008) Magnetic iron oxide nanoparticles synthesis, stabilization, vectorization, physicochemical characterizations, and biological applications. *Chemical Reviews*, 108, 2064-2110.

[112] S. Taira, D. Kaneko, K. Onuma, A. Miyazato, T. Hiroki, Y. Kawamura-Konishi and Y. Ichiyanagi. (2012) Synthesis and characterization of functionalized magnetic nanoparticles for the detection of pesticide. *International Journal of Inorganic Chemistry*, 2012, 1-7.

[113] M. H. Korayem, M. B. Saraee, Z. Mahmoodi and S. Dehghani. (2015) Modeling and simulation of three dimensional manipulations of biological micro/nanoparticles by applying cylindrical contact mechanics models by means of AFM. *Journal of Nanoparticle Research*, 17, 439.

[114] M. B. Saraee and M. H. Korayem. (2015) Dynamic simulation and modeling

of the motion modes produced during the 3D controlled manipulation of biological micro/nanoparticles based on the AFM. *Journal of Theoretical Biology*, 378, 65-78.

[115] M. H. Korayem and M. Zakeri. (2011) Dynamic modeling of manipulation of micro/nanoparticles on rough surfaces. *Applied Surface Science*, 257, 6503-6513.

[116] M. H. Korayem and M. Zakeri. (2009) Sensitivity analysis of nanoparticles pushing critical conditions in 2-D controlled nanomanipulation based on AFM. *The International Journal of Advanced Manufacturing Technology*, 41, 714-726.

[117] M. Sitti and H. Hashimoto. (2000) Controlled pushing of nanoparticles: modeling and experiments. *IEEE/ASME Transactions on Mechatronics*, 199-211.

[118] D. Guo, J. Li, L. Chang and J. Luo. (2013) Measurement of the friction between single polystyrene nanospheres and silicon surface using atomic force microscopy. *Langmuir: the ACS Journal of Surfaces and Colloids*, 29, 6920-6925.

[119] V. Cambel, P. Elias, D. Gregusova, J. Martaus, J. Fedor, G. Karapetrov and V. Novosad. (2010) Magnetic elements for switching magnetization magnetic force microscopy tips. *Journal of Magnetism and Magnetic Materials*, 322, 2715-2721.

[120] J. Chang, H. Yi, H. Cheol Koo, V. L. Mironov, B. A. Gribkov, A. A. Fraerman, S. A. Gusev and S. N. Vdovichev. (2007) Magnetization reversal of ferromagnetic nanoparticles under inhomogeneous magnetic field. *Journal of Magnetism and Magnetic Materials*, 309, 272-277.

[121] S. Byun, S. Son, D. Amodei, N. Cermak, J. Shaw, J. H. Kang, V. C. Hecht, M. M. Winslow, T. Jacks, P. Mallick and S. R. Manalis. (2013) Characterizing deformability and surface friction of cancer cells. *Proceedings of the National Academy of Sciences of the United States of America*, 11, 7580-7585.

[122] H. Babahosseini, B. Carmichael, J. S. Strobl, S. N. Mahmoodi and M. Agah. (2015) Sub-cellular force microscopy in single normal and cancer cells. *Biochemical and Biophysical Research Communications*, 463, 587-592.

[123] I. Sokolov. (2007) Atomic force microscopy in cancer cell research. *Cancer Nanotechnolgy*, 1-17.

[124] S. Nawaz, P. Sánchez, K. Bodensiek, S. Li, M. Simons and I. A. T. Schaap. (2012) Cell visco-elasticity measured with AFM and optical trapping at sub-micrometer deformations. *Plos One*, 7, e45297.

[125] W. Xu, R. Mezencev, B. Kim, L. Wang, J. McDonald and T. Sulchek. (2012) Cell stiffness is a biomarker of the metastatic potential of ovarian cancer cells. *Plos One*, 7, e46609.

[126] S. Zhang, M. Andreasen, J. T. Nielsen, L. Liu, E. H. Nielsen, J. Song, G. Ji, n. F. Su, T. Skrydstrup, F. Besenbacher, N. C. Nielsen, D. E. Otzen and M. Dong. (2013) Coexistence of ribbon and helical fibrils originating from hIAPP20-29 revealed by quantitative nanomechanical atomic force microscopy. *Proceedings of the National Academy of Sciences of the United States of America*, 110, 2798-2803.

[127] P. Lazar, S. Zhang, K. Safářová, Q. Li, J. P. Froning, J. Granatier, P. Hobza, R. Zbořil, F. Besenbacher, M. Dong and M. Otyepka. (2013) Quantification of the interaction forces between metals and graphene by quantum chemical calculations and dynamic force measurements under ambient conditions. *ACS Nano*, 7, 1646-1651.

[128] S. Zhang, H. Aslan, F. Besenbacher and M. Dong. (2014) Quantitative biomolecular imaging by dynamic nanomechanical mapping. *Chemical Society Reviews*, 43, 7412-7429.

[129] A. Li, A. H. Mansoor, K. S. W. Tan and C. T. Lim. (2006) Observations on the internal and surface morphology of malaria infected blood cells using optical and atomic force microscopy. *Journal of Microbiological Methods*, 66, 434-439.

[130] A. Sikora and A. Iwan. (2012) AFM study of the mechanical wear phenomena of the polyazomethine with thiophene rings: tapping mode, phase imaging mode and force spectroscopy. *High Performance Polymers*, 24, 218-228.

[131] C. Heu, A. Berquand, C. Elie-Caille and L. Nicod. (2012) Glyphosate-induced stiffening of HaCaT keratinocytes, a peak force tapping study on living cells. *Journal of Structural Biology*, 178, 1-7.

[132] X. Liu, Z. Song, Y. Qu, G. Wang and Z. Wang. (2015) Mechanical properties study of SW480 cells based on AFM. *Cell Biology International*, 39, 972-977.

[133] D. Gaspar, J. M. Freire, T. R. Pacheco, J. T. Barata and M. A. Castanho. (2015) Apoptotic human neutrophil peptide-1 anti-tumor activity revealed by cellular biomechanics. *Biochimica et Biophysica Acta (BBA) - Molecular Cell Research*, 1853, 308-316.

[134] P. D. Antonio, M. Lasalvia, G. Perna and V. Capozzi. (2012) Scale-independent roughness value of cell membranes studied by means of AFM technique. *Biochimica et Biophysica Acta (BBA) - Biomembranes*, 1818, 3141-3148.

[135] M. Girasole, A. Cricenti, R. Generosi, G. Longo, G. Pompeo, Cotesta, S and A. CongiuCastellano. (2007) Different membrane modifications revealed by atomic force/lateral force microscopy after doping of human pancreatic cells with Cd, Zn, or Pb. *Microscopy Research and Technique*, 70, 912-917.

[136] Y. S. Kim, K. S. Kim, C. H. Cho, K. S. Yoon, H. K. Park and M. H. Jung. (2012) Quantitative analysis with atomic force microscopy of cisplatininduced morphological changes in HeLa and Ishikawa cells. *Journal of Nippon Medical School*, 79, 320-326.

[137] C. Pelillo, H. Mollica, J. A. Eble, J. Grosche, L. Herzog, B. Codan, G. Sava and A. Bergamo. (2016) Inhibition of adhesion, migration and of α5β1 integrin in the HCT-116 colorectal cancer cells treated with the ruthenium drug NAMI-A. *Journal of Inorganic Biochemistry*, 160, 225-235.

[138] K. Hayashi and M. Iwata. (2015) Stiffness of cancer cells measured with an AFM indentation method. *Journal of the Mechanical Behavior of Biomedical Materials*, 45, 105-111.

[139] A. Ansardamavandi, M. Tafazzoli-Shadpour, R. Omidvar and I. Jahanzad. (2016) Quantification of effects of cancer on elastic properties of breast tissue by atomic force microscopy. *Journal of the Mechanical Behavior of Biomedical Materials*, 60, 234-242.

[140] Y. M. Efremov, M. E. Lomakina, D. V. Bagrov, P. I. Makhnovskiy, A. Y. Alexandrova, M. P. Kirpichnikov and K. V. Shaitan. (2014) Mechanical properties of fibroblasts depend on level of cancer transformation. *Biochimica et Biophysica Acta (BBA) - Molecular Cell Research*, 1843, 1013-1019.

[141] D. Wirtz, K. Konstantopoulos and P. C. Searson. (2011) The physics of cancer: the role of physical interactions and mechanical forces in metastasis. *Nature Reviews Cancer*, 11, 512-522.

[142] S. D. Cio and J. E. Gautrot. (2016) Cell sensing of physical properties at the nanoscale: Mechanisms and control of cell adhesion and phenotype. *Acta Biomaterialia*, 30, 26-48.

[143] P. F. Sheehy, T. Wakonig-Vaartaja, R. Winn and B. D. Clarkson. (1974) Asynchronous DNA synthesis and asynchronous mitosis in multinuclear ovarian cancer cells. *Cancer Research*, 34, 991-996.

[144] X. W. Zhu and J. S. Friedland. (2006) Multinucleate giant cells and the control of chemokine secretion in response to Mycobacterium tuberculosis. *Clinical Immunology*, 120, 10-20.

[145] X. Lu and Y. Kang. (2009) Cell Fusion as a Hidden Force in Tumor Progression. *Cancer Research*, 69, 8536-8539.

[146] M. Beno, M. Hurbankova, M. Dusinska, S. Cerna, K. Volkovova, M. Staruchova, M. Barancokova, A. Kazimirova, Z. Kovacikova, M. Mikulecky and S. A. Kyrtopoulos. (2005) Multinucleate cells (MNC) as sensitive

semiquantitative biomarkers of the toxic effect after experimental fibrous dust and cigarette smoke inhalation by rats. *Experimental and Toxicologic Pathology*, 57, 77-87.

[147] Z. Ming, H. Dong, Q. Zhong, C. G. Grevelding and M. Jiang. (2006) The effect of a mutagen (N-methyl-N-nitro-N-nitrosoguanidine) on cultured cells from adult Schistosoma japonicum. *Parasitology Research*, 98, 430-437.

[148] P. Walter, X. Hoffmann, B. Ebeling, M. Haas and W. Marwan. (2013) Switch-like reprogramming of gene expression after fusion of multinucleate plasmodial cells of two Physarum polycephalum sporulation mutants. *Biochemical and Biophysical Research Communications*, 435, 88-93.

[149] S. Kim, R. Kim, J. Ryu, E. Jho, K. Song, S. Jang and S. Kee. (2005) Multinuclear giant cell formation is enhanced by down-regulation of Wnt signaling in gastric cancer cell line. *Experimental Cell Research*, 308, 18-28.

[150] A. Guffei, R. Sarkar, L. Klewes, C. Righolt, H. Knecht and S. Mai. (2010) Dynamic chromosomal rearrangements in Hodgkin's lymphoma are due to ongoing three-dimensional nuclear remodeling and breakage-bridge-fusion cycles. *Haematological the Hematology Journal*, 95, 030171.

[151] Y. Kuroda and J. Furuyama. (1963) Physiological and biochemical studies of effects of mitomycin C on strain HeLa cells in cell culture. *Cancer Research*, 23, 682-687.

[152] D. E. Cool, P. R. Andreassen, N. K. Tonks, E. G. Krebs, E. H. Fischer and R. L. Margolis. (1992) Cytokinetic failure and asynchronous nuclear division in BHK cells overexpressing a truncated protein-tyrosine-phosphatase. *Proceedings of the National Academy of Sciences of the United States of America*, 89, 5422-5426.

[153] J. M. Papadimitriou, D. Sforsina and L. Papaelias. (1973) Kinetics of multinucleate giant cell formation and their modification by various agents in foreign body reactions. *American Journal of Pathology*, 73, 349-364.

[154] H. Knecht, B. Sawan, D. Lichtensztejn, B. Lemieux, R. J. Wellinger and S. Mai. (2009) The 3D nuclear organization of telomeres marks the transition from Hodgkin to Reed-Sternberg cells. *Leukemia*, 23, 565-573.

[155] H. Knecht, B. Sawan, Z. Lichtensztejn, D. Lichtensztejn and S. Mai. (2010) 3D Telomere FISH defines LMP1-expressing Reed-Sternberg cells as end-stage cells with telomere-poor 'ghost' nuclei and very short telomeres. *Laboratory Investigation*, 90, 611-619.

[156] W. Zhang, Q. Lin, A. J. Ramoth, D. Fan and I. J. Fidler. (2011) Formation of solid tumors by a single multinucleated cancer cell. *Cancer*, 117, 4092-4099.

[157] S. Trabulo, A. Aires, A. Aicher, C. Heeschen and A. L. Cortajarena. (2017) Multifunctionalized iron oxide nanoparticles for selective targeting of pancreatic cancer cells. *Biochimica et Biophysica Acta (BBA) - General Subjects*, 1861, 1597-1605.

[158] J. Varshosaz, F. Hassanzadeh, H. S. Aliabadi, F. R. Khoraskani, M. Mirian and B. Behdadfar. (2016) Targeted delivery of doxorubicin to breast cancer cells by magnetic LHRH chitosan bioconjugated nanoparticles. *International Journal of Biological Macromolecules*, 93, 1192-1205.

[159] X. Du, J. Zhou and B. Xu. (2015) Ectoenzyme switches the surface of magnetic nanoparticles for selective binding of cancer cells. *Journal of Colloid and Interface Science*, 447, 273-277.

[160] E. Borroni, M. Miola, S. Ferraris, G. Ricci, K. Zuzek Rozman, N. Kostevsek, A. Catizone, L. Rimondini, M. Prat, E. Verne and A. Follenzi. (2017) Tumor targeting by lentiviral vectors combined with magnetic nanoparticles in mice. *Acta biomaterialia*, 59, 303-316.

[161] D. Tsoucas and G. C. Yuan. (2017) Recent progress in single-cell cancer genomics. *Current Opinion Genetics & Development*, 42, 22-32.

[162] P. Abraham and T. T. Maliekal. (2017) Single cell biology beyond the era of antibodies: relevance, challenges, and promises in biomedical research.

Cellular and Molecular Life Sciences, 74, 1177-1189.

[163] N. Welkenhuysen, J. Borgqvist, M. Backman, L. Bendrioua, M. Goksor, C. B. Adiels, M. Cvijovic and S. Hohmann. (2017) Single-cell study links metabolism with nutrient signaling and reveals sources of variability. *BMC Systems Biology*, 11, 59.

[164] H. Matsuoka, T. Komazaki, Y. Mukai, M. Shibusawa, H. Akane, A. Chaki, N. Uetake and M. Saito. (2005) High throughput easy microinjection with a single-cell manipulation supporting robot. *Journal of Biotechnology*, 116, 185-194.

[165] O. Guillaume-Gentil, E. Potthoff, D. Ossola, P. Dorig, T. Zambelli and J. A. Vorholt. (2013) Force-controlled fluidic injection into single cell nuclei. *Small*, 9, 1904-1907.

[166] D. Guarisco and H. Nguy. (2003) High linear density in perpendicular recording. *Journal of Applied Physics*, 93, 6745.

[167] D. N. Geerpuram, A. S. Mani and V. S. Baskaran. (2004) A novel magnetic random access memory design using square ring elements for the hard layer. *Journal of Electronic Materials*, 33, 1269-1273.

[168] J. D. Wei, I. Knittel, C. Lang, D. Schüler and U. Hartmann. (2011) Magnetic properties of single biogenic magnetite nanoparticles. *Journal of Nanoparticle Research*, 13, 3345-3352.

[169] Y. Lisunova, J. Heidler, I. Levkivskyi, I. Gaponenko, A. Weber, C. Caillier, L. J. Heyderman, M. Klaui and P. Paruch. (2013) Optimal ferromagnetically-coated carbon nanotube tips for ultra-high resolution magnetic force microscopy. *Nanotechnology*, 24, 105705.

[170] B. Kumar, P. M. Pifer, A. Giovengo and J. Legleiter. (2010) The effect of set point ratio and surface Young's modulus on maximum tapping forces in fluid tapping mode atomic force microscopy. *Journal of Applied Physics*, 107, 044508.

[171] G. Y. Chen. (1996) Transient response of tapping scanning force microscopy in liquids. *Journal of Vacuum Science & Technology B*, 14, 1313.

[172] B. J. Rodriguez, S. Jesse, A. P. Baddorf and S. V. Kalinin. (2006) High resolution electromechanical imaging of ferroelectric materials in a liquid environment by piezoresponse force microscopy. *Physical Review Letters*, 96, 237602.

[173] J. E. Sader. (1998) Frequency response of cantilever beams immersed in viscous fluids with applications to the atomic force microscope. *Journal of Applied Physics*, 84, 64-76.

[174] K. Kobayashi, H. Yamada and K. Matsushige. (2009) Frequency noise in frequency modulation atomic force microscopy. *Revew of Scientific Instruments*, 80, 043708.

[175] K. J. Tapan, K. R. Maram, A. M. Marco, L. L. Diandra and L. Vinod. (2008) Biodistribution, clearance, and biocompatibility of iron oxide magnetic nanoparticles in rats. *Molecular Pharmaceutics*, 5, 316-327.

[176] E. E. L. Lewis, H. W. Child, A. Hursthouse, D. Stirling, M. McCully, D. Paterson, M. Mullin and C. C. Berry. (2015) The influence of particle size and static magnetic fields on the uptake of magnetic nanoparticles into three dimensional cell-seeded collagen gel cultures. *Journal of Biomedical Materials Research Part B Applied Biomaterials*, 103, 1294-1301.

[177] A. Sarella, A. Torti, M. Donolato, M. Pancaldi and P. Vavassori. (2014) Two-dimensional programmable manipulation of magnetic nanoparticles on-chip. *Advanced Materials*, 26, 2384-2390.

[178] P. Xu, G. M. Zeng, D. L. Huang, C. L. Feng, S. Hu, M. H. Zhao, C. Lai, Z. Wei, C. Huang, G. X. Xie and L. Z. F. (2012) Use of iron oxide nanomaterials in wastewater treatment: A review. *Science of The Total Environment*, 424, 1-10.

[179] M. G. Troia, G. E. P. Henriques, M. F. Mesquita and W. S. Fragoso. (2008)

The effect of surface modifications on titanium to enable titanium–porcelain bonding. *Dental Materials*, 24, 28-33.

[180] H. Y. Nie, M. J. Walzak and N. S. McIntyre. (2002) Use of biaxially oriented polypropylene film for evaluating and cleaning contaminated atomic force microscopy probe tips: An application to blind tip reconstruction. *Revew of Scientific Instruments*, 73, 3831-3836.

[181] S. Schreiber, M. Savla, D. V. Pelekhov, D. F. Iscru, C. Selcu, P. C. Hammel and G. Agarwal. (2008) Magnetic force microscopy of superparamagnetic nanoparticles. *Small*, 4, 270-278.

[182] T. M. Nocera, J. Chen, C. B. Murray and G. Agarwal. (2012) Magnetic anisotropy considerations in magnetic force microscopy studies of single superparamagnetic nanoparticles. *Nanotechnology*, 23, 495704.

[183] S. Prijic, J. Scancar, R. Romih, M. Cemazar, V. B. Bregar, A. Znidarsic and G. Sersa. (2010) Increased cellular uptake of biocompatible superparamagnetic iron oxide nanoparticles into malignant cells by an external magnetic field. *The Journal of Membrane Biology*, 236, 167-179.

[184] M. Palacio and B. Bhushan. (2008) A nanoscale friction investigation during the manipulation of nanoparticles in controlled environments. *Nanotechnology*, 19, 315710.

[185] D. Maharaj, B. Bhushan and S. Iijima. (2013) Effect of carbon nanohorns on nanofriction and wear reduction in dry and liquid environments. *Journal of Colloid and Interface Science*, 400, 147-160.

[186] N. V. Zarate, A. J. Harrison, J. D. Litster and S. P. Beaudoin. (2013) Effect of relative humidity on onset of capillary forces for rough surfaces. *Journal of Colloid and Interface Science*, 411, 265-272.

[187] H. J. Butt, B. Cappella and M. Kappl. (2005) Force measurements with the atomic force microscope: Technique, interpretation and applications. *Surface Science Reports*, 59, 1-152.

[188] E. Hsiao, M. J. Marino and S. H. Kim. (2010) Effects of gas adsorption isotherm and liquid contact angle on capillary force for sphere-on-flat and cone-on-flat geometries. *Journal of Colloid and Interface Science*, 352, 549-557.

[189] G. Lian and J. Seville. (2016) The capillary bridge between two spheres: New closed-form equations in a two century old problem. *Advances in Colloid and Interface Science*, 227, 53-62.

[190] G. V. Dedkov. (1999) Friction on the nanoscale: new physical mechanisms. *Materials Letters*, 38, 360-366.

[191] S. Kayal, D. Bandyopadhyay, T. K. Mandal and R. V. Ramanujan. (2011) The flow of magnetic nanoparticles in magnetic drug targeting. *RSC Advances*, 1, 238-246.

[192] Y. S. Kang, S. Risbud, J. F. Rabolt and P. Stroeve. (1996) Synthesis and characterization of nanometer-size Fe_3O_4 and γ-Fe_2O_3 particles. *Chemistry of Materials*, 8, 2209-2211.

[193] J. Xu, K. J. Kwak, J. L. Lee and G. Agarwal. (2010) Lifting and sorting of charged Au nanoparticles by electrostatic forces in atomic force microscopy. *Small*, 6, 2105-2108.

[194] E. Mirowski, J. Moreland, A. Zhang, S. E. Russek and M. J. Donahue. (2005) Manipulation and sorting of magnetic particles by a magnetic force microscope on a microfluidic magnetic trap platform. *Applied Physics Letters*, 86, 243901.

[195] B. Lee and R. E. Rudd. (2007) First-principles study of the Young's modulus of Si ⟨001⟩ nanowires. *Physical Review B*, 75, 041305(R).

[196] N. Lepot, M. K. Van Bael, H. Van den Rul, J. D'Haen, R. Peeters, D. Franco and J. Mullens. (2011) Influence of incorporation of ZnO nanoparticles and biaxial orientation on mechanical and oxygen barrier properties of polypropylene films for food packaging applications. *Journal of Applied*

Polymer Science, 120, 1616-1623.

[197] H. Jin, X. Zhong, Z. Wang, X. Huang, H. Ye, S. Ma, Y. Chen and J. Cai. (2011) Sonodynamic effects of hematoporphyrin monomethyl ether on CNE-2 cells detected by atomic force microscopy. *Journal of Cellular Biochemistry*, 112, 169-178.

[198] X. Cai, S. Gao, J. Cai, Y. Wu and H. Deng. (2009) Artesunate induced morphological and mechanical changes of Jurkat cell studied by AFM. *Scanning*, 31, 83-89.

[199] J. R. Baena, M. Gallego and M. Valcárcel. (2002) Fullerenes in the analytical sciences. *Trends in Analytical Chemistry*, 21, 187-198.

[200] I. Rade, R. Natasa, G. Biljana, D. Aleksandar and S. Borut. (2008) Bioapplication and activity of fullerenol $C_{60}(OH)_{24}$. *African Journal of Biotechnology*, 7, 4940-4950.

[201] J. Gao, Y. Wang, K. M. Folta, V. Krishna, W. Bai, P. Indeglia, A. Georgieva, H. Nakamura, B. Koopman and B. Moudgil. (2011) Polyhydroxy fullerenes (fullerols or fullerenols): beneficial effects on growth and lifespan in diverse biological models. *Plos One*, 6, e19976.

[202] R. Injac, M. Perse, N. Obermajer, V. Djordjevic-Milic, M. Prijatelj, A. Djordjevic, A. Cerar and B. Strukelj. (2008) Potential hepatoprotective effects of fullerenol $C_{60}(OH)_{24}$ in doxorubicin-induced hepatotoxicity in rats with mammary carcinomas. *Biomaterials*, 29, 3451-3460.

[203] P. Chaudhuri, A. Paraskar, S. Soni, R. A. Mashelkar and S. Sengupta. (2009) Fullerenol-cytotoxic conjugates for cancer chemotherapy. *ACS Nano*, 3, 2505-2514.

[204] V. M. Torres, B. Srdjenovic, V. Jacevic, V. D. Simic, A. Djordjevic and A. L. Simplício. (2010) Fullerenol $C_{60}(OH)_{24}$ prevents doxorubicin-induced acute cardiotoxicity in rats. *Pharmacological Reports*, 62, 707-718.

[205] J. Grebowski, A. Krokosz and M. Puchala. (2013) Fullerenol $C_{60}(OH)_{36}$ could

associate to band 3 protein of human erythrocyte membranes. *Biochimica et Biophysica Acta (BBA) - Biomembranes*, 1828, 2007-2014.

[206] T. Çavas, N. Çinkılıç, Ö. Vatan and D. Yılmaz. (2014) Effects of fullerenol nanoparticles on acetamiprid induced cytoxicity and genotoxicity in cultured human lung fibroblasts. *Pesticide Biochemistry and Physiology*, 114, 1-7.

[207] M. Zhao, C. Srinivasan, D. J. Burgess and B. D. Huey. (2011) Rate- and depth-dependent nanomechanical behavior of individual living Chinese hamster ovary cells probed by atomic force microscopy. *Journal of Materials Research*, 21, 1906-1912.

[208] F. Rico, P. Roca-Cusachs, N. Gavara, R. Farré, M. Rotger and D. Navajas. (2005) Probing mechanical properties of living cells by atomic force microscopy with blunted pyramidal cantilever tips. *Physical Review E*, 72, 021914.

[209] G. Cao, J. Sui and S. Sun. (2013) Evaluating the nucleus effect on the dynamic indentation behavior of cells. *Biomechanics and Modeling in Mechanobiology*, 12, 55-66.

[210] R. Qiao, A. P. Roberts, A. S. Mount, S. J. Klaine and P. C. Ke. (2007) Translocation of C_{60} and its derivatives across a lipid bilayer. *Nano Letters*, 7, 614-619.

[211] S. Rungaldier, W. Oberwagner, U. Salzer, E. Csaszar and R. Prohaska. (2013) Stomatin interacts with GLUT1/SLC2A1, band 3/SLC4A1, and aquaporin-1 in human erythrocyte membrane domains. *Biochimica et Biophysica Acta (BBA) - Biomembranes*, 1828, 956-966.

[212] E. Augustin, B. Czubek, A. M. Nowicka, A. Kowalczyk, Z. Stojek and Z. Mazerska. (2016) Improved cytotoxicity and preserved level of cell death induced in colon cancer cells by doxorubicin after its conjugation with iron-oxide magnetic nanoparticles. *Toxicology in Vitro*, 33, 45-53.

[213] B. Cross, F. Ronzon, B. Roux and J. R. Rieu. (2005) Measurement of the

Anchorage Force between GPI-Anchored Alkaline Phosphatase and Supported Membranes by AFM Force Spectroscopy. *Langmuir: the ACS Journal of Surfaces and Colloids*, 21, 5149-5153.

[214] S. W. Han, C. Nakamura, I. Obataya, N. Nakamura and J. Miyake. (2005) A molecular delivery system by using AFM and nanoneedle. *Biosensors and Bioelectronics*, 20, 2120-2125.

[215] I. Obataya, C. Nakamura, S. Han, N. Nakamura and J. Miyake. (2005) Mechanical sensing of the penetration of various nanoneedles into a living cell using atomic force microscopy. *Biosensors and Bioelectronics*, 20, 1652-1655.